CONTINUOUS RESTORATION OF THE HUMAN VESTIBULO-OCULAR REFLEX USING A MULTICHANNEL VESTIBULAR IMPLANT

by

Peter J. Boutros

A dissertation submitted to Johns Hopkins University in conformity with the requirements for the degree of Doctor of Philosophy.

Baltimore, Maryland

December, 2018

Abstract

Bilateral loss of vestibular sensation causes blurry vision during head movement, postural instability, chronic unsteadiness, and an increased fall risk. Individuals who fail to compensate despite rehabilitation therapy and cessation of exacerbating medications have no adequate treatment options. Inspired by the success of cochlear implants in restoring hearing, prosthetic stimulation of vestibular afferent neurons to encode head motion has been investigated as a potential treatment. Until now, no human had been continuously stimulated for more than a day, and human responses had not been assessed using 3-dimensional (3D) binocular oculography, without which one cannot determine whether an implant independently stimulates each of the implanted ear's three semicircular canals.

We report 3D binocular vestibulo-ocular reflex (VOR) responses in four human subjects with bilateral vestibular loss who were each implanted with a system designed to provide long-term motion-modulated prosthetic stimulation via electrodes in the semicircular canals of one ear. Initiation of prosthetic stimulation evoked nystagmus that decayed within 30 minutes. Stimulation targeting one canal produced 3D VOR responses aligned with that canal’s anatomic axis, while targeting canal pairs reliably yielded responses aligned with a vector sum of individual responses. Over 8 weeks of continuous use, modulated electrical stimulation produced robust and stable VOR responses that grew predictably with stimulus intensity and aligned approximately with any specified 3D head rotation axis. Combining mechanical and electrical stimulation enhanced low frequency responses. These results demonstrate that a vestibular implant can partially restore 3D inner ear sensation to individuals disabled by vestibular loss. Lastly, we show that temporal discretization inherent to cochlear implant signal processing has minimal effects on evoked responses, motivating a future combined device.

Primary reader: Charles C. Della Santina, Ph.D., M.D.

Secondary reader: Gene Y. Fridman, Ph.D.

This dissertation is dedicated to Merlin, the love of my life. Completing this would have been impossible without you. Thank you for your love, support, and patience.

Acknowledgements

It is difficult to describe the impact Dr. Charley Della Santina has had on my life, both academically and personally. In the lab, your guidance and leadership has gone beyond what I was expecting when starting graduate school. You always found a fine line between structured scientific discovery and providing room to learn things on my own. It was not uncommon for meetings in your office to become sprawling discussions ending after the sun went down. Beyond the lab, you have always given me excellent guidance for my career, found unique opportunities for my professional development, offered the perfect personal story that put my problems in perspective, or came up with the ideal movie/music reference to make me laugh. Your brilliance and unrivaled work ethic is what I aspire to achieve in my professional career. It's been an honor to work in your lab.

Next, I would remiss if I didn't take the time to thank the other members of my thesis committee. Dr. Gene Fridman, you were one of the first people I met at Hopkins and have been a friendly face working right next door for my entire time here. From my days struggling through chinchilla surgeries next to you in Ross 833, to asking your advice on job prospects, you have been around my life for this entire journey and I am so honored you are a part of my committee. To Dr. Kathy Cullen, I feel so privileged to have been a trainee at Hopkins when you moved here from McGill University. I remember diligently reading your lab's manuscripts in my earliest lab days, and now I have the tremendous honor of having you on my thesis committee.

Next, I would like to acknowledge everyone associated with the Vestibular NeuroEngineering Lab (VNEL). I believe our lab attracts unique individuals who strive for excellence, work incredibly hard, yet do it all with a smile and an open heart. First, I want to thank Kristin Hageman. In the early days when it was just the two of us in the Ross 830 cubicles, you were a big help getting me on the right track. You are an incredible engineer and I am so glad I had the opportunity to work alongside you. Meg Chow, it has been so much fun working with you these past few years. I am so impressed with your intellect, humor, and work ethic. I'm expecting big things from you! Kelly Lane, you have been a guiding force for the lab and constantly generous with your time. From crab feasts in your backyard, to your yearly wine festivals, you have injected real fun into our lab. Dale Roberts, you were truly my second mentor in the lab. Your expertise in electronics and computer science has been a critical part of my training. You were always ready to help me optimize code, work through a tough computation, tune a motor, or debug a circuit. It has been a real treasure learning from you these past 6 years. Next, I want to thank Desi Schoo. Your contribution to the trial is immeasurable and your friendship made the long nights in JHOC feasible. Dr. Chenkai Dai, I am very gratefully to have worked and learned from you. Andrianna Ayiotis, I am constantly impressed by your drive and professionalism. I cannot think of a more qualified person to lead this work going forward. Brian Morris, it has been a pleasure working with you this past year. Your talent and creativity will serve you very well in the lab. To Abderrahmane Hedjoudje, it was always a delight when you left your serene life in Europe to visit us in the lab. I look forward seeing more of your future side career hosting talk shows and creating documentaries. I also want to mention: JoongHo Ahn, Lani Swarthout, Pengyu Ren, Bryan Ward, Dan Sun, Carolina Treviño, Guoliang Wang, and Shiyao Dong.

From my experience working on the MVI™ trial, first and foremost I want to thank our study subjects. Their courage and patience is truly astounding, and I am eternally grateful for the numerous hours they have devoted to these experiments. Mehdi Rahman, it has been incredible to work with you both in the lab and throughout the trial. We've spent hours working through rotational kinematics or validating stimulation experiments. Your hard work creating the MVI™ fitting software, integrating the VOG acquisition system, collecting data with me, and being a great friend has made this work possible. Nic Valentin, your incredible contribution to the trial creating the 3DBinoc™ goggles, designing the test equipment, and being an incredible asset to the team has made this work possible. Also, I have enjoyed being the only person to get your a cappella Motown/hip-hop references throughout the long subject visits. I would also like to thank the rest of the extended MVI™ team: Dr. John Carey, Yoav Gimmon, Dr. Michael Schubert, and Stephen Bowditch. Also, many thanks to the MED-EL group involved with the MVI™ project: Andreas Hofner, Aitor Morillo Rascon, Andreas Marx, Fabio Rodriquez, Ross Deas, Stefan Strasser, Carolyn Garnham, and Andreas Jaeger.

Next, I want to thank some of my friends who have made this long journey possible. I want to thank my friends from the Wang lab: Kai Yuen Lim, Mike Osmanski, and Darik Gamble. Even though I only did a short rotation in your lab, you guys brought me into your group for many happy hours and late-night discussions. I want to thank my friends in Hopkins BME: Joe Galaro, Alyssa Kosmides, Mike Batista, Zinnia Xu, Griffin Milsap, and many others. I want to thank Dilawer Singh for being a great friend for many years, in addition to the rest of the Fridman lab.

Lastly, I want to thank my family. Merlin, I am certain I would not have made it to the end without your constant support and love. Thank you for always being there for me. To Baba and Mama, you have supported me throughout my whole life and I cannot express how much I love you. To Mom, I still remember all the car rides to high school so many years ago. I know I wouldn't be here without your support and I love you. Katie, Greg, and Gabe: I love you all so much. Tommy, ya gazma, thanks for always being available to hear me complain. To my cousin Mina, you were my partner in crime for so many years and always my biggest champion.

The work in this dissertation was supported by the National Institute on Deafness and Other Communication Disorders of the National Institutes of Health under R01DC013536 and R01DC009255. I am very grateful for my financial support including: the above NIH grants, a pre-doctoral training grant (2T32DC000023-31) through the Johns Hopkins Center for Hearing and Balance, and lastly pre-doctoral funding supplied by the Johns Hopkins Department of Biomedical Engineering.

Contents

List of Figures

List of Tables

Chapter 1 Introduction

1.1 Significance

The vestibular system provides sensory inputs that contribute to our sense of balance and play essential but normally unnoticed roles in stabilizing vision, posture, gait, cerebral perfusion and spatial orientation. For individuals suffering from profound loss of vestibular function, the missing sensory inputs of head movement and tilt drastically degrades their quality of life. Recent studies estimate ~1.8M adults suffer from bilateral vestibular hypofunction worldwide [1]. Many of these individuals report a significant increase in frequency of falls, loss in productivity due to dizziness, an overall reduced ability to participate in society, and an average economic burden of ~$13K annually [2].

In marked contrast to severe sensorineural hearing loss, for which cochlear implants (CIs) now provide auditory sensation to over 300K individuals worldwide, clinicians currently have no restorative treatment to offer individuals disabled by loss of inner ear vestibular sensation who fail to improve sufficiently despite rehabilitative therapy and cessation of vestibular suppressant medications. For these individuals, selective prosthetic electrical stimulation of surviving afferent fibers within each branch of the vestibular nerve may partially restore balance sensation. This dissertation describes both acute and longitudinal results from the first-in-human clinical trial of a multichannel vestibular implant aimed to continuously restore vestibular function. Additionally, we examine the effect of temporal discretization of stimulus pulse timing on prosthetic vestibular responses in anticipation of a future combined cochlear/vestibular inner ear implant.

1.2 Organization

This dissertation will outline our efforts to advance the development of a multichannel vestibular implant that electrically stimulates the vestibular nerve to continuously restore balance sensation for individuals suffering from severe loss of balance sensation. The remainder of this chapter will outline a brief background of the vestibular system, loss of vestibular sensation, treatment options, previous work investigating VI technology in animal models, preliminary studies studying acute stimulation of the vestibular labyrinth in human subjects, and lastly a methods overview for the whole dissertation. Chapter 2 outlines acute responses to prosthetic stimulation of the vestibular system assayed in 4 human subjects using 3D oculographic techniques. Additionally, this chapter will review adaptation to activation of the device. Chapter 3 summarizes the longitudinal changes to implant effectiveness as vestibular compensation mechanisms adapt central processing of prosthetic input. In Chapter 4 we will examine the effect of temporal discretization on vestibular prosthetic electrical stimulation to guide future development of inner ear prosthetics. Lastly, in Chapter 5 we will review the next steps of vestibular implant research and future directions of all reported work.

1.3 Background

1.3.1 Vestibular Anatomy and Physiology

Each human vestibular labyrinth comprises a collection of five sensory organs in each inner ear that contribute to the sensation of balance and spatial orientation. The three semicircular canals encode rotational components of head motion via a mechanotransduction mechanism in which fluid within each canal acts as an inertial load during rotations, causing displacement of a gelatinous membrane (cupula) that overlies the sensory epithelium (crista ampullaris) of the canal. Deflection of the cupula applies a shear stress on the stereocilia of hair cells within the crista, opening mechanically gated ion channels. The resulting ionic transfer modulates neurotransmitter release to primary vestibular afferents innervating the hair cells, evoking spike rate fluctuations above and below the spontaneous discharge rate to encode the dynamics of head motion [3,4].

Each canal is most sensitive to one component of 3-dimensional (3D) head rotational velocity and approximately coplanar with an oppositely-oriented partner in the right ear, and the difference in afferent neuron activity reaching the brainstem from those two complementary canals provide an approximately linear signal encoding head rotational velocity in their plane. The six canals of the two ears comprise three mutually orthogonal co-planar pairs that decompose a head rotation about any 3D axis into its angular velocity components in the left-anterior/right-posterior (LARP), right-anterior/left-posterior (RALP), and left-horizontal/right-horizontal (LHRH) canal planes. Together, the three pairs of canals therefore form an approximately orthogonal basis set for transformation of 3D head rotational motion into neural signals encoding three independent and complementary streams of directional information. Those neural signals in turn drive vision- and posture-stabilizing reflexes. One of these, the 3D angular vestibulo-ocular reflex (VOR), stabilizes vision during head rotation by generating eye movements that continuously and effectively steady the visual field on each retina [3,5].

The VOR is a dynamic system generating eye movements that are roughly 180° out of phase with head rotational velocity with a gain near 1 (i.e., eye movements that are equal in amplitude but opposite in direction of head velocity) from ~0.1-15Hz [3,4]. The short, three neuron VOR circuit provides corrective eye movements with a latency of ~7ms in normal humans [6], allowing vision to remain stable while walking or jogging. The VOR works without any visual input (i.e., it is an adaptive but open loop control system), and is thus only enhanced when the relatively slow (latency of ~60ms [7]) dominates the control of gaze.

1.3.2 Unilateral Vestibular Hypofunction (UVH)

Some people experience symptoms of unilateral vestibular hypofunction (UVH) due to either unintended noxious insults to one vestibular labyrinth or induced unilateral hypofunction (via labyrinthectomy or intratympanic aminoglycoside injections) as a treatment for vertigo caused by disorders such as Ménière’s disease. These individuals often experience a sudden-onset asymmetric VOR function in the acute post-insult period. In the chronic period following onset of UVH most subjects undergo a recovery of VOR function at modest frequencies (<0.5Hz) and head velocities (<100°/s), allowing these individuals to function normally with limited loss of gaze stabilization and balance sensation [8,9]. This recovery involves synaptic reorganization of central vestibulo-cerebellar circuits and upregulation of other sensory inputs to supplement the damaged ear. This recalibration of vestibular sensation after a unilateral lesion is termed *vestibular compensation* [10,11] and can last days to months from the onset of UVH symptoms. Integration of vestibular rehabilitation exercises in the post-injury period can help accelerate and extend recovery of function.

1.3.3 Bilateral Vestibular Hypofunction (BVH)

Individuals disabled by bilateral vestibular hypofunction (BVH) suffer from blurred vision during head movements (oscillopsia), postural instability, chronic disequilibrium and fatigue that stems from having to exert cognitive effort to perform normally automatic tasks such as walking down a grocery store aisle while looking at items on the shelves. The impact of BVH on quality of life (QOL), productivity and health care consumption is substantial: Sun *et al*. (2014) estimated that a US adult with BVH incurs a significant reduction in QOL and a mean annual economic burden of $13K (range $0-$49K) per capita compared to demographically matched controls without vestibular loss [2]. Analyzing data from the 2008 United States National Health Interview Survey, Ward *et al*. (2013) estimated the point prevalence of severe, disabling BVH among adults at 28 per 100K, or about 64K US adults and 1.8M adults worldwide [1].

For many etiologies of profound BVH, including aminoglycoside antibiotic ototoxicity, the insult is localized to the vestibular labyrinth/hair cells that normally modulate neurotransmitter release to primary vestibular afferents. In many cases, the first order neurons are intact yet unable to encode head velocity due to damage of the peripheral mechanotransduction pathway. With the peripheral nerve branch within each canal intact, generating patterned activity to encode head motion may provide a therapeutic method of alleviating BVH symptoms. Moreover, if prosthetic input in one ear could independently modulate activity within each canal ampullary nerve branch above and below a level mimicking spontaneous discharge levels, one could restore bidirectional vestibular sensation allowing a BVH patient to potentially benefit from vestibular compensation experienced by UVH individuals.

1.3.4 Treatment for BVH

Like those with UVH, individuals suffering from BVH can learn to compensate partially for their loss of balance sensation via vestibular rehabilitation exercises and upregulating other sensory systems [12]. While effective in many individuals with less severe BVH, those suffering from profound, disabling BVH often find that other sensory systems cannot sufficiently stabilize gaze and provide temporally appropriate sensation. These strategies include integrating predictive anticipatory eye movements, visual input [7], cervico-ocular reflex enhancements [10,13], and auditory cues [14,15]. Additionally, some teams investigating sensory substitution prosthetics involving electrical stimulation of the torso [16,17] and tongue [18] have had modest success replicating a minimal subset of motion cues. While those options may provide some relief for individuals suffering from severe BVH, there are currently no restorative options available for clinicians treating these patients. Affected individuals who fail to compensate sufficiently through rehabilitative exercises and cessation of vestibular suppressant medications currently have no adequate treatment options.

1.3.5 Electrical Stimulation of Primary Vestibular Afferents

Although failure of reflexes normally driven by inner ear sensation can be caused by downstream lesions in the central nervous system, BVH is often caused by ototoxic injury (e.g., by gentamicin and other aminoglycoside antibiotics), ischemia, infection, Ménière's disease, or genetic inner ear abnormalities. When the vestibular nerve branches to the 3 canals in an affected labyrinth are at least partially intact, prosthetic electrical stimulation encoding head motion may provide an effective means of partially restoring vestibular sensation and alleviating symptoms suffered by individuals chronically disabled by BVH. This approach is directly analogous to that of cochlear implants, which use patterned electrical stimulation to partially restore hearing via bypassing absent or abnormal cochlear hair cells.

Electrical stimulation of vestibular afferent neurons to partially restore the VOR has been effective in driving reflexive eye movements in cat [19–23], guinea pig [24–29], chinchilla [30–34], rabbit [21,29], dog [23], and non-human primate [20,23,35–40] animal models. Those preclinical studies provided promising evidence that a vestibular implant could produce robust eye movements and that selective electrical stimulation of individual canal afferent nerve branches can produce ocular responses in the plane of the targeted canal. Importantly, they also showed that simultaneous but independent activation of multiple vestibular nerve branches can elicit VOR eye movements rotating about an axis approximating the vector summation of the sensitivity axes for each canal scaled by the relative magnitudes of the stimuli delivered to each canal. Studies using prototype multichannel vestibular prosthetic devices that sensed 3D head motion and modulated electrical stimulation of each vestibular nerve branch partially restored conjugate binocular VOR responses [36,39,40] (outlined using data from [36] in Figure 1.1), drove brainstem and cerebellar directional plasticity circuits to minimize 3D VOR misalignment [33,37], and implemented a 3D coordinate transformation to optimize stimuli and further reduce misalignment [31,38].

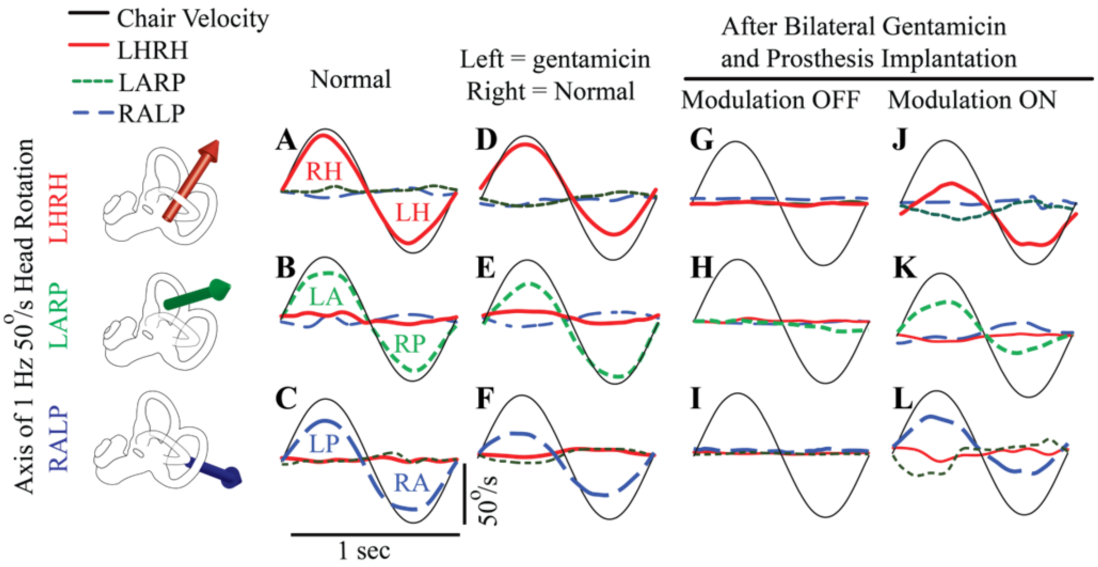

Figure 1.1. Second generation Johns Hopkins Multichannel Vestibular Prosthesis (MVP2) results in non-human primates. Mean eye and head angular velocities during 1Hz, 50°/s sinusoidal head rotations in darkness delivered about the left-horizontal/right-horizontal (LHRH, top row), left-anterior/right-posterior (LARP, middle row), and right-anterior/left-posterior (RALP, bottom row) semicircular canal anatomic axes. Experiments were repeated with (**A-C**) animals with normal vestibular function, (**D-F**) after unilateral gentamicin treatment, (**G-I**) following bilateral injection of gentamicin with prosthesis motion-modulation turned off, (**J-L**) and lastly bilaterally deficient animals with MVP stimulation providing motion-modulated prosthetic input. Standard deviations throughout each mean waveform was <10°/s. Adapted from [36].

1.3.6 Electrical Stimulation of the Human Vestibular System

Over the past decade, work investigating prosthetic electrical stimulation of the human vestibular labyrinth has demonstrated that stimulation targeting vestibular nerve branches can evoke eye movements that are approximately consistent with target canal orientations. In 2007, Wall, Kos, and Guyot described intraoperative electrical stimulation of the posterior canal nerve branch in three subjects undergoing ear surgery under local anesthesia and observed approximately vertical VOR responses [41]. By 2018, 13 patients with BVH and severe hearing loss at the Geneva University Hospitals and Maastricht University Medical Center had undergone implantation of a cochlear implant modified to allow redirection and implantation of 1-3 electrodes in canals or near their vestibular nerve branches. Responses were variable, but all implanted subjects elicited measurable VOR responses approximately aligned with the target canal with at least one implanted electrode when assayed using 2D oculography [42–50].

Rubinstein, Phillips et al. described a study involving unilateral implantation of a vestibular stimulator intended for use as a temporary pacing device during vertigo attacks caused by unilateral Menière's disease [51,52]. All four subjects implanted in that study suffered a profound post-operative loss of hearing and vestibular sensation in the implanted ear; however, transient electrical stimulation elicited modest VOR eye movements roughly aligned with the intended plane in 5 of 11 implanted canals. When tested longitudinally (i.e., in repeated transient stimulation sessions distributed over many months without stimulation between test sessions), responses fluctuated or decreased from session to session in most cases. While those studies demonstrated that acute/transient prosthetic vestibular stimulation can produce modest electrically-evoked eye movements, both groups used 2D oculographic techniques that restrict estimation of relative activation of individual canal ampullary nerves.

1.4 Methods Overview

Experiments in Chapter 2 and Chapter 3 were completed with 4 human subjects suffering from severe BVH conducted under a protocol approved by the Johns Hopkins

University Institutional Review Board (IRB Study Number NA_00051349) and registered on the ClinicalTrials.gov database (#NCT02725463) [53]. The Labyrinth Devices Multichannel Vestibular Implant™ (MVI™) used in these chapters was developed and manufactured through a collaboration between Labyrinth Devices, LLC and MED-EL GmbH. The devices were provided by Labyrinth Devices, LLC to the Johns Hopkins study team for use only in this study under FDA Investigational Device Exemption G150198 [53]. Details of study design, enrolled subjects, surgical procedure, 3D eye movement recording, and data analysis are outlined in later chapters (sections 2.2 and 3.2). In brief, each subject was implanted with an MVI™ stimulator, which comprises a MED-EL GmbH cochlear implant stimulator modified with an array of intralabyrinthine electrodes inserted into each semicircular canal ampulla in the left ear. Charge balanced, biphasic current pulses were used to characterize responses to stimuli delivered via each electrode at various current levels, phase durations, and pulse rates. An Earth-vertical axis rotary chair was used to provide whole body, *en bloc* sinusoidal rotations of the subject in darkness over 0.1–2Hz at 100°/s peak velocity. Eye movements described in this report were recorded using 3DBinoc™ video-oculography goggles (Labyrinth Devices, LLC) pre-operatively, post-op/pre-activation, and over 8 weeks post-activation.

For Chapter 4, experiments were conducted with two female rhesus macaques in a protocol approved by the Johns Hopkins Animal Care and Use Committee. Detailed surgical, data acquisition, stimulus protocol, and data analysis techniques are outlined in the appropriate chapter (section 4.2). In brief, both animals were treated with ototoxic doses of gentamicin sufficient to cause severe drops in vestibulo-ocular reflex responses consistent with BVH and implanted in the left ear with an intralabyrinthine electrode array similar to that used in the MVI™ for humans but scaled down to fit rhesus anatomy. With the animals held stationary in darkness, patterns of pulsatile biphasic current pulses encoding waveforms of sinusoidal head angular velocity according to both a smooth pulse frequency modulation mapping (sPFM) and a mapping corrupted by temporal discretization (dPFM) typifying timing errors that would occur in a VI/CI that incorporates VI electrodes into a variant of the *continuous interleaved sampling* (CIS) stimulus strategy used in commercially available CIs. Biphasic current pulses were delivered to individual branches of the left vestibular nerve at sinusoidally modulated pulse frequencies to encode sinusoidal head motions with peak velocities of 50-400°/s and frequencies of 0.1-5Hz. Responses were assayed using 3D scleral search coil techniques. Stimuli were delivered using a MED-EL PULSAR CI100 stimulator interfaced with Research Interface Box hardware developed at the University of Innsbruck and a custom software package.

Chapter 2 Acute 3D Binocular Eye Movement Responses to Unilateral Semicircular Canal Stimulation in Humans

2.1 Introduction

Recent work advancing prosthetic electrical stimulation in human subjects [41–52] demonstrated promising evidence that acute prosthetic vestibular stimulation can produced modest electrically evoked eye movements approximately aligned with target canal axes. Both groups behind those studies used 2D video oculography to assay eye movements, preventing accurate measurement of each 3D component of evoked VOR responses. While 2D techniques provide insight into the effectiveness of prosthetic stimulation of vestibular afferents, those methods prevent estimation of spurious stimulation of non-target afferent nerve branches via measurement of 3D eye velocity components in anatomic canal coordinates.

Here we present data from the first four human subjects with BVH to undergo vestibular implantation and continuous motion-modulated prosthetic stimulation. Specifically, this chapter will describe electrically-evoked 3D vestibulo-ocular reflex (eeVOR) responses to acute presentations of pulse train stimuli targeting individual canal afferent nerve branches. Additionally, we measure 3D eye movement responses to the initial onset of constant-rate electrical stimulation with the head motionless. This experiment assays the evolution of adaptation to a sudden onset of electrical stimulation, revealing how prosthetic canal input drives acute vestibular compensation.

2.2 Methods

2.2.1 Study design

This study is a first-in-human, nonrandomized, self-controlled, longitudinal early clinical feasibility study to assess safety and tolerability of the Labyrinth Devices MVI™ vestibular implant system as a treatment for bilateral vestibular loss. A primary objective was assessment of changes in 3D VOR magnitude and alignment compared to pre-intervention status and archival data for normal human vestibular function. Inclusion criteria included age between 22-90 years old, summed responses to warm/cool caloric vestibular stimulation below 10°/s per ear, confirmation of normal ear and vestibular anatomy via MRI and CT, and sufficient hearing in the contralateral ear to support communication. All subjects must be ≥12 months post-onset and must have completed ≥6 months of vestibular rehabilitation therapy exercises while off vestibular-suppressant medications. Exclusion criteria included vestibular areflexia etiologies outside of the labyrinth, medical conditions that could impede a subject's ability to complete testing, or any medical contraindication to the planned surgery [53].

2.2.2 Subjects

Four adult subjects (2 men, 2 women) with BVH participated in this study. Prior to enrollment, subject MVI001 (male, 61 years old on entry into the study) received intravenous gentamicin for 14 days in 2012 for a leg injury. Post-aminoglycoside treatment, the subject reported symptoms of profound BVH which persisted for over 4 years following a plateau of compensation from rehabilitation therapy. The subject was implanted with the MVI™ system in the left ear in August 2016. Subject MVI002 (male, 57 years old) suffered from vertigo, imbalance, and oscillopsia in 2006 following spinal surgery. The subject was further treated with bilateral intratympanic streptomycin in 2007 and experienced symptoms consistent with BVH thereafter. On presentation to Johns Hopkins in 2016, the subject reported an incomplete recovery from vestibular rehabilitation exercises started in 2010. He underwent implantation of an MVI™ stimulator in his left ear in November 2016. Subject MVI003 (female, 63 years old) suffered from symptoms of BVH after 7 days of intravenous gentamicin treatment for a kidney stone urosepsis in 2015. The subject performed vestibular physical therapy for over a year without sufficient recovery and was implanted in her left ear with the MVI™ in February of 2017. Subject MVI004 (female, 62 years old) was treated for 14 days with gentamicin after an operation to treat a pelvic abscess in 2015. After the onset of BVH symptoms, she participated in vestibular therapy, which incompletely alleviated her symptoms. This subject's left ear was implanted with an MVI™ stimulator in December 2017.

2.2.3 Surgical procedure

Each subject was implanted with the receiver/stimulator component of a Labyrinth Devices MVI™ system in the left ear via a post-auricular incision and transmastoid approach similar to that typically used for cochlear implantation or labyrinthectomy, except that no entry was made into the cochlea and four ~0.75 mm diameter openings were made into the labyrinth's ampullae and common crus, via which electrodes were inserted. All surgeries were performed at the Johns Hopkins Hospital or the Johns Hopkins Outpatient Center by the same surgeon (Dr. Charles C. Della Santina). The receiver/stimulator (Figure 2.1A) was secured with suture in a bone well and sub-periosteal pocket in the left post-auricular region of the patient's head.

2.2.4 Labyrinth Devices MVI™ Multichannel Vestibular Implant System

The implanted stimulator component of the Labyrinth Devices MVI™ Multichannel Vestibular Implant System is a CONCERTO cochlear implant stimulator, modified by its manufacturer (MED-EL GmbH) for implantation in the semicircular canals (Figure 2.1A). The device includes an electrode array with nine stimulation electrode contacts, a stimulation reference electrode, a recording reference electrode, stimulator circuitry, three fixation magnets, and a coil antenna for transcutaneous inductive transmission of power and control signals. The electrode array (Figure 2.1B-D) comprises a total of 10 Pt/Ir electrodes: three electrodes (E3-E5) on a linear array implanted in the left posterior canal (Figure 2.1C); two linear arrays of three electrodes each, joined to form a forked array inserted into the left horizontal (E6-E8) and left anterior (E9-E11) ampullae (Figure 2.1D); and a separate Pt/Ir wire inserted into the common crus and used as the reference/return electrode for stimulus currents injected via E3-E11 (Figure 2.1B).

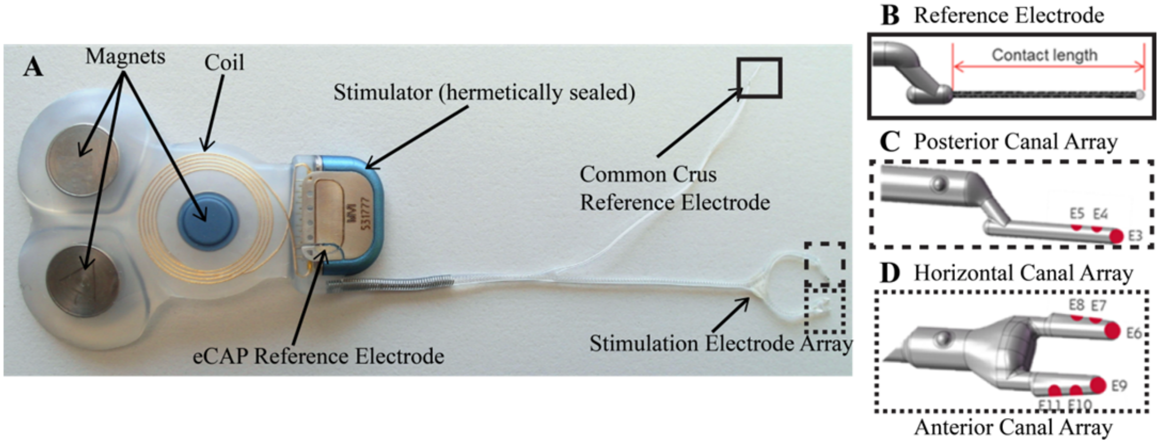

Figure 2.1. Labyrinth Devices Multichannel Vestibular Implant™ (MVI™) stimulator and electrode Array. (**A**) The Labyrinth Devices Multichannel Vestibular Implant™ (MVI™) stimulator comprises three fixation magnets, an inductive coil link, electrical current stimulator circuitry, a stimulation electrode array, and two reference electrodes (a stimulation reference electrode contact (**B**) and a recording reference electrode on the stimulator housing). (**C,D**) The MVI™ has two stimulation arrays: a linear array with three contacts implanted in the posterior canal (E3-E5, panel **C**) and a forked array with two shanks (**D**). The forked array is implanted into the horizontal (E6-E8) and anterior (E9-E11) canals. After characterization of electrically-evoked responses for each contact, only one electrode will be active within each shank. Multiple contacts on each stimulation array provide three options per canal. The stimulation reference electrode is implanted in the common crus of the vestibular labyrinth.

The implanted stimulator receives power and control signals from the external Head-Worn Unit (HWU, Figure 2.2B), which in turn receives commands from a lanyard-worn Power and Control Unit (PCU, Figure 2.2A). Magnetically held in place on the scalp over the implanted stimulator, the HWU uses a 6 degree-of-freedom motion sensor

(MPU6050, Invensense) to measure the subject's 3D angular head velocity and translational head acceleration. The PCU retains patient-specific device stimulation parameters, processes head movements, computes and dictates the timing of charge-balanced biphasic stimulus pulses, and provides power to the rest of the system from a rechargeable AA-sized battery.

Figure 2.2. Power and Control Unit (PCU) and Head Worn Unit (HWU). (**A**) The power and control unit (PCU) provides power via a AA battery and controls the signal processing of input gyroscopic data and output stimulation parameters. (**B**) The Head Worn Unit (HWU) magnetically couples to the MVI™ circuitry to supply power and control signals from the PCU to the stimulator via an inductive coil link. The HWU also houses a 6-DOF motion processing unit (MPU) to provide measurements of the 3D angular velocity of the subject's head while the device is active. (**C**) Subject MVI001 wearing the HWU coupled to the implanted stimulator.

Intralabyrinthine electrode array positioning was confirmed using a computed tomography (CT) scan of the subject's temporal bone 3 weeks post-implantation (Figure 2.3A, depicting a 3D reconstruction for subject MVI002). Oblique planar CT images displaying the stimulating electrode shanks in the left posterior (Figure 2.3B), left horizontal (Figure 2.3C), and left anterior (Figure 2.3D) canal ampullae verified proper implantation of the electrode arrays.

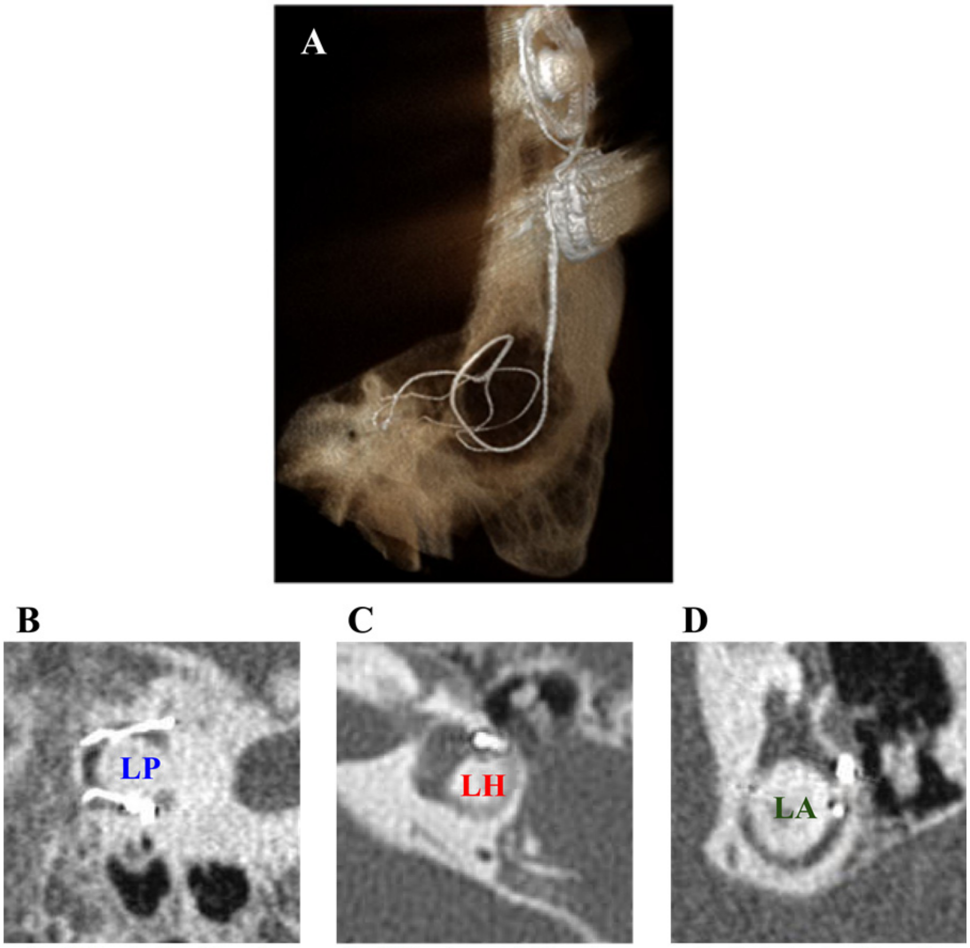

Left Posterior Canal Left Horizontal Canal Left Anterior Canal

Figure 2.3. CT Imaging of electrode array positioning in subject MVI002. (**A**) Post-operative CT 3D reconstruction for subject MVI002 with the stimulator. (**C**-D) Planar CT images outlining electrode shanks implanted in the (**B**) left posterior, (**C**) left horizontal, and (**D**) left anterior canals.

2.2.5 3D eye movement recording

Eye movements were recorded using the 3DBinoc™ video-oculography (VOG) goggles (Labyrinth Devices, LLC). This goggle set (Figure 2.4) uses a single camera to track binocular 3D eye position while illuminating the subject's eyes using infrared LEDs (allowing ocular tracking without visible light). The goggles assay horizontal and vertical components of eye position via pupil tracking and measure torsional angular position using iris pattern template matching [54]. Custom VOG software acquired 3D angular eye position data at 100 frames-per-second with a peak-to-peak noise floor of 0.15°, 0.07°, and 0.06° for the torsional, vertical, and horizontal 3D components, respectively (see section 6.2). The goggles use a pair of IR-pass optical filter insets to block the subject's view of visible light during data acquisition. 3DBinoc™ goggles interface with a host PC through a galvanically isolated USB connection and directly connect to each subject's PCU for stimulus trigger synchronization.

Figure 2.4. Subject MVI001 wearing the Labyrinth Devices 3DBinoc™ Goggles with IR-pass filter insets. This figure shows subject MVI001 wearing the 3DBinoc™ goggles during data acquisition on a custom bite-bloc. IR-pass optical filter insets are magnetically coupled to the goggles to occlude the subject's vision during experiments. The PCU can also be seen attached to a lanyard around the subject's neck.

2.2.6 Data analysis and statistics

The 3DBinoc™ system reports 3D angular position data as gaze direction (i.e., horizontal and vertical position of the pupil) and torsion around the eye's line-of-sight. We processed raw angular position data traces with third-order median filters to recover VOG tracking dropouts. 3D angular position data were converted to rotation vectors [55] and filtered with second or third order Savitsky-Golay filters [56] for high frequency noise rejection. We first computed 3D angular velocity in X ('roll'), Y ('pitch'), and Z ('yaw') head-fixed coordinates (Figure 2.5), then transformed angular velocity data into anatomic canal coordinates by applying a -45° passive reorientation of the head-fixed coordinate system about the yaw axis [57–60].

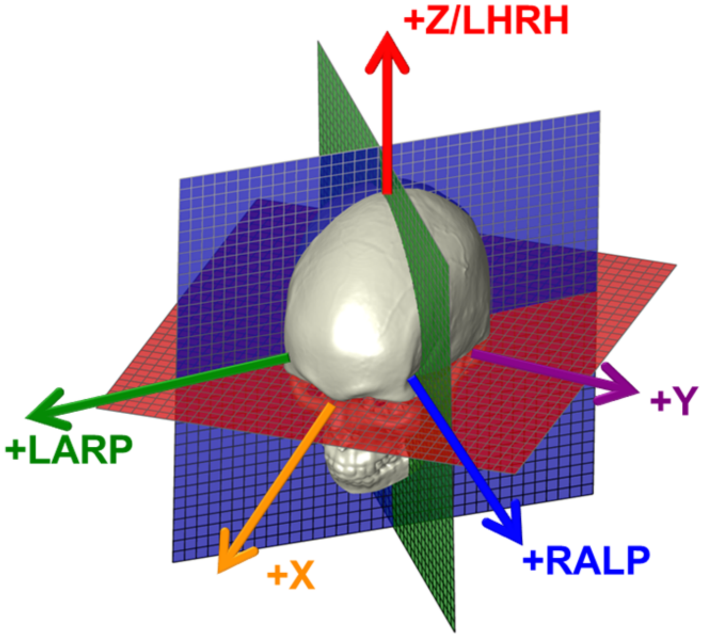

Figure 2.5. Head-fixed coordinate systems used to describe 3D vestibulo-ocular reflex (VOR) data. The +X ('roll', naso-occipital), +Y ('pitch', interaural), and Z (yaw, superoinferior) coordinates are mutually orthogonal stereotaxic axes. During data analysis, 3D angular position and velocity data are computed in skull coordinates and transformed into a canal coordinate system. Each subject's head is repositioned with a ~+20° pitch reorientation to align the +Z axis with the +LHRH axis [60].

A custom algorithm detected and omitted quick phases of vestibular nystagmus using an eye acceleration threshold and stitched across blanked regions using spline interpolation to produce smooth slow phase eye velocity traces. We computed cycle averages after removing trails corrupted by blinks or drops in pupil/iris tracking. Eye position data collected during adaptation to MVI™ activation were processed with custom software that fit a least-squares linear model to slow phase responses between auto-detected quick phases. The slope of the fitted line for each 3D component and corresponding angular position values was used to compute 3D angular velocity using standard rotational kinematic techniques [57]. All data are reported as mean values ± one standard deviation.

Tests of normality indicated most data residuals significantly deviated from a normal distribution (Anderson-Darling test, 95% CI). We used the aligned rank transform (ART) procedure [61–63] to perform a non-parametric multi-factorial repeated measures analysis of variance (ANOVA) and evaluate differences in evoked responses across each MVI condition. This was typically performed with factors of *MVI condition* ("Pre-operative", "Post-operative and pre-stimulation", "Modulation ON", and "Modulation OFF") and *Frequency* (0.1-2Hz). Post hoc pairwise comparisons were made using two-sided Wilcoxon rank sum tests. Statistical significance for all tests was set at $p < 0.05$.

2.2.7 Electrode characterization and activation

For pre-activation electrical stimulation characterization measurements, a 200pps pulse train was delivered to each electrode contact (with pulse train duration 200ms and inter-train-interval 300ms) to assay responses at each tested current level. Pulse train stimuli were first used to characterize perceptual thresholds, VOR thresholds, and maximum current levels for each tested electrode/phase duration combination (shown in Figure 6.1 of the Appendix). These data were used to generate 10 (MVI001 and MVI002) or 7 (MVI003 and MVI004) current amplitudes spanning the VOR threshold and maximum current level to assay acute 3D VOR responses during MVI™ stimulation (Table 2.1).

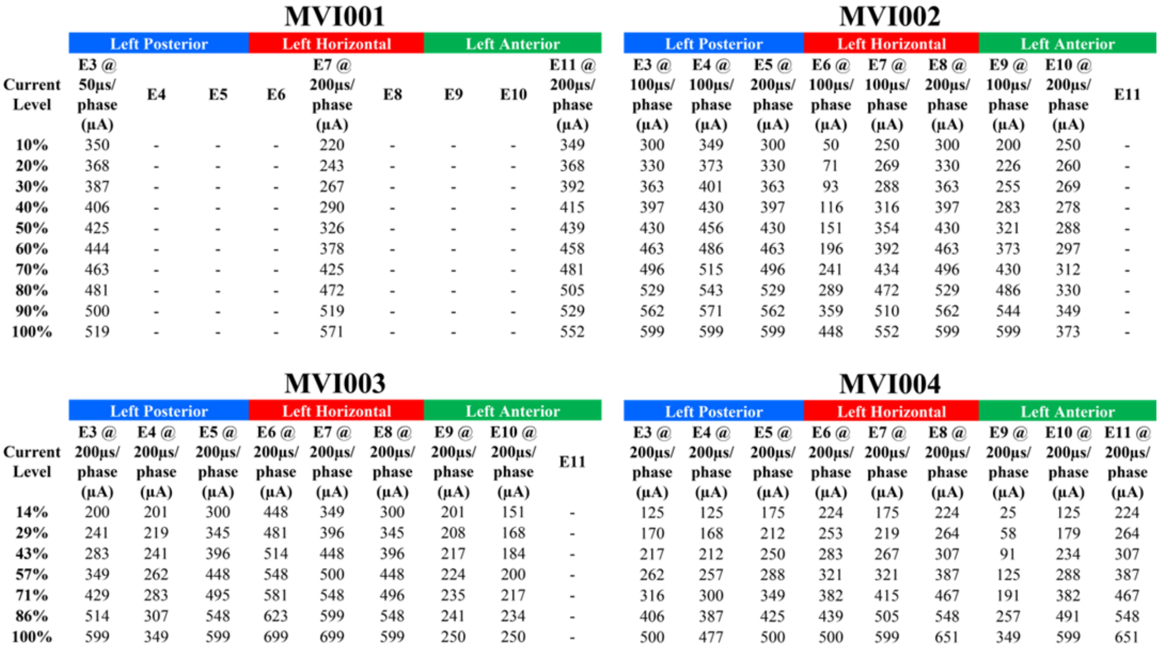

MVI001

Current Level	Left Posterior			Left Horizontal			Left Anterior		
	E3 @ 50µs/ phase (µA)	E4	E5	E6	E7 @ 200µs/ phase (µA)	E8	E9	E10	E11 @ 200µs/ phase (µA)
10%	350	-	-	-	220	-	-	-	349
20%	368	-	-	-	243	-	-	-	368
30%	387	-	-	-	267	-	-	-	392
40%	406	-	-	-	290	-	-	-	415
50%	425	-	-	-	326	-	-	-	439
60%	444	-	-	-	378	-	-	-	458
70%	463	-	-	-	425	-	-	-	481
80%	481	-	-	-	472	-	-	-	505
90%	500	-	-	-	519	-	-	-	529
100%	519	-	-	-	571	-	-	-	552

MVI002

Current Level	Left Posterior			Left Horizontal			Left Anterior		
	E3 @ 100µs/ phase (µA)	E4 @ 100µs/ phase (µA)	E5 @ 200µs/ phase (µA)	E6 @ 100µs/ phase (µA)	E7 @ 100µs/ phase (µA)	E8 @ 200µs/ phase (µA)	E9 @ 100µs/ phase (µA)	E10 @ 200µs/ phase (µA)	E11
10%	300	349	300	50	250	300	200	250	-
20%	330	373	330	71	269	330	226	260	-
30%	363	401	363	93	288	363	255	269	-
40%	397	430	397	116	316	397	283	278	-
50%	430	456	430	151	354	430	321	288	-
60%	463	486	463	196	392	463	373	297	-
70%	496	515	496	241	434	496	430	312	-
80%	529	543	529	289	472	529	486	330	-
90%	562	571	562	359	510	562	544	349	-
100%	599	599	599	448	552	599	599	373	-

MVI003

Current Level	Left Posterior			Left Horizontal			Left Anterior		
	E3 @ 200µs/ phase (µA)	E4 @ 200µs/ phase (µA)	E5 @ 200µs/ phase (µA)	E6 @ 200µs/ phase (µA)	E7 @ 200µs/ phase (µA)	E8 @ 200µs/ phase (µA)	E9 @ 200µs/ phase (µA)	E10 @ 200µs/ phase (µA)	E11
14%	200	201	300	448	349	300	201	151	-
29%	241	219	345	481	396	345	208	168	-
43%	283	241	396	514	448	396	217	184	-
57%	349	262	448	548	500	448	224	200	-
71%	429	283	495	581	548	496	235	217	-
86%	514	307	548	623	599	548	241	234	-
100%	599	349	599	699	699	599	250	250	-

MVI004

Current Level	Left Posterior			Left Horizontal			Left Anterior		
	E3 @ 200µs/ phase (µA)	E4 @ 200µs/ phase (µA)	E5 @ 200µs/ phase (µA)	E6 @ 200µs/ phase (µA)	E7 @ 200µs/ phase (µA)	E8 @ 200µs/ phase (µA)	E9 @ 200µs/ phase (µA)	E10 @ 200µs/ phase (µA)	E11 @ 200µs/ phase (µA)
14%	125	125	175	224	175	224	25	125	224
29%	170	168	212	253	219	264	58	179	264
43%	217	212	250	283	267	307	91	234	307
57%	262	257	288	321	321	387	125	288	387
71%	316	300	349	382	415	467	191	382	467
86%	406	387	425	439	505	548	257	491	548
100%	500	477	500	500	599	651	349	599	651

Table 2.1. Pulse amplitudes used for current fitting experiments. This table outlines the current amplitudes and phase durations used in current fitting experiments for all tested electrodes. Each current level listed was tested using a pulse train that oscillated from 200 to 0pps for 200 and 300ms, respectively. Each current level intensity series was determined by linearly interpolating points between a level right below each subject's perceptual threshold and their maximum tolerable level, separately for each electrode and phase duration. Subjects MVI001 and MVI002 were tested with 10 levels for each electrode/phase duration pair, where MVI003 and MVI004 were tested with 7 levels due to time constraints.

Following electrode characterization, a stimulation parameter set (including electrode contact, current amplitude, and phase duration) was programmed into the subject's PCU for each canal. Stimuli were chosen to optimize evoked VOR magnitude and response alignment with target canal anatomic axes (Table 2.2). Device activation (including adaptation to baseline tonic electrical stimulation) was performed with the subject on a bite-block in total darkness. Each active electrode was programmed to provide biphasic, charge balanced current pulses at 100pps on all three active canal channels.

The nystagmus evoked by the onset of stimulation was measured in darkness for 1 minute, after which the lights in the experimental room were turned on and the IR-pass filters removed from the 3DBinoc™ goggles for 4 minutes. When in light the subject was instructed to focus on an Earth-fixed target to promote adaptation to prosthetic baseline stimulation via retinal slip error signals during the evoked nystagmus. This procedure (1 minute in darkness to assay vestibular nystagmus responses and 4 minutes to promote adaptation) was repeated until all components of the spontaneous nystagmus in darkness were <5°/s. Subjects MVI002, MVI003, and MVI004 were later adapted to a 150pps baseline pulse rate on the same day.

2.3 Results

2.3.1 3D oculography reveals conjugate binocular vestibulo-ocular reflex responses aligned with the implanted canal, consistent with selective activation of vestibular nerve branches

Electrode contacts were characterized using 20 cycles of a 2Hz-modulated pulse train stimulus that alternated in pulse rate between 200 pulses-per-second (pps) and 0pps for 200 and 300ms, respectively. This stimulus was used to test 3D VOR responses to individual current amplitudes using biphasic, charge balanced current pulses while assaying 3D eye movements in darkness with the subject's head held stationary on a bite-block. Pulse amplitude was varied between the minimum current level that evoked a discernible eye movement up to the maximum level that was tolerable for the subject and maintained a consistent motion percept, determined separately for each electrode contact and pulsatile phase duration tested. The maximum level was determined by slowly incrementing the current amplitude with the subject reporting his/her percepts to detect spurious stimulation of auditory afferents (perceived as tinnitus), facial nerve fibers (causing facial twitch, tearing, ear canal discomfort or phantom taste sensation), non-target vestibular structures (producing percepts of head translation or change in axis of rotation), or any other undesired effect of current spread.

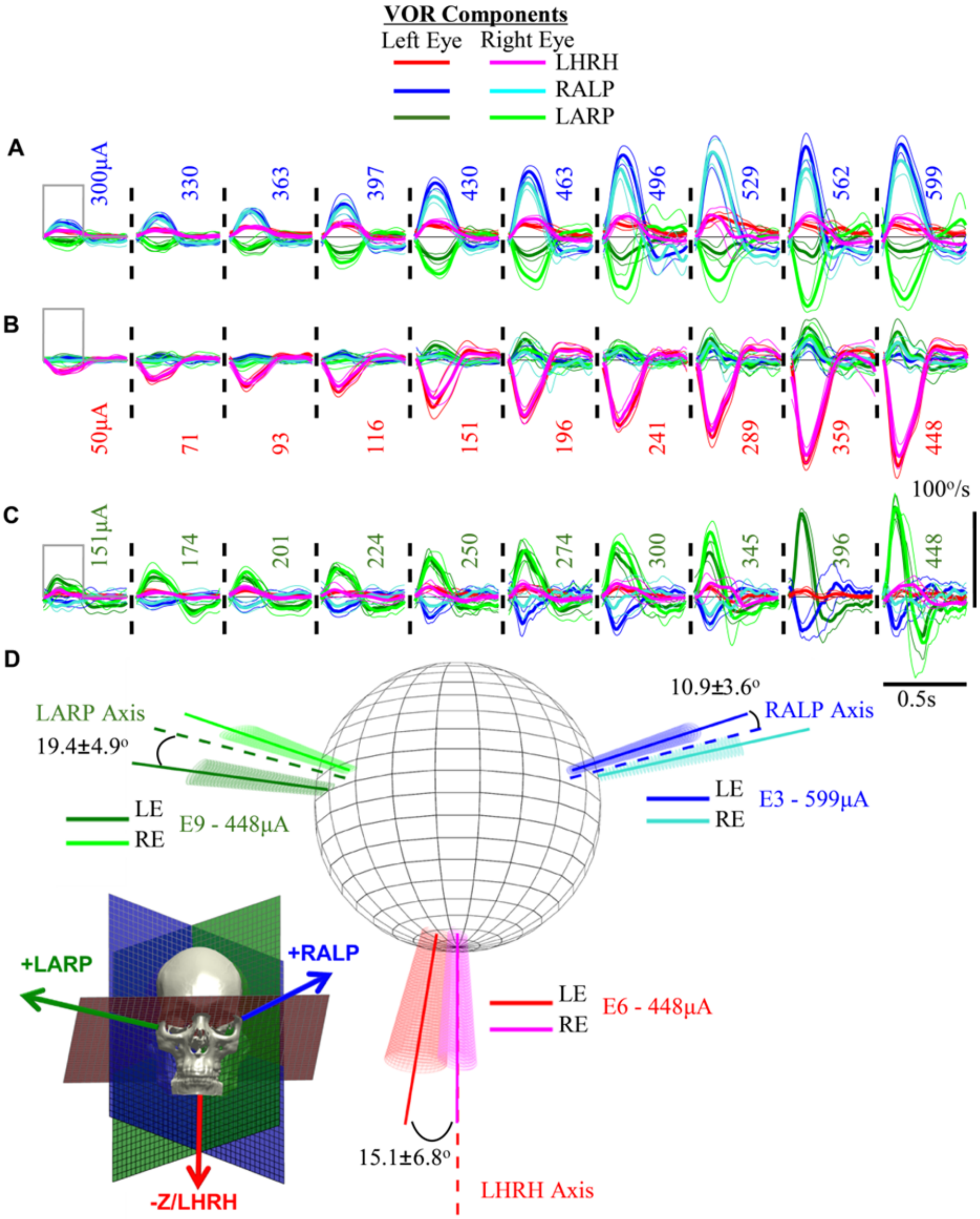

Figure 2.6. MVI™ stimulation evokes vestibulo-ocular reflex (VOR) responses aligned with the intended semicircular canal. 3D VOR responses from MVI002 during pulse train stimuli using biphasic, charge balanced 100μs/phase current pulses. Cycle averaged binocular eye velocity traces are plotted for a 2Hz, 40% duty cycle pulse train stimulus from 0 to 200pps. (**A**) Stimulation of electrode E3 in the left posterior canal ampulla with pulse amplitudes from 300-599μA. (**B**) Stimulation of electrode E6 in the left horizontal canal with pulse amplitudes from 50-448μA. Excitation of the left horizontal ampullary nerve produces a rightward slow phase eye velocity (negative by convention). (**C**) Stimulation of electrode E9 in the left anterior canal at with pulse amplitudes from 151-448μA. Note that the right eye response for the 396μA stimulus condition is missing due to a loss of VOG tracking. (**D**) Each vector depicts the mean axis of rotation during the peak excitatory eye velocity for the current amplitude listed in the legend. Elliptical conic regions surrounding each eye velocity axis vector are computed from an eigenvalue decomposition of the 3D angular velocity covariance matrix. Anatomic canal axes of rotation are plotted as dashed lines.

Ideally, prosthetic stimulation delivered via an electrode implanted in and targeting a given canal should elicit 3D VOR responses for the two eyes that align with each other and with the target canal's anatomic axis. To varying degrees, this ideal was achieved for at least one electrode in every canal of every subject. Cycle-averaged binocular eeVOR responses from subject MVI002 using 100μs/phase current pulses were robust and grew with increasing current amplitude (Figure 2.6A-C). Stimuli delivered via electrode E3 in the left posterior canal (Figure 2.6A) produced a strong RALP component in both eyes, while an unintended LARP component grew in the right eye. When assaying electrode E6 in the left horizontal canal (Figure 2.6B) the evoked eye movements rotated about an axis that closely approximated a pure horizontal eye movement. Lastly, testing electrode E9 in the left anterior canal (Figure 2.6C) produced eye movements well aligned with the intended LARP axis for the subject's right eye with a slightly misaligned eye movement in the left eye. When plotting the 3D angular velocity axis of rotation of responses evoked from the largest currents tested for each electrode/canal (Figure 2.6D), alignment between eeVOR response vectors and the intended anatomic canal axes illustrates that MVI™ stimulation can provide approximately selective activation of individual primary afferent nerve branches.

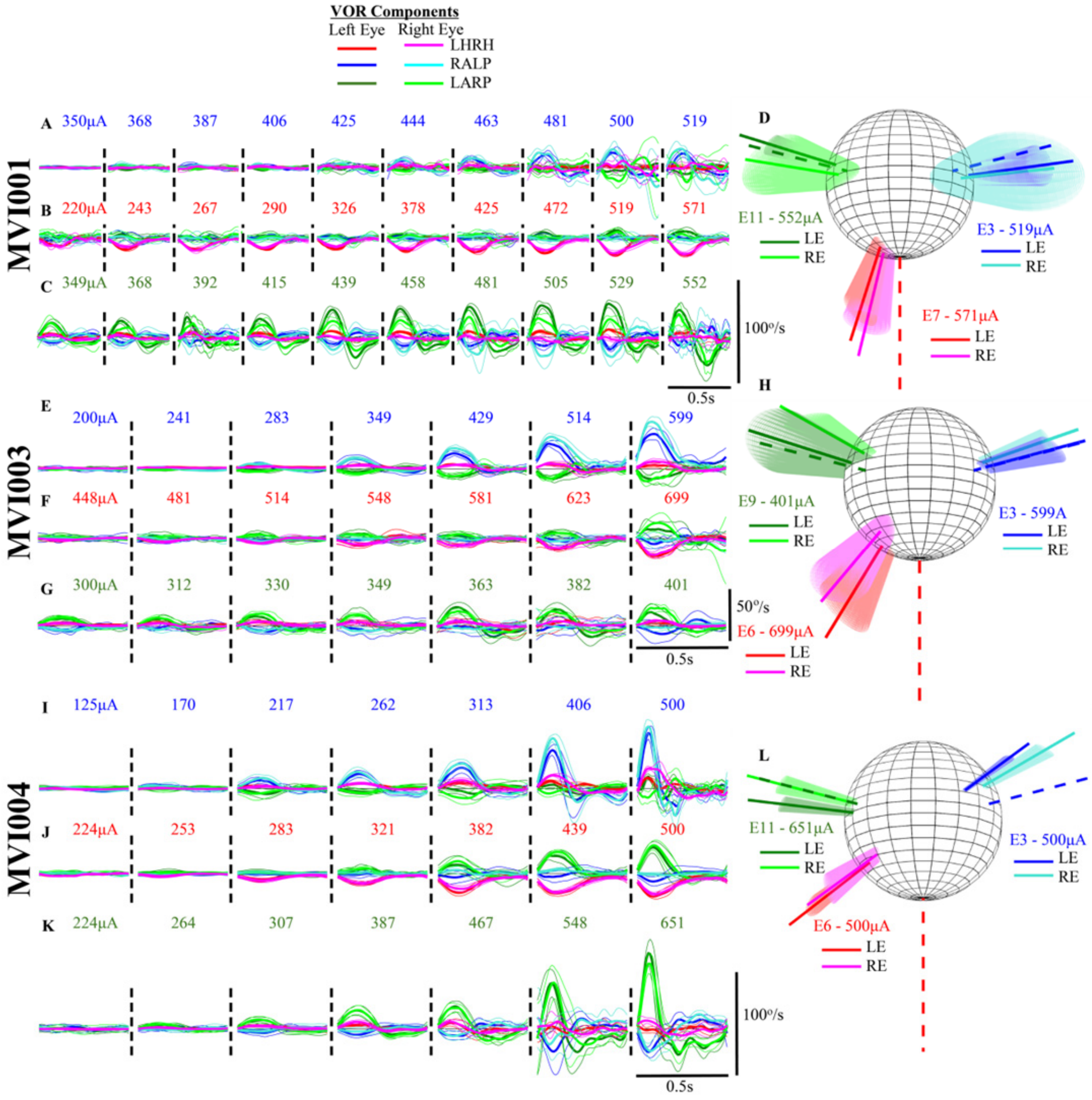

Figure 2.7. Binocular 3D Responses from subjects MVI001, MVI003, and MVI004. Binocular cycle averaged 3D slow phase eye velocity traces in response to 2Hz, 40% duty cycle pulse trains oscillating between 200pps (200ms) and 0pps (300ms). Pulse trains where delivered to isolated electrode contacts on subjects MVI001 (**A-D**), MVI003 (**E-H**), and MVI004 (**I-L**). For subject MVI001, pulse trains delivered to (**A**) electrode E3 using 50μs/phase biphasic current pulses, (**B**) electrode E7 using 200μs/phase, and (**C**) electrode E11 using 200μs/phase pulses produced canal specific responses. The axis of rotation of the eye movement evoked by the maximum current level for each of the three electrodes is plotted in (**D**). When tested on electrodes (**E**) E3, (**F**) E6, and (**G**) E9 using 200μs/phase current pulses, subject MVI003 produced eye movements well aligned with the left posterior and left anterior canals. Stimuli delivered to the left horizontal canal produced a response consistent with activation of the left horizontal ampullary nerve and spurious stimulation of the left anterior canal, depicted graphically in (**H**). Lastly, subject MVI004 produced similar responses when tested on electrodes (**I**) E3, (**J**) E6, and (**K**) E11 using 200μs/phase current pulses, where stimulation of electrode contacts in the left anterior and left posterior ampullae produced well aligned responses, while stimulation in the horizontal canal produced a mixed LHRH/LARP response.

Using 50µs/phase pulses on E3 (Figure 2.7A) and 200µs/phase pulses on E7 and E11 (Figure 2.7B, C), subject MVI001 produced modest eye movements consistent with activation of the left posterior, left horizontal, and left anterior ampullary nerves, respectively. Eye movements from subject MVI003 using 200 µs/phase pulses with electrodes in the left posterior (E3, Figure 2.7E), left horizontal (E6, Figure 2.7F), and left anterior (E9, Figure 2.7G) canal ampullae produced eye movements rotating about axes approximating the target canal axes for most current levels tested. Stimulation via electrode E6 (Figure 2.7F) evoked a predominantly horizontal eye movement until the current was increased to 699µA, where the off-axis LARP component grew causing a decrease in response alignment. Adjusting stimulation parameters to reduce current amplitude can reduce this off-axis component, typically at the expense of minimized response magnitude. Responses from subject MVI004 during stimulation of electrode E3 in the left posterior canal (Figure 2.7I), electrode E6 in the left horizontal canal (Figure 2.7J), and electrode E11 in the left anterior canal (Figure 2.7K) with 200µs/phase pulses produced well aligned responses to stimulation of the left posterior and left anterior canals, while trials assaying electrodes in the horizontal canal also produced a mixed response consistent with simultaneous excitation of the left horizontal and anterior ampullary nerves.

Current fitting experiments with subject MVI002 produced robust, selective eye movement responses (Figure 2.8) across all tested electrodes (E11 was not assayed due to high electrical impedance suggesting wire breakage during implantation). Response velocities tended to grow monotonically with increased current amplitude, a pattern observed in responses of all subjects (Figure 2.9). For MVI002, the electrode contact on the tip of each shank produced the largest eye velocity magnitudes compared to the other two contacts within each canal (Figure 2.8A-C). To assess the relative alignment of the mean binocular axis of rotation (i.e., the average of both unit vectors describing the axes of rotation for each eye) and the targeted anatomic canal axis, we monitored the angle between these two axes (Figure 2.8D-F). Overall, electrodes in MVI002's horizontal canal (Figure 2.8E) produced better alignment with the anatomic canal axis compared to electrodes in the left posterior (Figure 2.8D) and left anterior (Figure 2.8F) canals. Additionally, quantifying disconjugacy (i.e., the angle between the left and right eyes' 3D axes of rotation) showed ocular responses to horizontal stimulation (Figure 2.8H) produced eye movements better aligned between both eyes compared to stimulation of electrodes in the left posterior (Figure 2.8G) and left anterior (Figure 2.8I) canals, where interocular disconjugacy grew as the current level increased.

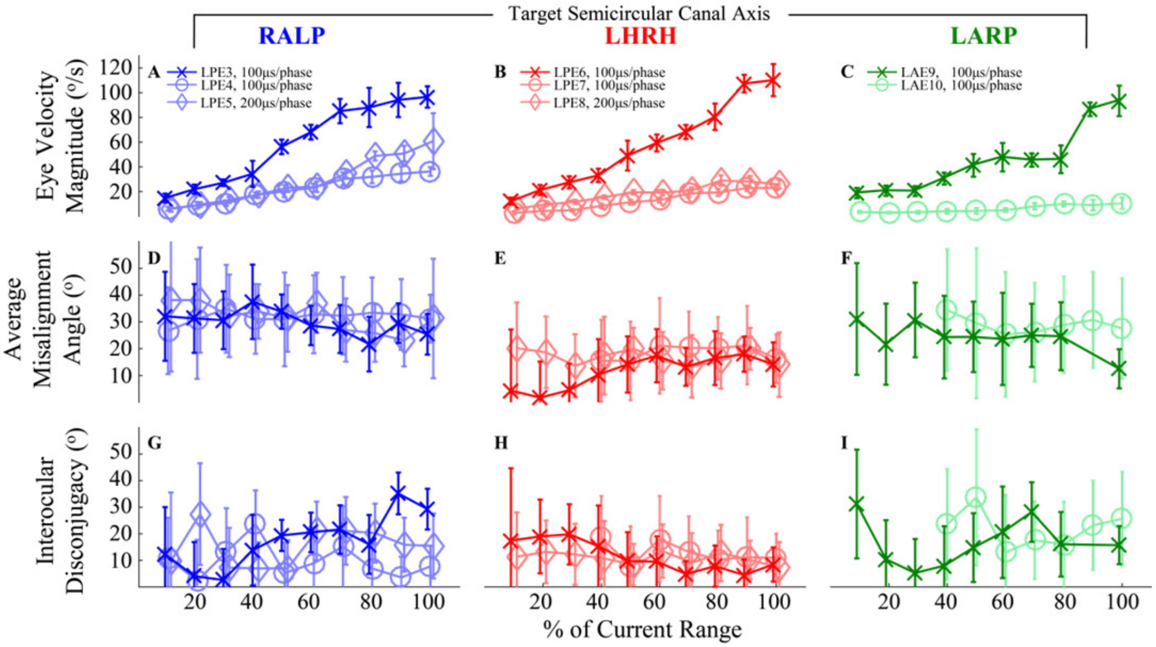

Figure 2.8. Electrode characterization produces selective, conjugate eye movements. Each electrode contact was characterized using a 2Hz, 40% duty cycle pulse train stimuli from 0 to 200pps for subject MVI002. E11 was not tested due to a high electrical impedance (>25kΩ). Electrode contacts chosen for device activation are bolded. (**A, B, C**) Peak excitatory slow phase velocity of the left eye as a function of % current amplitude intensity. A current intensity of 10% corresponds to the per-electrode minimum current amplitude that evoked an eye movement response, while an intensity of 100% represents the maximum current amplitude tested for that electrode contact/phase duration. See Table 2.1 for the complete mapping of per-electrode current intensity to pulse amplitude in µA for each subject. (**D, E, F**) The misalignment angle plotted as a function of current amplitude intensity, where misalignment is computed as the angle between the mean binocular axis of rotation and the intended canal axis of rotation. (**G, H, I**) The binocular disconjugacy is plotted as the angle between the mean VOR rotation axes of the left and right eye as a function of current intensity. Responses with peak eye velocities <5°/s were too small to provide accurate estimates of response misalignment or interocular disconjugacy and are not displayed in the figure.

Subject MVI001 was only comprehensively tested on E3 in the left posterior canal, E7 in the left horizontal canal, and E11 in the left anterior canal due to time constraints. Each electrode produced canal-aligned responses with 20-40°/s peak velocities when tested up to the maximum current level (Figure 2.9A-C). Subject MVI003 (Figure 2.9D-F) was tested on 8 of the 9 electrode contacts; E11 was not tested because she reported that stimulation via that electrode caused discomfort in the area of the left temple. Like MVI002, subject MVI003 exhibited eye movements that rotated about axes approximating their target canal axes, but MVI003's responses had smaller peak eye velocities (17-33°/s). Tests of all 9 electrodes in subject MVI004 produced peak eye movements up to 65°/s in the intended canal plane when stimulated with the largest comfortable current for each contact (Figure 2.9G-I). For this subject, electrodes in the left anterior and left posterior canals produced large amplitude peak eye velocities (~60-70°/s) with low misalignment angles at the higher current levels (~14-17°), consistent with selective stimulation of the target ampullary nerve branches. Stimulation via electrodes implanted in MVI004's left horizontal ampulla (E6-E8, Figure 2.9G middle) elicited responses with lower velocities (~30°/s) and greater misalignment (up to ~55°). All horizontal canal electrodes in this subject produced a LARP component that grew in amplitude with the LHRH component as the current level increased, consistent with cycle averaged responses (Figure 2.9J) and likely due to current spread exciting the LA ampullary nerve.

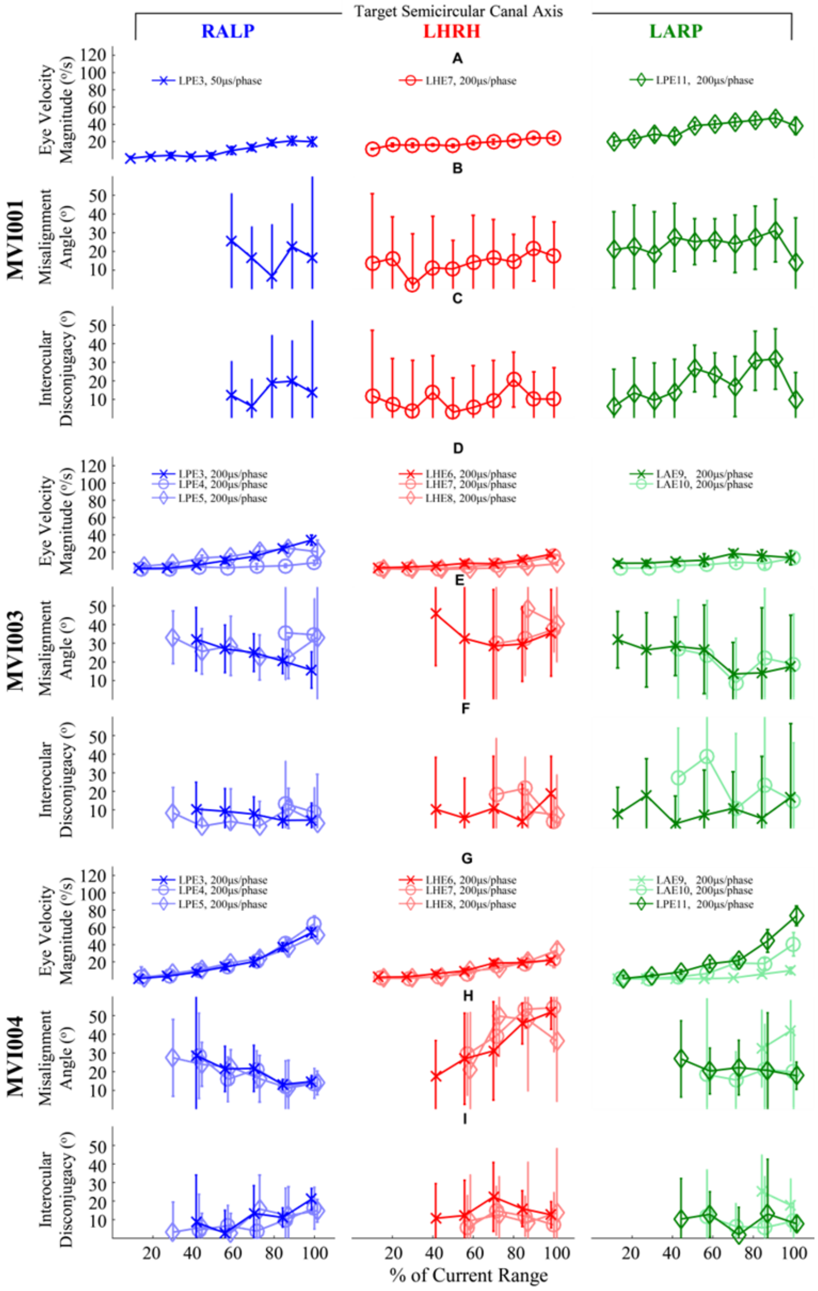

Figure 2.9. Current fitting summaries for subjects MVI001, MVI003, and MVI004. Electrode contacts chosen for continuous motion-modulated stimulation for the longitudinal portion of this study are bolded and others are faded. (**A-C**) MVI001 was only thoroughly tested on electrodes E3, E7, and E11 in the left posterior, left horizontal, and left anterior canals respectively due to restricted time. (**D-F**) Subject MVI003 produced eye movements that approximated the target canal axis of rotation, with overall smaller amplitude velocities compared to MVI002. (**G-I**) MVI004 produced strong eye movements during stimulation of electrodes in the left posterior and left anterior canals (G, left and right) that were consistent with selective stimulation of their respective ampullary nerve branches. Stimulation of electrodes in the left horizontal canal (H, middle) produced eye movements with a large LARP component (as seen in Figure S1J). All stimulus parameters are listed in Table 2.1.

2.3.2 Initial onset of constant-rate stimulation produced nystagmus with yaw and pitch components decaying within 5 minutes and more persistent roll responses

Biphasic, charge-balanced stimulus pulses like those delivered by the MVI™ (and all other related neural prostheses, including cochlear implants) are exclusively excitatory, so the only way for a unilaterally-implanted MVI™ to encode both excitatory (ipsiversive) and inhibitory (contraversive) head rotations is to modulate excitatory stimulation rate and/or current above and below a continuous, non-zero electrical stimulus. Over time the vestibular central nervous system can learn to associate this tonic stimulation with the absence of head motion through neuronal plasticity mechanisms analogous to those enlisted during recovery after unilateral injury [64]. Abruptly initiating this tonic stimulus causes a sudden-onset asymmetry of tonic input to vestibular nuclei (VN), which under normal circumstances continuously computes a difference signal comparing input from coplanar pairs of canals in the two labyrinths to determine the presence, axis and direction of head rotation. Although onset of electrical stimulation would produce an *increase* in tone from the implanted side, the VN can be expected to respond as they would after a sudden contralateral *decrease* in vestibular tone, as often occurs with onset of nystagmus and vertigo due to Ménière's disease attacks, vestibular neuritis, or destructive treatment such as a chemical labyrinthotomy, surgical labyrinthectomy, or vestibular neurectomy [65,66]. In the setting of those unilaterally disabling or destructive events, abrupt onset of vestibular tone asymmetry typically causes vertigo, nausea and "spontaneous" nystagmus about an axis aligned with the vector sum of the 3 intact canal's axes scaled by their relative levels of activity [3]. The extent and duration of vertigo and nystagmus caused by an analogous asymmetry immediately after onset of tonic prosthetic stimulation are likely to determine whether MVI™ activation requires hospitalization or can be performed in a much more cost-efficient outpatient setting.

Few published data are available to support estimation of time required for humans to adapt to an initial onset of tonic prosthetic vestibular stimulation. In four guinea pigs [26,28], nystagmus beat frequency dropped to <10% of its peak within 5-120 min after activation onset, but nystagmus persisted in some animals for more than 24 hours. In one human [42], horizontal nystagmus persisted for ~30 min after initial onset of tonic input. The wide variation within and between species in those published data might represent species-specific differences but could also depend on differences in stimulation intensity, events immediately prior to onset of tonic stimulation and the visual scene displayed during adaptation. Given that yaw and pitch nystagmus components move the image of a small, frontal visible target off the retinal fovea while roll nystagmus would not, the time course of nystagmus decay should depend on the visual scene, eye position and differential rates of decay of different 3D VOR components. The previously published data for human subjects were recorded using 2D oculography [42], which did not measure roll/torsional eye motion and cannot differentially quantify adaptation dynamics for the three components of the 3D VOR.

	Subject ID	**MVI001**	**MVI002**	**MVI003**	**MVI004**
	Date	09/07/2016	11/30/2016	02/23/2017	01/05/2018
RALP	Electrode ID	E3	E3	E3	E3
	Phase Dur. [us/phase]	50	100	200	200
	Pulse Amp. [uA]	390	600	600	406
	Pulse Rate [pps]	100	100	100	100
LHRH	Electrode ID	E7	E6	E6	E6
	Phase Dur. [us/phase]	200	100	200	200
	Pulse Amp. [uA]	570	160	620	320
	Pulse Rate [pps]	100	100	100	100
LARP	Electrode ID	E11	E9	E9	E11
	Phase Dur. [us/phase]	200	100	100	200
	Pulse Amp. [uA]	480	600	400	550
	Pulse Rate [pps]	100	100	100	100

Table 2.2. Electrical stimulation parameters used during device activation. Stimulation parameters used during activation onset of stimulation in all three canals for all subjects. The table lists the active electrode contact number, phase duration, pulse amplitude, and stimulus pulse rate for each channel. Note, baseline pulse rates for subjects MVI002, MVI003, and MVI004 on all channels were increased to 150pps after device activation. Details of map types are outlined in section 3.2.1.

Three weeks post-implantation, each subject experienced initial onset of tonic electrical stimulation presented concurrently but asynchronously to the three canal ampullae. A single electrode producing the most robust, well aligned responses on each shank was chosen as the “active” electrode for each canal (bold traces in Figure 2.8 and Figure 2.9, and listed in Table 2.2). Additionally, phase duration and current amplitude for each active channel was chosen to maximize the evoked eye velocity and minimize the spurious activation of non-target vestibular neural structures. A 3DBinoc™ VOG system recorded eye movement responses to characterize the time course of adaptation throughout the procedure. With the subject’s head held stationary using a bite-block, the test environment was darkened by turning off room lights and blocking the subject’s vision using visible-light blocking optical filters to isolate the vestibular contribution to the observed eye movements. After the onset of electrical stimulation (black bar at top of

Figure 2.10, and insets 4A-C), ocular responses were monitored for ~1 minute in darkness (Figure 2.10, gray regions). The filters were then removed, the testing room lights turned on, and the subject was instructed to fixate on an Earth-fixed target to aid compensation to the applied tonic stimulus for ~4 minutes (Figure 2.10, sections with a white background).

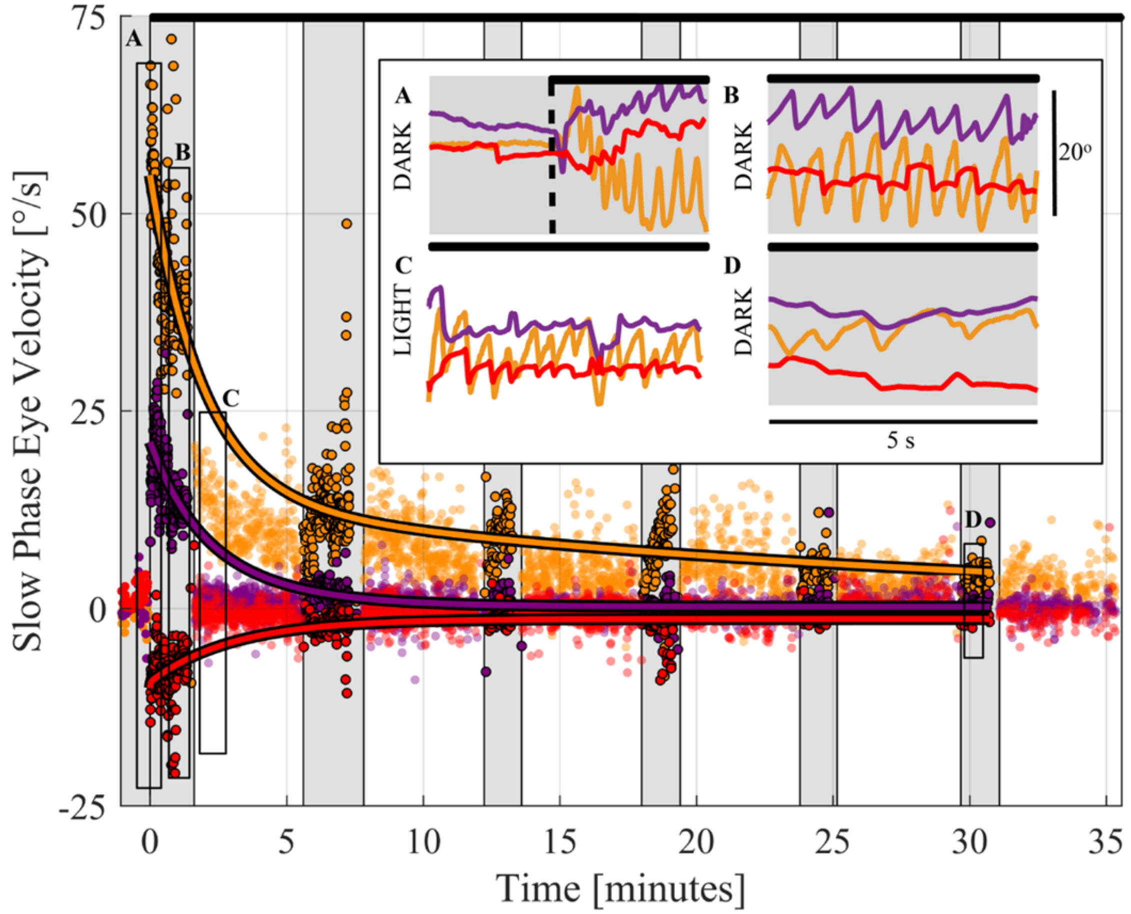

Figure 2.10. Activation of MVI™ stimulation produced a robust nystagmus that decayed within 30 minutes. 3 weeks post-implantation, subject MVI002 was activated with continuous stimulation. With the subject's head stable on a bite-block, electrical stimulation was initiated at 100pps on a single electrode contact in the left posterior canal (E3 at 599µA), the left horizontal canal (E6 at 151µA), and the left anterior canal (E9 at 599µA) using 100µs/phase biphasic, charge balanced current pulses (black bar at top of figure). Eye movements were monitored for ~1 minute in darkness. The subject was then put into a lighted environment for ~4 minutes and instructed to focus on an earth fixed target. This pattern (1 minute in dark, ~4 minutes in light) was repeated for >35 minutes. The slow phase 3D left eye velocity is plotted as a function of time throughout the adaptation process. Second order exponential fits of the data collected in darkness produced dominant time constant estimates of 28.2, 3.33, and 3.0 minutes for the roll, pitch and yaw 3D components, respectively. (RMSE_X = 6.6°/s, RMSE_Y = 2.7°/s, RMSE_Z = 2.7°/s). (**A**) The onset of electrical stimulation produced a robust nystagmus dominated by a positive slow phase torsional component. (**B**) By the end of the first minute of electrical stimulation in darkness, the horizontal component of the eye movement had diminished near zero, while the slow phase velocity of the vertical and torsional components sustained a positive slow phase nystagmus. (**C**) When the lights in the testing room were turned on and the subject was allowed to view an Earth-fixed target, the vertical component of the ocular response diminished. The torsional component of the evoked eye movement remained at ~18°/s. (**D**) By the fifth session in darkness (after ~30 minutes of prosthetic stimulation) the torsional eye velocity had reduced to ~5°/s, while the vertical and horizontal components were both near zero.

This procedure was repeated every 5 minutes for >35 minutes to assay the time course of adaptation to tonic stimulation. For subject MVI002, this initially evoked a nystagmus with positive roll (clockwise from the subject's viewpoint), positive pitch (downward), and negative yaw (rightward) slow phase eye velocity components (Figure 2.10A). This result is consistent with excitation of the entire left vestibular labyrinth (assuming the positive pitch component is due to left posterior canal excitation exceeding left anterior canal excitation and/or to a roll deviation of the implanted labyrinth's orientation from that assumed in the analysis). After ~1 minute in darkness, nystagmus was still present, though reduced in slow phase velocity (Figure 2.10B). Immediately after room lighting was restored and the subject attempted to fixate a dot on the wall 1.9m in front of the subject's nose, yaw and pitch nystagmus components became small, while roll slow phase velocity remained at ~18°/s (Figure 2.10C). After about 30 minutes of dark/lighting cycling, the roll nystagmus component in darkness fell to <5°/s, a level the yaw and pitch components reached within the first few minutes (Figure 2.10D). Subjects MVI001, MVI003, and MVI004 produced similar results, with onset of stimulation eliciting robust nystagmus that decayed within 30 minutes for the roll component and more quickly for the yaw and pitch components (Figure 2.11). Second order exponential fits of the roll component of nystagmus in darkness yielded dominant time constants of 1.5, 28.2, 7.8, and 9.6 minutes for subjects MVI001, MVI002, MVI003, and MVI004, respectively (RMSE = 3.1, 6.6, 1.7, and 2.5°/s, respectively).

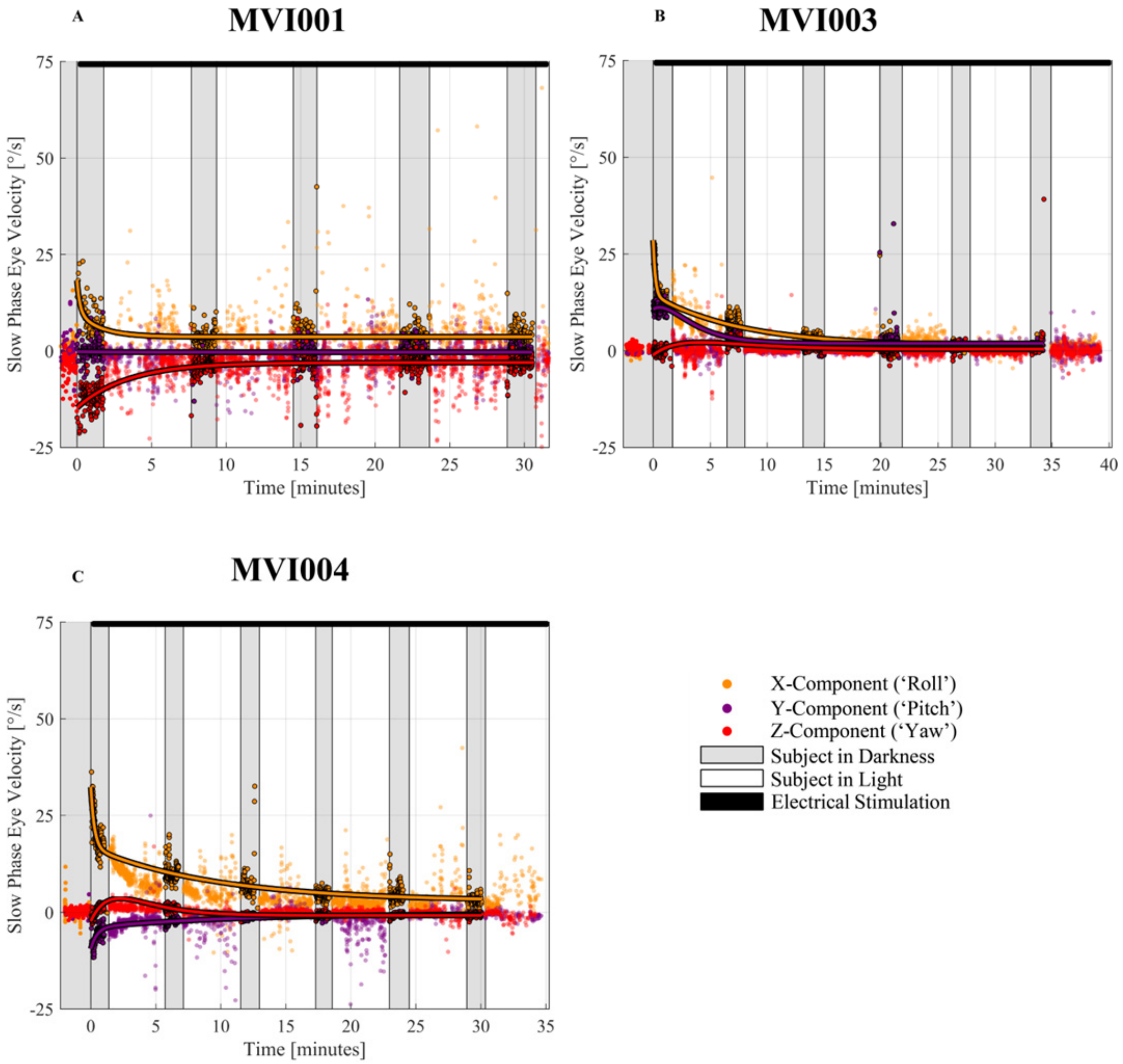

Figure 2.11. MVI001, MVI003, and MVI004 adaptation to constant-rate and -current electrical stimulation. Subjects (**A**) MVI001, (**B**) MVI003, and (**C**) MVI004 all produced nystagmus responses to the onset of prosthetic vestibular stimulation delivered to electrodes in each canal that decayed to imperceptible levels within ~30 minutes. (**A**) Subject MVI001 produced a brisk nystagmus that decayed within the first minute in darkness. (**B**) Subject MVI003 produced a positive roll component that decreased rapidly within the first minute in darkness. The subject also produced a positive pitch component in addition to the positive roll component, consistent with a higher level of evoked activity in the left posterior ampullary nerve branch relative to the left anterior nerve group. Also, this subject and subject (**C**) MVI004 produced a nystagmus with a small negative (~-3°/s) yaw component that reversed direction within the first minute in darkness. This finding is consistent with reversal phases of evoked nystagmus during sustained vestibular stimulation. Second order exponential fits of slow phase velocity data acquired in darkness revealed dominant roll time constants of 1.5, 7.8, and 9.6 minutes (RMSE = 3.1, 1.7, and 2.8°/s) for MVI001, MVI003, and MVI004, respectively.

2.4 Discussion

Acute measurements of electrically-evoked 3D VOR responses to prosthetic stimulation of primary afferent nerve branches in 4 human subjects reveal that use of the Multichannel Vestibular Implant™ system is a tolerable, effective, and overall a safe potential treatment for BVH. Binocular 3D video-oculography data collected during stimulation via 9 electrodes in each subject's implanted labyrinth (Figure 2.6-Figure 2.9) show that MVI™ stimulation can semi-selectively activate each of the vestibular nerve's ampullary branches. These first-in-human 3D data are therefore consistent with prior 3D oculography in animals [30–38] and 2D measurements in humans [41–52].

This result indicates that surgical placement of each stimulation array is spatially aligned with target canal nerve branches, allowing prosthetic vestibular stimulation evoke compensatory, directionally appropriate eye movements that scale with modulation intensity. In some cases, eye movement responses were consistent with spurious stimulation of non-target canal nerve branches. For example, increasing stimulus current amplitude for electrode E6 in the horizontal canal of subjects MVI003 and MVI004 (Figure 2.7F,J) amplified the desired LHRH component but also elicited an increasingly prominent LARP component at larger current amplitudes, consistent with excitation of both the left horizontal and left anterior ampullary nerve branches. This is not surprising considering the close proximity of the anterior and horizontal ampullae (and their ampullary nerves) to each other and the location of electrode E6. In both of these subjects, setting the current for E6 channel stimulation required navigating a trade-off, as higher currents were more effective at exciting LH responses but also caused more spurious LA stimulation.

While work from other groups has provided some insight into acute responses to vestibular prosthetic electrical stimulation, those studies used 2D oculography to assay elicited eye movements (i.e., recorded only the yaw and pitch components of the evoked nystagmus, ignoring the roll component), limiting estimation of current spread to each canal ampullary nerve [41–52]. When activating a subject to a baseline electrical stimulus signal that can be modulated to encode head rotations, the neural response to the onset of tonic stimulation should elicit global excitation of all three canals in the implanted labyrinth. In this situation the evoked eye movement should be dominated by yaw and roll, because pitch components driven by anterior and posterior canal stimulation cancel each other (assuming relatively equal activation of each canal) while the torsional components add constructively.

Studies investigating vestibular compensation in human subjects report that adaptation of yaw and pitch VOR components adapt faster and more completely compared to roll components [67–70]. One reason may be that roll nystagmus would cause retinal slip error signals that are less effective at driving central vestibular adaptation than are signals due to yaw or pitch slip, because torsion of the eyes about the line of sight does not result in the fovea moving away from the point of fixation.

Our data indicate that all 3D components of the slow phase VOR response to tonic prosthetic vestibular stimulation decayed to <5°/s within 35 min for every subject (Figs. 4 and S3), with yaw and pitch decaying much faster than roll. These data support the hypothesis that retinal slip error caused by roll nystagmus does not drive compensatory VOR adaptation as effectively as retinal slip due to horizontal and vertical nystagmus components, perhaps because the former need not displace a fixation target from the retinal foveae while the latter do [67–70]. They are also consistent with previously reported data acquired using 2D video-oculography [41–52].

In subjects MVI003 and MVI004, onset of prosthetic stimulation evoked a ~-3°/s yaw nystagmus component that reversed direction during the first minute of measurement in darkness (Figure 2.11B and C, respectively). This may represent a nystagmus reversal analogous to that observed for normal subjects during prolonged, constant velocity whole-body rotation [71–75].

All subjects reported briefly intense vertigo for less than 5 minutes immediately upon onset of stimulation, and all described the head motion percepts as predominantly a mix of yaw and roll head movement, consistent with the expected vector sum of roughly equal components about the axes of the three implanted/excited canals. The perceived combined yaw and roll head motion faded rapidly and ended by <10 min after onset of stimulation. Starting ~30 min after stimulation onset, each subject was able to walk around the clinic, initially assisted but then completely independently by <60 min after stimulation onset. Each subject was discharged from the outpatient clinic on the activation day without the need for additional assistance or overnight observation.

Chapter 3 Longitudinal 3D Binocular Eye Movements During Continuous 3D MVI Stimulation

3.1 Introduction

In contrast to the systems used to deliver stimulation in a laboratory setting in prior studies investigating prosthetic electrical stimulation of vestibular afferents in humans [41–52], the MVI™ Multichannel Vestibular Implant System developed by Labyrinth Devices LLC and MED-EL GmbH is intended to continuously treat individuals suffering from severe/profound loss of semicircular canal function 24 hours/day over a lifetime of use. The MVI™ constantly senses and encodes 3D head rotational velocity via pulse-amplitude- and/or pulse-rate-modulation of biphasic, charge balanced current pulses delivered to each canal to encode head rotations.

In this chapter, we report responses seen during 8 weeks of continuous motion-modulated use of the system in four human subjects. We describe eeVOR responses to modulation of adapted prosthetic input targeting each of three canals individually, simultaneous stimulation of multiple canal nerve branches intended to encode different 3D axes of head rotation, and to whole-body rotations during motion-modulated and constant-rate/-current electrical stimulation.

3.2 Methods

The study design, recruited subjects, surgical procedure, the Labyrinth Devices MVI™ system, 3D eye movement recording system, and data analysis methods were described in Chapter 2.

3.2.1 Stimulus encoding using the MVI™ system

The MVI™ system uses pulse-rate- and pulse-amplitude-modulation (Figure 3.1) of charge-balanced, biphasic current pulses to encode head rotations. The system is designed to encode head velocity waveforms generated via measurements acquired by the motion sensor within the subject's HWU during head rotations or produced by a galvanically isolated computer during experimental testing sessions to encode a *virtual* head rotation when the head is, in fact, stationary. For example, to encode a 1Hz, 100°/s peak velocity sinusoidal head velocity waveform (Figure 3.1A), the signal is first processed by a canal-specific mapping programmed into the subject's PCU. This mapping defines pulse rate (Figure 3.1B, top) and current amplitude (Figure 3.1B, bottom) of charge-balanced biphasic cathodic-first pulses delivered via a given canal channel as a function of the component of head velocity amplitude about that canal's axis of rotation. The resulting modulation waveforms (Figure 3.1C) illustrate the time-varying changes in pulse rate (Figure 3.1C, top) and current amplitude (Figure 3.1C, bottom) defining the output pulsatile waveform (Figure 3.1D). When the system is running in its usual motion-modulated mode but the head velocity reported by the HWU is zero, the implanted stimulator delivers a constant, non-zero rate and current baseline stimulus to mimic the spontaneous activity typical of a normal canal's primary afferent neurons when the head is not moving.

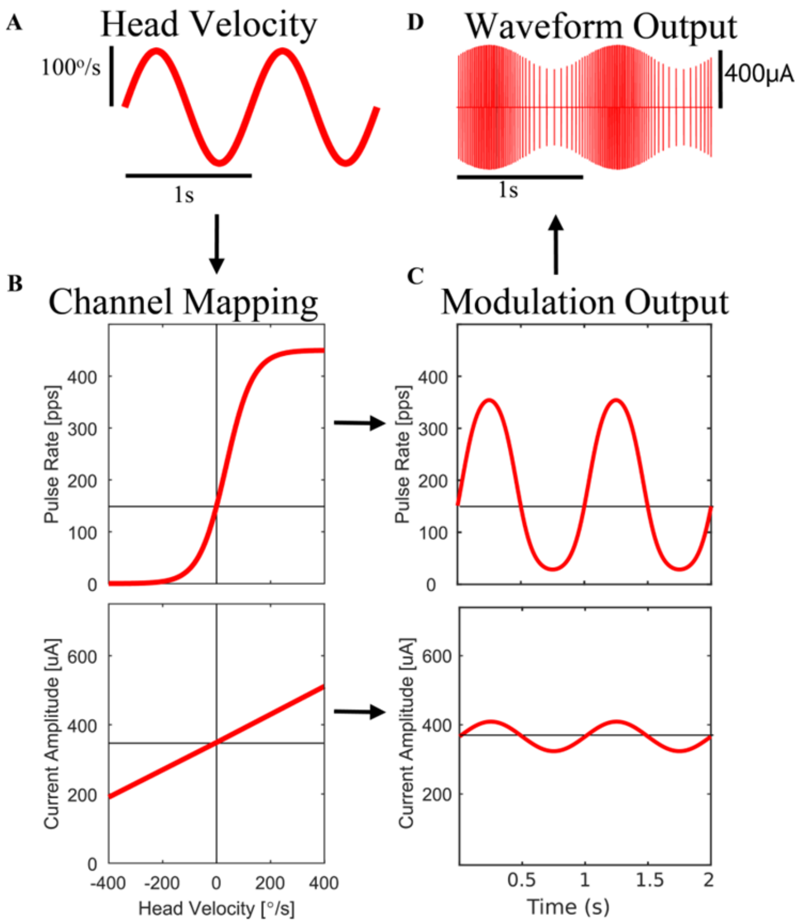

Figure 3.1. MVI™ pulse-rate- and pulse-amplitude-modulation encoding scheme. (**A**) Example head velocity waveform used to modulate the electrical stimulation delivered by the MVI™ system. This signal can be generated either via mechanical head motion sensed by the MPU or generated by the fitting software to create a *virtual* head velocity stimulus to directly assay the effect of electrical stimulation on evoked eye movements without contributions from residual function or non-vestibular cues. (**B**) MVI002's final pulse rate- and pulse amplitude- modulation mappings for the horizontal canal electrode (E6) using 100µs/phase current pulses. The upper plot portrays the head velocity-to-pulse rate mapping that defines the pulse rate used to encode head velocities, while the lower plot shows the mapping used to modulate pulse amplitude as a function of head velocity. The pulse frequency and current amplitude maps use a non-zero pulse rate (150 pulses per second, pps) and non-zero current amplitude value (349µA) to represent when the subject's head is stationary (0°/s), respectively. This allows the system to encode excitatory and inhibitory head motions through up- and down-modulation of these baseline values. (**C**) The resultant time series trace showing the instantaneous pulse rate and current amplitude used by the MVI™ to encode the head velocity waveform shown in (A). (**D**) The output pulsatile waveform delivered to a MVI™ electrode contact to encode the head velocity trace.

Head rotational velocities reported by the HWU's 3-axis gyroscopic sensors modulate pulse rate, pulse amplitude, or both above and below this baseline rate and current amplitude. Acclimating a unilaterally-implanted subject to a non-zero tonic stimulation representing absence of head motion allows the MVI™ to encode not only excitatory, ipsiversive head rotations toward the implanted ear (which increase stimulus rate and/or current) but also inhibitory, contraversive head rotations, which down-modulate stimulation to encode head rotations as would the normal labyrinth's canal in a person with unilateral vestibular hypofunction.

The MVI™ encodes 3D head velocity via modulation of pulse rate and/or pulse amplitude of the adapted electrical stimulus delivered to each active canal electrode. For each active contact within a canal ampulla, a head velocity-to-pulse rate and head velocity-to-pulse amplitude mapping was programmed into the subject's PCU to update pulsatile stimulation parameters and encode 3D head rotation components about each anatomic canal axis. Mappings were programmed as either:

1) Flat

   Where pulse rate or amplitude is set to a single value that does not change with head velocity.

2) Piecewise-Linear

   A two-segment, piecewise-linear map constructed by mapping the head velocity input range from [-400°/s, 0°/s, +400°/s] to the minimum, baseline, and maximum pulse rate or amplitude determined during electrode characterization.

3) Sigmoidal

   A non-linear mapping created using a hyperbolic tangent function to mimic the response dynamics of primary vestibular afferents in non-human primates [35,36,76] defined by:

$$Pulse(t) \ = \ 0.5 * (P_{MAX} - P_{MIN}) * \left(1 + tanh\left(X + C_{RATE} * \left(\frac{v(t)}{v_{MAX}}\right)\right)\right) + P_{MIN}$$

and

$$X = atanh(2 * \frac{P_{BASELINE} - P_{MIN}}{P_{MAX} - P_{MIN}} - 1)$$

Where:

$Pulse(t)$ ≜ Mapping describing either pulse-amplitude- or pulse-rate-modulation of prosthetic stimulation as a function of head velocity.

$v(t)$ ≜ Input head velocity waveform. This can be generated either via measurements made using the 3-axis gyroscope sensors in the subject’s HWU or generated by a galvanically isolated computer with the subject’s head stationary.

v_{MAX} ≜ Maximum input head velocity magnitude. Set to 400°/s for all subjects. The head velocity input range is set to $[-v_{MAX}, v_{MAX}]$

$P_{BASELINE}$ ≜ Pulse rate or amplitude used when the subject's head is stationary (i.e., 0°/s)

P_{MAX} ≜ Maximum pulse rate or amplitude used to encode the maximum input head velocity (v_{MAX}).

P_{MIN} ≜ Minimum pulse rate or amplitude used to encode the minimum input head velocity ($-v_{MAX}$).

C_{factor} ≜ Compression factor defining the slope of the head velocity-to-pulse rate or -pulse amplitude curve.

The mapping parameters used for each subject in this chapter are outlined in Table 3.1 and Figure 3.2.

Implant Ear	Left	**Subject ID**	**MVI001**	**MVI002**	**MVI003**	**MVI004**
		Date of Testing	11/02/2016	1/24/2017	04/18/2017	02/27/2018
		Days Since MVI™ Activation	56	55	54	53
RALP		Electrode ID	E3	E3	E3	E3
		Phase Dur. [us/phase]	200	100	200	200
	Amp. Mod.	Map Type	Flat	Piecewise Linear	Flat	Piecewise Linear
		Min. Pulse Amp. [uA]	N/A	500	N/A	125
		Baseline Pulse Amp. [uA]	450	600	600	406
		Max Pulse Amp. [uA]	N/A	700	N/A	500
		Compression Factor	N/A	N/A	N/A	N/A
	Rate Mod.	Map Type	Sigmoidal	Sigmoidal	Sigmoidal	Sigmoidal
		Min. PR [pps]	0	0	0	0
		Baseline PR [pps]	100	150	150	150
		Max PR [pps]	400	450	450	450
		Compression Factor	2	5	2	5
LHRH		Electrode ID	E7	E6	E6	E6
		Phase Dur. [us/phase]	200	100	200	200
	Amp. Mod.	Map Type	Flat	Piecewise Linear	Sigmoidal	Sigmoidal
		Min. Pulse Amp. [uA]	N/A	150	610	220
		Baseline Pulse Amp. [uA]	600	350	620	320
		Max Pulse Amp. [uA]	N/A	550	700	470
		Compression Factor	N/A	N/A	20	3
	Rate Mod.	Map Type	Sigmoidal	Sigmoidal	Sigmoidal	Sigmoidal
		Min. PR [pps]	0	0	0	0
		Baseline PR [pps]	100	150	150	150
		Max PR [pps]	400	450	450	450
		Compression Factor	2	5	2	5
LARP		Electrode ID	E11	E9	E9	E11
		Phase Dur. [us/phase]	200	100	100	200
	Amp. Mod.	Map Type	Flat	Piecewise Linear	Sigmoidal	Piecewise Linear
		Min. Pulse Amp. [uA]	N/A	500	400	220
		Baseline Pulse Amp. [uA]	700	600	400	550
		Max Pulse Amp. [uA]	N/A	700	420	600
		Compression Factor	N/A	N/A	20	N/A
	Rate Mod.	Map Type	Sigmoidal	Sigmoidal	Sigmoidal	Sigmoidal
		Min. PR [pps]	0	0	0	0
		Baseline PR [pps]	100	150	150	150
		Max PR [pps]	400	450	450	450
		Compression Factor	2	5	2	5

Table 3.1. MVI™ stimulation parameters for each subject during testing after 8-weeks of continuous, motion-modulated electrical stimulation. Current pulse and dynamic mapping parameters used in this chapter.

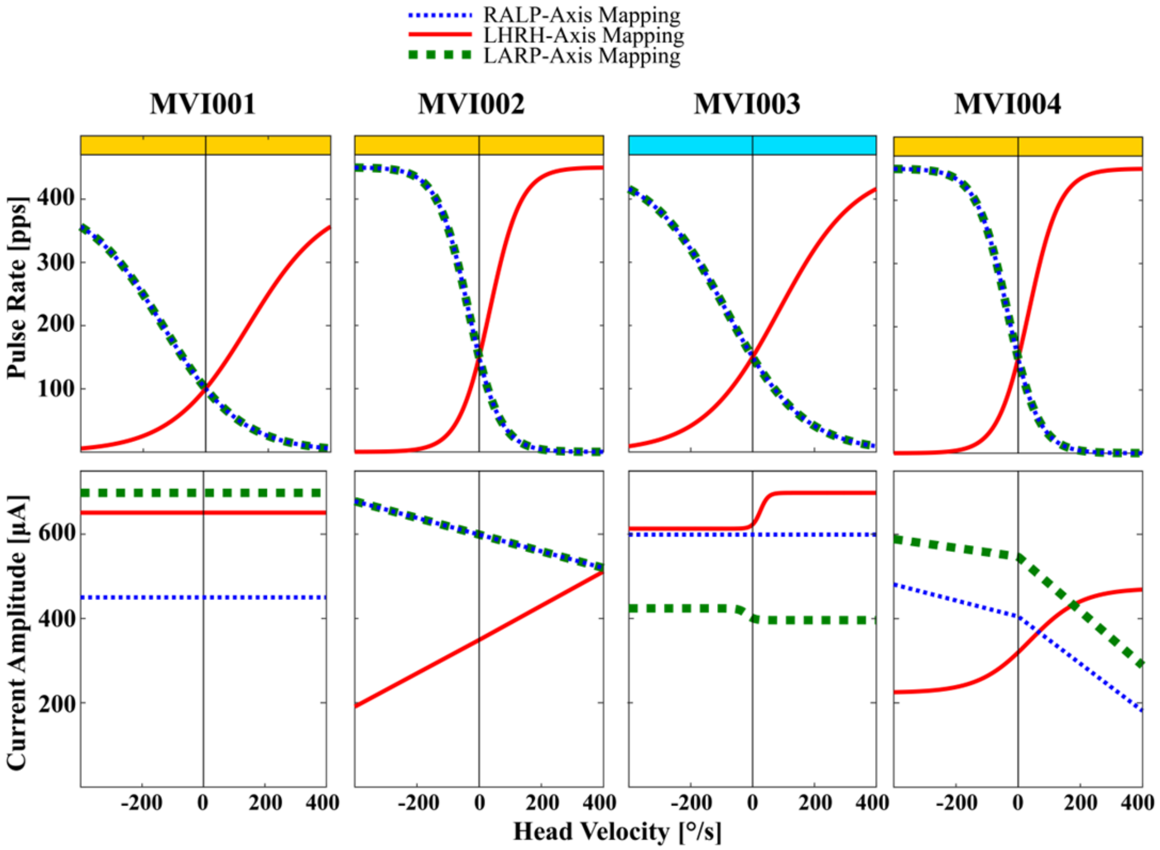

Figure 3.2 Graphical representations of all subject mappings after 8-weeks of continuous, motion-modulated electrical stimulation. Head velocity-to-pulse rate and -pulse-amplitude mappings programmed into each subject's PCU during testing after 8 weeks of motion-modulated electrical stimulation. Throughout the period of continuous stimulation, parameters were adjusted to optimize subject performance for each canal electrode individually. Colored bars at the top of each column correspond to the colored labels used in Figure 6.1 and Table 6.1 describing longitudinal mapping changes.

3.2.2 Virtual head velocity stimulation

For experiments using virtual head velocity waveforms, the PCU was programmed to bypass gyroscopic input from the HWU and provide 'virtual' head motion signals processed by the subject's PCU. The device communicated with the implanted stimulator to provide a sequence of pulsatile stimuli encoding head rotations according to each canal's stimulation parameters describing relationships between head velocity and both pulse rate and pulse amplitude for each active electrode (Table 3.1 and Figure 3.2). These stimuli were delivered with the subject in darkness and their head stationary on a custom bite-block to prevent visual, latent vestibular, or cervico-ocular reflex responses from influencing recorded eye movements.

3.2.3 Rotary chair testing

An Earth-vertical rotary chair (NeuroKinetics, Inc., Pittsburgh, PA) was used to provide whole body, *en bloc* sinusoidal rotations in darkness using frequencies between 0.1–2Hz at 100°/s peak velocity. Rotatory testing was performed both pre-operatively and post-operatively before any electrical stimulation to assay changes to mechanical vestibular function due to surgical procedures. After activation of the MVI™ system, testing was completed in the following two conditions: a) with the device set to provide pulsatile stimulation that modulated according to parameters programmed into the subject's PCU ("Modulation ON") and b) with the PCU set to provide non-modulating, constant-rate and -amplitude tonic stimulation on each active canal electrode ("Modulation OFF").

3.3 Results

3.3.1 Electrode impedance remained stable over 8 weeks of continuous use

To measure electrode impedances intraoperatively and repeatedly throughout 8 weeks of sustained pulse-rate- and pulse-amplitude-modulated electrical stimulation (Figure S4), we used MED-EL Maestro 6.0.1 clinical cochlear implant software and a MAX Programming Interface with 24µs/phase and 302 clinical unit amplitude pulses (where 1 clinical unit is ~1µA [77]). In most cases, electrode impedances remained constant throughout the continuous stimulation period. For subject MVI002 (Figure 3.3B), electrode E11 produced a high amplitude impedance value (consistent with a break in the electrode lead) around 21kΩ. Electrode E11 in subject MVI004 (Figure 3.3D) alternated between a 'high' state of around 15kΩ and a 'low' state of ~10kΩ.

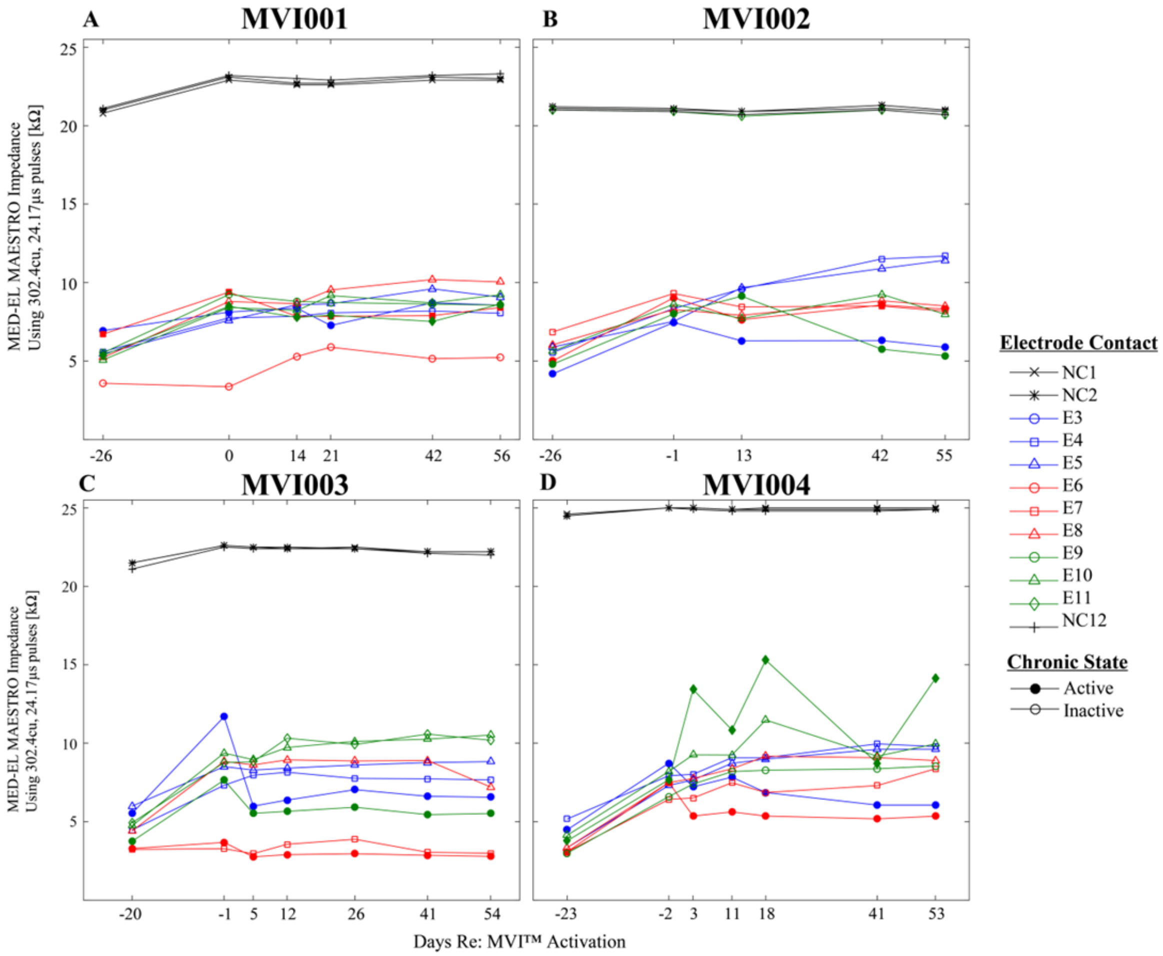

Figure 3.3. Electrical impedance measurements remain stable over 8 weeks. Throughout the 8 weeks of continuous motion-modulated stimulation, a clinical cochlear implant system (MED-EL Maestro 6.0.1 software and a MAX Programming Interface) recorded electrode impedance measurements for all electrode outputs of the stimulator. All data were collected using biphasic, charge balance current pulses using 200µs/phase and 302 clinical unit (cu) stimuli, where 1cu ≈ 1µA [77]. Data labeled as "NC" are "No Connect" outputs of the stimulator that are open circuit simulator channels not connected to any electrode contacts and shown for comparison. In each plot, the 'active' electrode within a canal electrode shank that was continuously used during the 8 week period is displayed with a filled in marker, while the unused electrodes are hollow. Overall subjects (**A**) MVI001, (**B**) MVI002, (**C**) MVI003, and (**D**) MVI004 produced electrical impedance values that remained relatively stable throughout the continuous stimulation period (i.e., "Days Re: Activation" > 0). For subject MVI002, electrode E11 produced a high amplitude impedance (~21kΩ) in line with the "No Connect" electrodes and consistent with an electrode lead breakage. For subject MVI004, electrode E11 varied between ~10kΩ and ~15kΩ.

3.3.2 Modulation of pulse rate and current amplitude encodes head angular velocity magnitude

After 8 weeks of continuous, 24 hour/day motion-modulated electrical stimulation, each subject was tested using sinusoidally modulated stimuli while the subject's head was held stationary on a bite-block in darkness to measure eye movements elicited by MVI™ stimulation without confounding contributions from residual vestibular function in the non-implanted ear, vision, potential responses from the cervico-ocular reflex during head-on-body rotations, or other cues not originating from primary vestibular afferent activity. Each canal's active electrode was modulated alone, while active electrodes in the other canals maintained constant pulsatile current and rate. Each virtual sinusoidal signal was modulated to represent peak head velocities from 20 to 400°/s, or from 5 to 100% of the mapping programmed into the subject's PCU (Table 4.1).

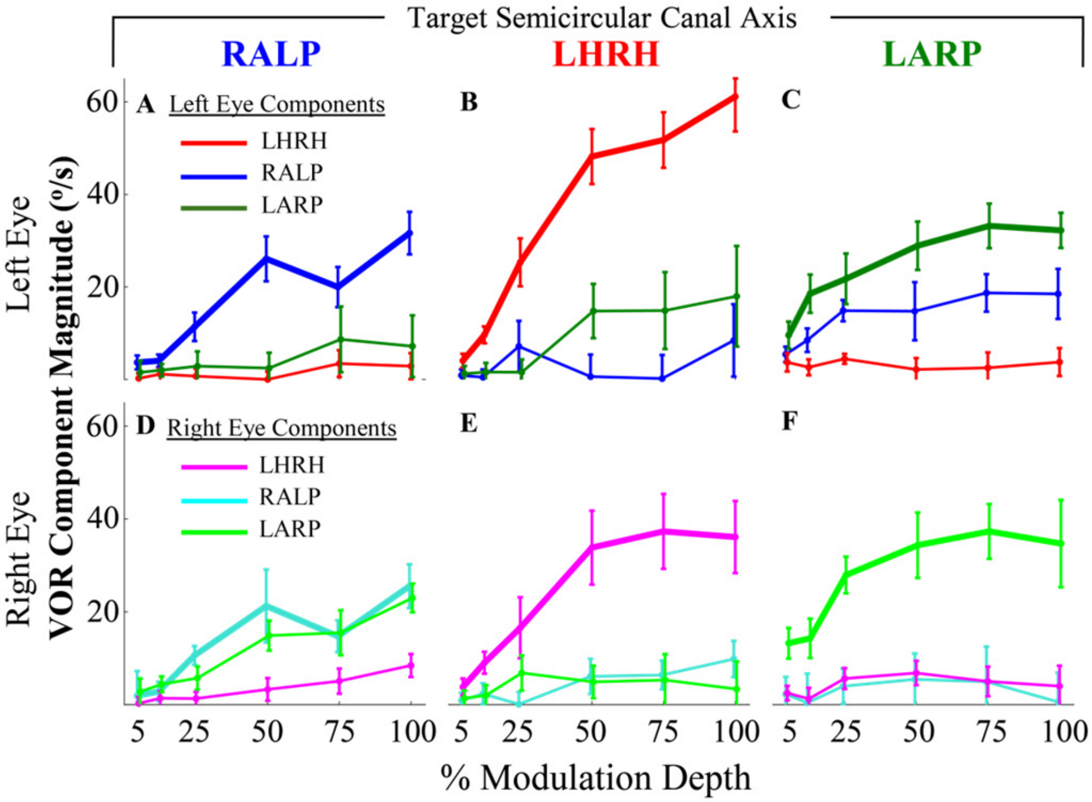

Figure 3.4. Sinusoidally modulated electrical stimulation targeting excitation of a single canal produces eye movements that align with that canal and grow with modulation depth. After 8 weeks of continuous motion-modulated prosthetic stimulation, the pulsatile electrical stimulus for each active electrode of subject MVI002 was modulated to encode a series of 2Hz sinusoidal head velocity waveforms to assay the full head velocity range for each SCC channel with the subject's head stationary. Sinusoidal head velocity amplitudes ranged between 5% and 100% of the full-scale range of input head velocity (where 100% is 400°/s). Table 3.1 and Figure 3.2 shows the stimulus parameters used for all subjects. 3D peak eye velocity magnitudes during the excitatory half-cycles are plotted for the (**A-C**) left and (**D-F**) right eyes as a function of modulation depth during experiments testing the active electrode in the (**A,D**) left posterior (E3), (**B,E**) left horizontal (E6), and (**C,F**) left anterior (E9) canals. Each electrode was individually modulated while the other two channels were held at a constant current amplitude and tonic pulse rate. Target canal VOR components are bolded in each panel.

Peak 3D eye velocity magnitudes evoked in both the left (Figure 3.4A-C) and right (Figure 3.4D-F) eye of subject MVI002 grew with modulation depth. Stimuli delivered to the active electrode in the left posterior (E3, Figure 3.4A,D), left horizontal (E6, Figure 3.4B,E), and left anterior (E9, Figure 3.4C,F) canals produced eye movements predominantly in the plane of the intended canal. An exception to this observation is in the left eye during stimulation targeting the left anterior canal (Figure 3.4C) and the right eye when encoding a left posterior head velocity (Figure 3.4D). In these cases, the response is less selective and produces eye movements approaching a pure vertical eye velocity. Similar results were observed with subjects MVI001 (Figure 3.5A), MVI003 (Figure 3.5B), and MVI004 (Figure 3.5C). Subject MVI001 produced a similar disconjugacy between the left and right eye seen in subject MVI002 for LARP and RALP stimulation (Figure 3.5A bottom left and top right), while the remaining ocular responses were well aligned. Subject MVI003 (Figure 3.5B) produced eye movements that, although dominated by the target SCC components, were smaller in amplitude (peak responses ~20°/s for 100% stimulus modulation depth). Subject MVI004 (Figure 3.5C) produced selective RALP responses when stimulating the left posterior canal (Figure 3.5C left), a coupled LHRH and LARP response when modulating the electrode in the left horizontal canal (Figure 3.5C middle), and a modest but well aligned LARP eye movement in response to patterned electrical stimulation delivered to the left anterior canal.

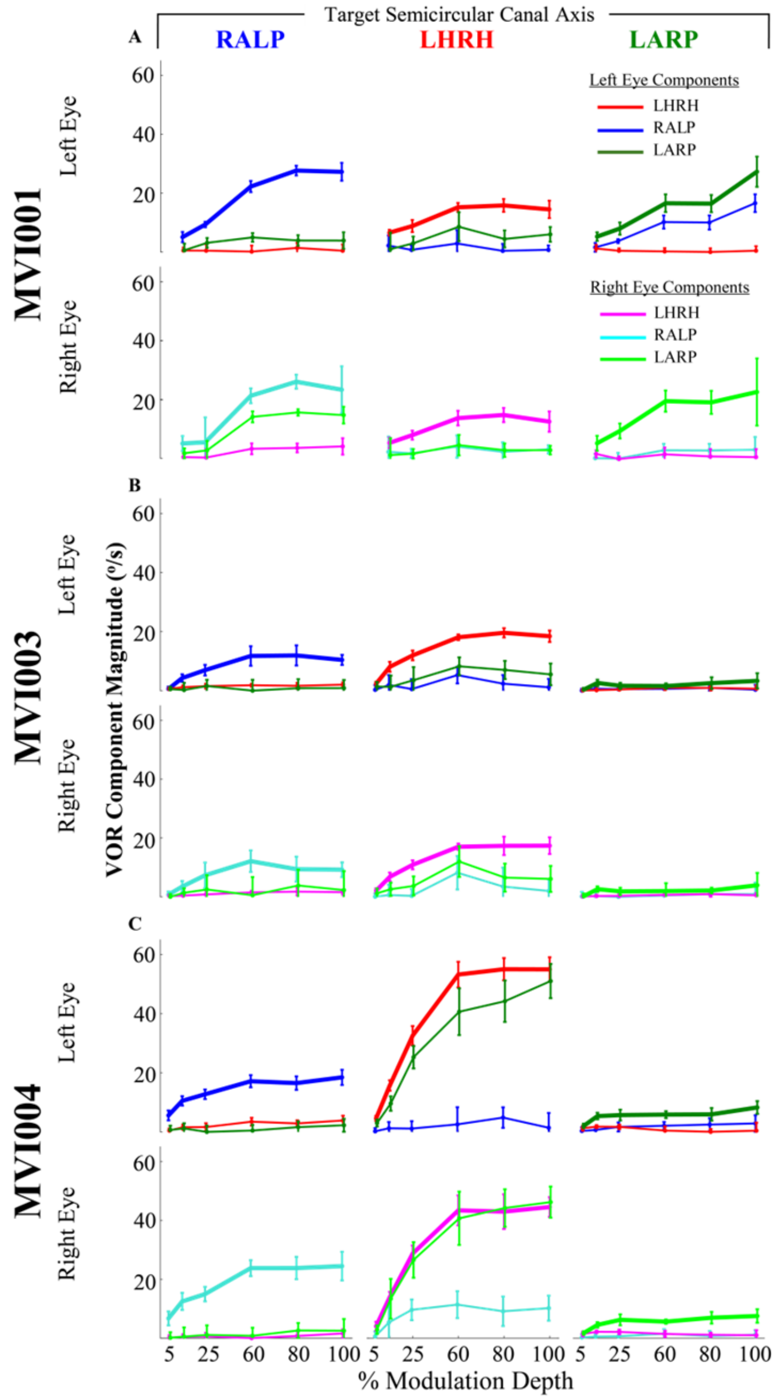

Figure 3.5. Eye movement responses to excitatory half-cycles of pulsatile waveforms encoding 2Hz sinusoidal head motion (MVI001, MVI003, and MVI004). Excitatory half-cycles of virtual head velocity waveforms encoding 2Hz sinusoids targeting the active electrodes in each canal assayed each electrode's ability to drive canal-specific VOR responses after 8 weeks of continuous motion-modulated prosthetic stimulation. All data was collected with the subject's head stationary on a bite-block and the test environment darkened by occluding the subject's vision with visible-light blocking filters and turning off the experimental room lights. Target canal components are bolded in each figure. (**A**) Subject MVI001 produced stable VOR responses that grew in magnitude with modulation intensity. VOR responses tended to rotate about an axis that closely approximated the target anatomic canal axis, except during RALP stimulation in the right eye and LARP stimulation in the left eye. (**B**) Testing subject MVI003 with virtual head velocity sinusoids produced eye movements resembling the intended canal axes of rotation, though with lower amplitude peak eye velocities compared to subject's MVI001 and MVI002. Modulation of the current stimulus on electrode E9 in the left anterior canal (**B, right**) produced small amplitude eye movements when tested at 100% modulation depth (Left eye: 3.4±2.6°/s, Right eye: 4.0±4.2°/s). (**C**) Subject MVI004 produced 3D responses that approximated the intended anatomic canal axis of rotation during modulation of the electrical stimulus delivered to electrodes E3 in the left posterior canal (**C, left**) and E11 in the left anterior canal (**C, right**). During modulation of electrode E6 in the left horizontal canal (**C, middle**), the intended 3D component aligned with the subject's LHRH axis (red trace in top and pink trace in bottom) grew with modulation depth with an unintended LARP component (dark green on top and light green on bottom) that was likely due to co-activation of the left anterior nerve branch.

Responses to virtual 2Hz sinusoidal head velocity modulations were assayed throughout the 8 week period described above and intermittently throughout study enrollment. Throughout this period individual stimulation parameters for each canal channel were adjusted to optimize evoked responses amplitude and alignment (listed in Table 6.1 and shown graphically in Figure 6.5 - Figure 6.8). Subject MVI001 (Figure 3.6) was tested starting 42 days after device activation using stimuli ranging from 12.5-100% modulation depth (visits occurring after 132 days post-activation tested the entire 5-100% modulation depth range). Preceding the 42 day visit, eye movement responses were too small to accurately estimate response amplitude and required electrical stimulation parameter adjustments. From the data available, responses to stimulation of electrodes in the left posterior canals (E3, Figure 3.6 top) and left anterior (E11, Figure 3.6 bottom) canals remained stable out to 308 days post-activation. Responses to electrode E7 (Figure 3.6 middle) in the left horizontal canal decreased across all modulation depths by 306 days post-activation.

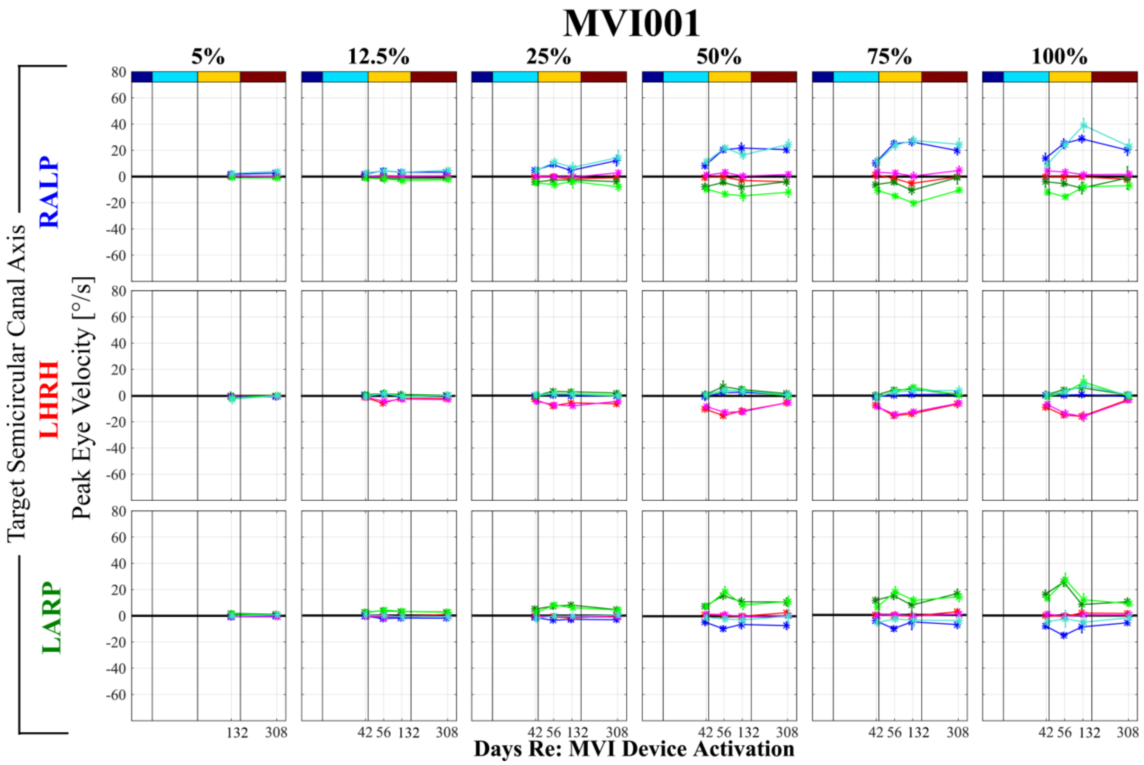

Figure 3.6. MVI001 longitudinal responses to virtual 2Hz sinusoidal modulations. Summary of responses from subject MVI001 up to 308 days after device activation when assayed using virtual head velocity waveforms to modualte pulsatile stimulation rates. All stimuli are 2Hz sinusoidal waveforms that span the input head velocity range (±20-400°/s) presented as a modulation depth (5-100%) delivered with the subject's head held stationary. This subject was not tested with these stimuli until day 42 post-activation (and day 132 for the 5% modualtion depth stimulus). Stimulus parameters used to encode head velocity were changed to optimize performance for each canal individually. The history of parameter changes are represented in Table 6.1 and graphically in Figure 6.5. Timepoints where received continuous, motion-mdulated stimulation are outlined at the top with colored bars indicating the distinct mapping used by this subject.

Subject MVI002 produced robust eeVOR responses that remained stable through 280 days of continuous, motion-modulated stimulation (Figure 3.7). Responses to modulation in all three canals produced eye movements rotating about 3D axes that closely approimate the target canal anatomic axis. Additionally, the disconjugacy seen when stimulating electrode E3 in the left posterior canal (Figure 3.7 top) and electrode E9 in the left anterior canal (Figure 3.7 top) remained when assayed 280 days post-activation and with no further changes to stimulation parameters following the onset of Mapping #3 (yellow color bar at the top of Figure 3.7) on day 41. Mapping #3 added amplitude modulation to all three canal channels, where excitatory head rotations would increase the amplitude of biphasic current pulses delivered to the active electrode in each canal. For this subject when stimulating electrode E6 in the left horizontal canal (Figure 3.7 middle), a minor unintended LARP component grew following onset of Mapping #3 (41 days post-activation).

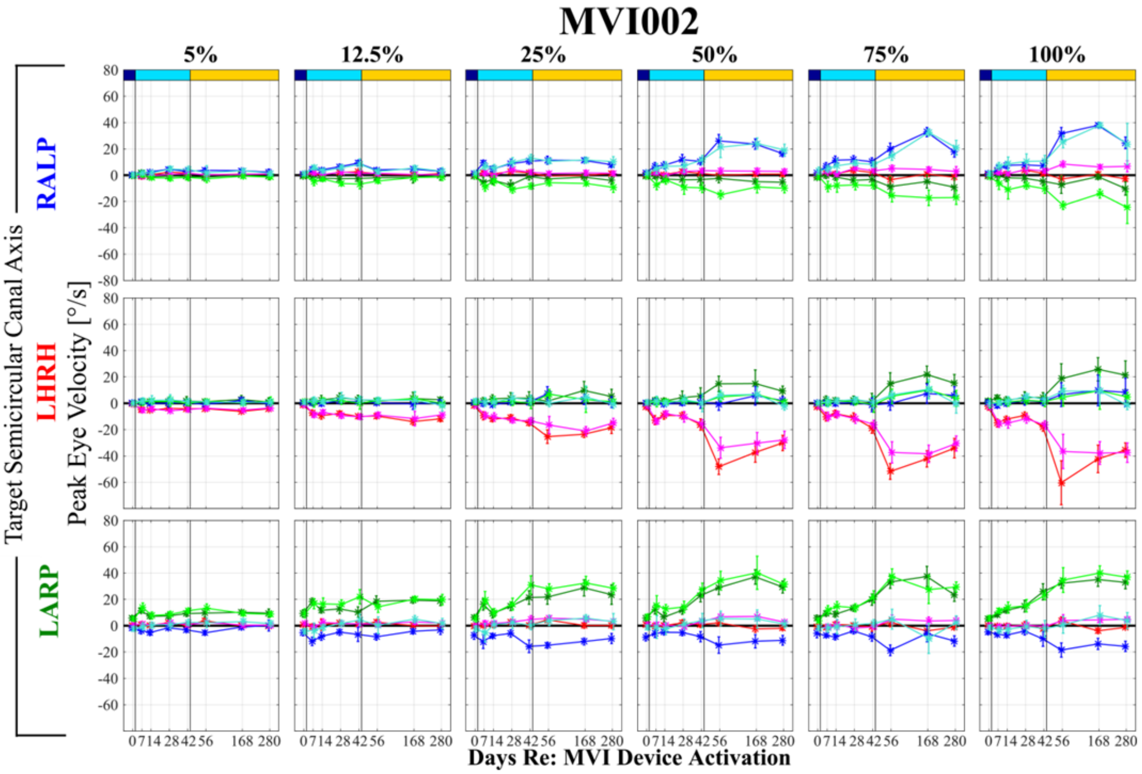

Figure 3.7. MVI002 longitudinal responses to virtual 2Hz sinusoidal modulations. Summary of responses from subject MVI002 up to 280 days after device activation when assayed using virtual head velocity waveforms to modualte pulsatile stimulation rates. All stimuli are 2Hz sinusoidal waveforms that span the input head velocity range (±20-400°/s) presented as a modulation depth (5-100%) delivered with the subject's head held stationary. Stimulus parameters used to encode head velocity were changed to optimize performance for each canal individually. The history of parameter changes are represented in Table 6.1 and graphically in Figure 6.6. Timepoints where received continuous, motion-mdulated stimulation are outlined at the top with colored bars indicating the distinct mapping used by this subject.

For subject MVI003, responses to electrodes E3 in the left posterior canal (Figure 3.8 top) remained consistent throughout the entire period presented, with a peak excitatory slow phase response of ~15°/s. The stimulation parameters for the E3 electrode remained unchanged throughout this period, meaning this stable response respresents a consistent activation of the poserior canal afferent branch. Electrode E9 in the left anterior canal (Figure 3.9 bottom) produced small responses that did not grow with the addition of pulse amplitude modulation (light blue bar at top of Figure 3.9, parameters listed in Table 6.1). Alternatively, the introduction of amplitude modulation for electrode E6 in the left horizontal canal after 13 days of continuous stimulation produced a consistent enchancement of the eeVOR response through the data reported 160 days after activation.

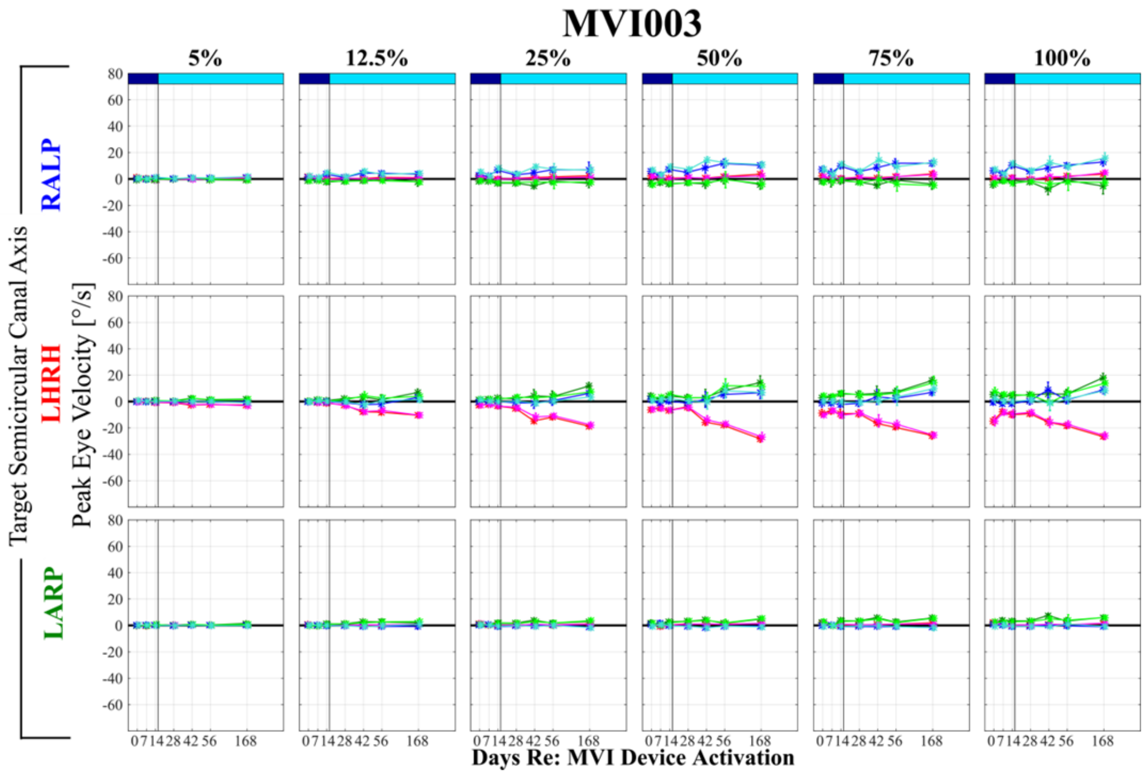

Figure 3.8. MVI003 longitudinal responses to virtual 2Hz sinusoidal modulations. Summary of responses from subject MVI003 up to 168 days after device activation when assayed using virtual head velocity waveforms to modualte pulsatile stimulation rates. All stimuli are 2Hz sinusoidal waveforms that span the input head velocity range (±20-400°/s) presented as a modulation depth (5-100%) delivered with the subject's head held stationary. Stimulus parameters used to encode head velocity were changed to optimize performance for each canal individually. The history of parameter changes are represented in Table 6.1 and graphically in Figure 6.7. Timepoints where received continuous, motion-mdulated stimulation are outlined at the top with colored bars indicating the distinct mapping used by this subject.

Different from the previous three subjects, MVI004 was activated with both pulse-rate-modulation and pulse-amplitude-modulation mappings to encode head rotations. Decrements to the compression factor/max current amplitude of the amplitude modulation mapping for the horizontal channel were the only parameter adjustments made during the 140 day post-activation period (Table 6.1). These changes were made at request of the subject, who reported an "energy" when turning her head to the left (i.e., an excitatory yaw axis rotation).

Responses to modulation of electrical stimulation for electrode E3 in the left posterior canal produced stable, consistent eeVOR responses over the 140 day period. (Figure 3.9 top). Modulation of electrode E6 in the left horisontal canal produced both a targeted LHRH VOR component in addition to a unintended LARP component consistent with co-activation of the left anterior canal. This trend was seen both immediately post-activation (day 0) with peak LHRH and LARP components of ~20°/s (Mapping #1 with a dark blue header in Figure 3.9) and after decreasing the horizontal channel amplitude modulation compression factor from 20 to 4 (i.e., changing the head velocity-to-pulse rate mapping from one that abruptly increases or decreses current according to the polarity of head motion, to one that smoothly modulates pulse amplitude with head motion). At the onset of Mapping #2, response amplitudes approximately doubled to a peak of ~40°/s. Modulation of electrode E9 in the left anterior canal produced response amplitudes that fluctuated from visit-to-visit in the post-activation period, consistent with the changes in electrode impedance of this subjects electrode E9 discussed previously (Figure 3.3).

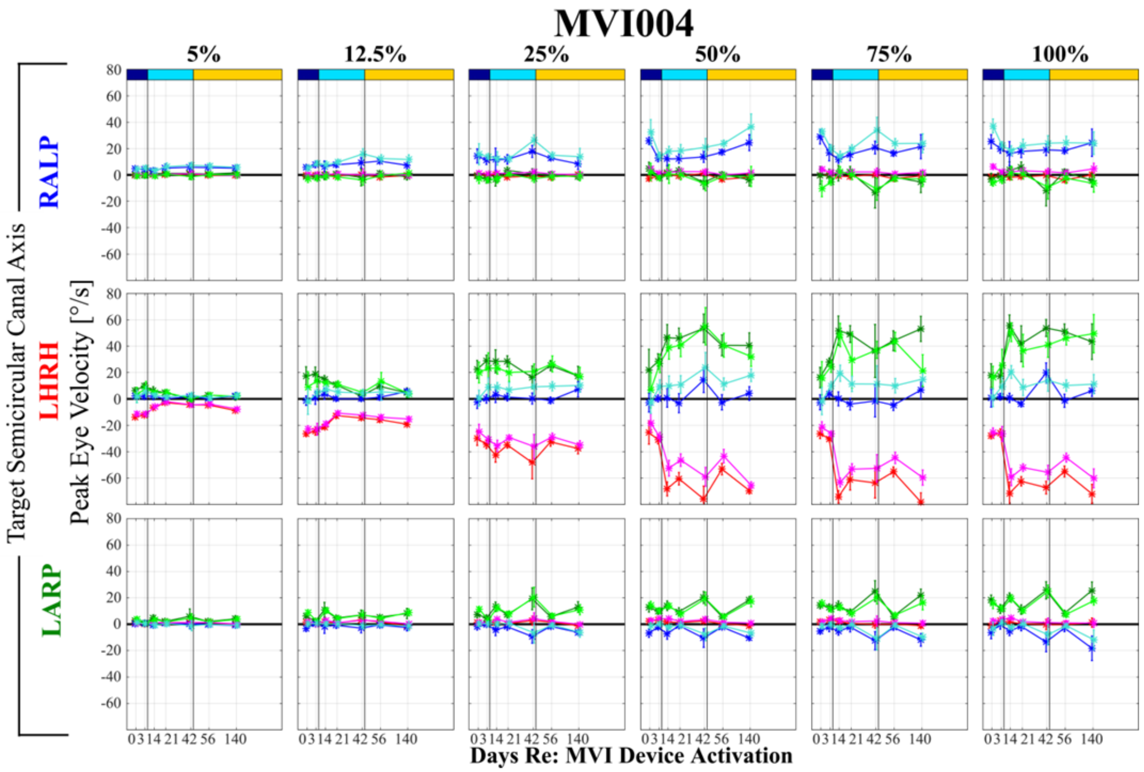

Figure 3.9. MVI004 longitudinal responses to virtual 2Hz sinusoidal modulations. Summary of responses from subject MVI004 up to 140 days after device activation when assayed using virtual head velocity waveforms to modualte pulsatile stimulation rates. All stimuli are 2Hz sinusoidal waveoforms that span the input head velocity range (±20-400°/s) presented as a modulation depth (5-100%) delivered with the subject's head held stationary. Stimulus parameters used to encode head velocity were changed to optimize performance for each canal individually. The history of parameter changes are represented in Table 6.1 and graphically in Figure 6.8. Timepoints where received continuous, motion-mdulated stimulation are outlined at the top with colored bars indicating the distinct mapping used by this subject.

3.3.3 Concurrent modulation of multiple electrodes encodes head rotations as a quasilinear 3D vector sum of canal-aligned components

A vestibular implant intended to restore 3D sensation should decompose and encode head rotation about any specified head rotation axis by eliciting proportionate activity on the three implanted canal's ampullary nerves, which the brainstem subsequently adds in a vector sense to compute an estimate of the head rotation axis [31,38]. We recorded 3D eye movements of head-fixed subjects in darkness during stimuli encoding ‘virtual’ head rotations about each canal rotation axis (using individual canal electrode contacts), the +X (‘Roll’) axis parallel to the subject’s naso-occipital axis, and the +Y (‘Pitch’) axis coincident with the subject’s inter-aural axis (Figure 3.10A) using brief virtual trapezoidally-modulated stimuli (50ms onset/offset ramp, 150ms plateau, and 250ms inter-trapezoid-interval) from 0 to 50% modulation depth.

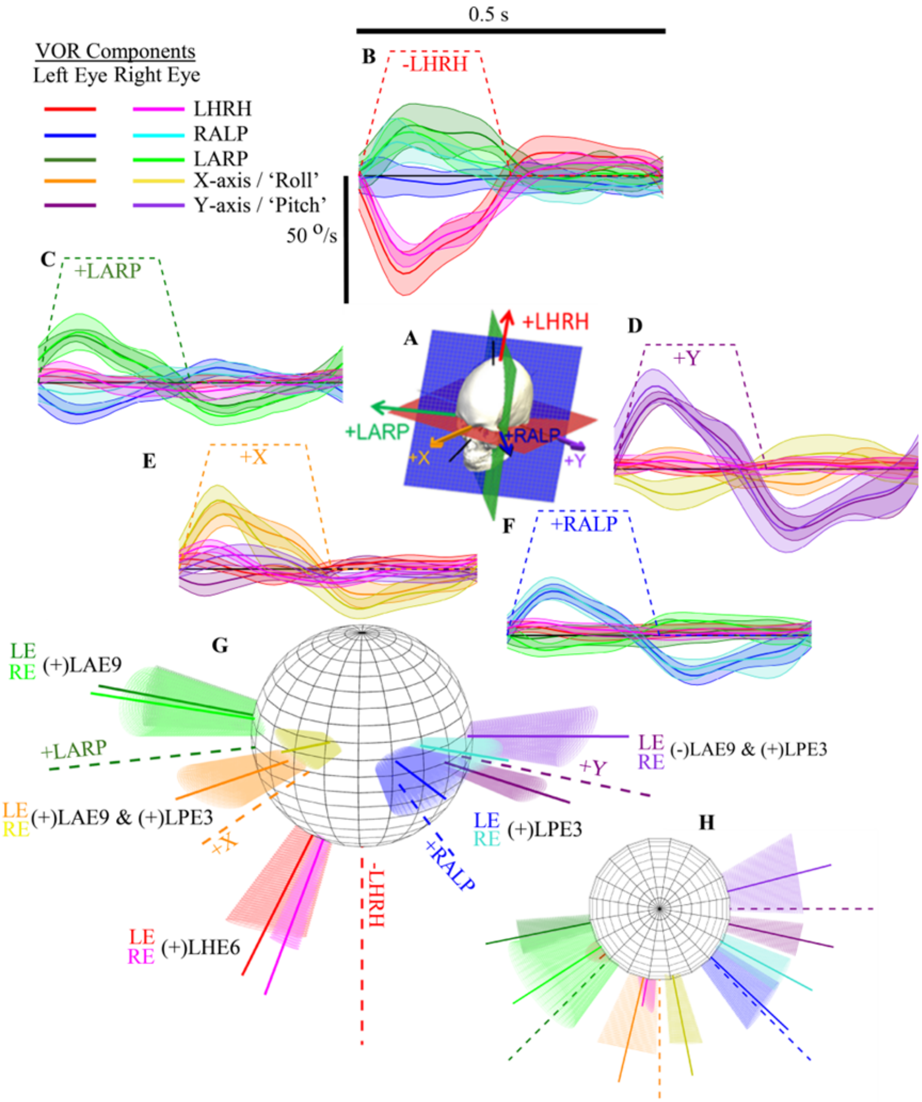

Figure 3.10. Simultaneous modulation of multiple canal electrodes encodes 3D head rotation axis. Selective stimulation of each canal afferent branch provides a basis set to encode arbitrary 3D vectors with the MVI. (**A**) Schematic view of the canal axes (+LARP, +RALP, +LHRH), the +X-axis along the subjects naso-occipital axis, and the +Y-axis along the subject's inter-aural axis. A 50% modulation depth trapezoidal velocity waveform sent to the (**B**) left horizontal (LHE6), (**C**) left anterior (LAE9), and (**F**) left posterior (LPE3) canals of MVI002 each evoked 3D eye velocities well aligned with their intended canal axes. (**E**) To encode an eye movement about the X-axis, electrodes LAE9 and LPE3 were modulated in phase (i.e., an excitatory stimulus was provided to both electrode contacts), producing a slow phase eye velocity aligned with the +X axis. (**D**) The LAE9 and LPE3 electrodes were modulated out of phase (where the LAE9 electrical stimulus decreased in pulse rate and current amplitude to encode an inhibitory LARP rotation, while the LPE3 electrical stimulus encoded an excitatory signal by increasing the pulse rate and current amplitude). This combination evoked a primarily vertical eye movement rotating about a vector closely aligned with the Y-axis. (**G**) Vectors showing the mean axis of rotation for each eye encoding all 5 vectors are plotted on a globe along with each target axis. Each mean eye velocity vector is plotted with a cone computed using the eigenvalues of the covariance matrix for each dataset to represent the uncertainty of the analyzed data. (**H**) The same data is presented looking down the top of the globe shown in (**G**).

Slow phase eye velocity responses to electrodes E6, E9, and E3 in subject MVI002 each evoked 3D eye velocities predominantly rotating about the target canal axis (Figure 3.10B,C and F, respectively). To encode a roll 'virtual' head movement (i.e., a slow phase eye velocity rotating about an axis approximating the +X axis in Figure 3.10A) a 50% modulation depth trapezoidal waveform was projected onto the canal coordinate system, producing concurrent excitatory modulation of E3 in the left posterior canal and E9 in the left anterior canal. Simultaneous excitation of those two canals should produce an eye movement consistent with the vector sum of responses to excitation of each canal's ampullary nerve alone. Excitation of the left anterior canal elicits an upward and clockwise eye movement (or a positive rotation about the +LARP axis in Figure 3.10A using the right-hand rule), while an increase in activity of the left posterior canal ampullary nerve elicits a downward and clockwise eye movement (or a positive rotation about the +RALP axis in Figure 3.10A). The opposite polarity vertical components mostly cancel each other, while the in-phase torsional components combine, producing a clockwise (positive) roll/torsional eye movement about the +X axis (Figure 3.10E).

In contrast, conveying a sensation of pitch head movements about the interaural +Y axis requires anti-phase modulation of stimuli delivered via electrodes E3 and E9. In that case, increasing pulse rate and current amplitude on E3 in the left posterior canal while simultaneously decreasing stimulus rate and pulse amplitude for E9 in the left anterior canal resulted in a downward pitch eye movement, which is positive by the right-hand-rule display convention used in Figure 3.10D. Plotting the binocular axes of rotation for all 5 stimuli (Figure 3.10G,H) demonstrates that stimulation of multiple canal electrode contacts can be combined to encode head rotations closely approximating predefined vector sums of multiple canal axes. Observations in all other subjects further corroborated the ability of MVI™ stimulation to encode 3 linearly independent, approximately canal-aligned components of 3D rotational motion, alone and in linear combinations (Figure 3.11).

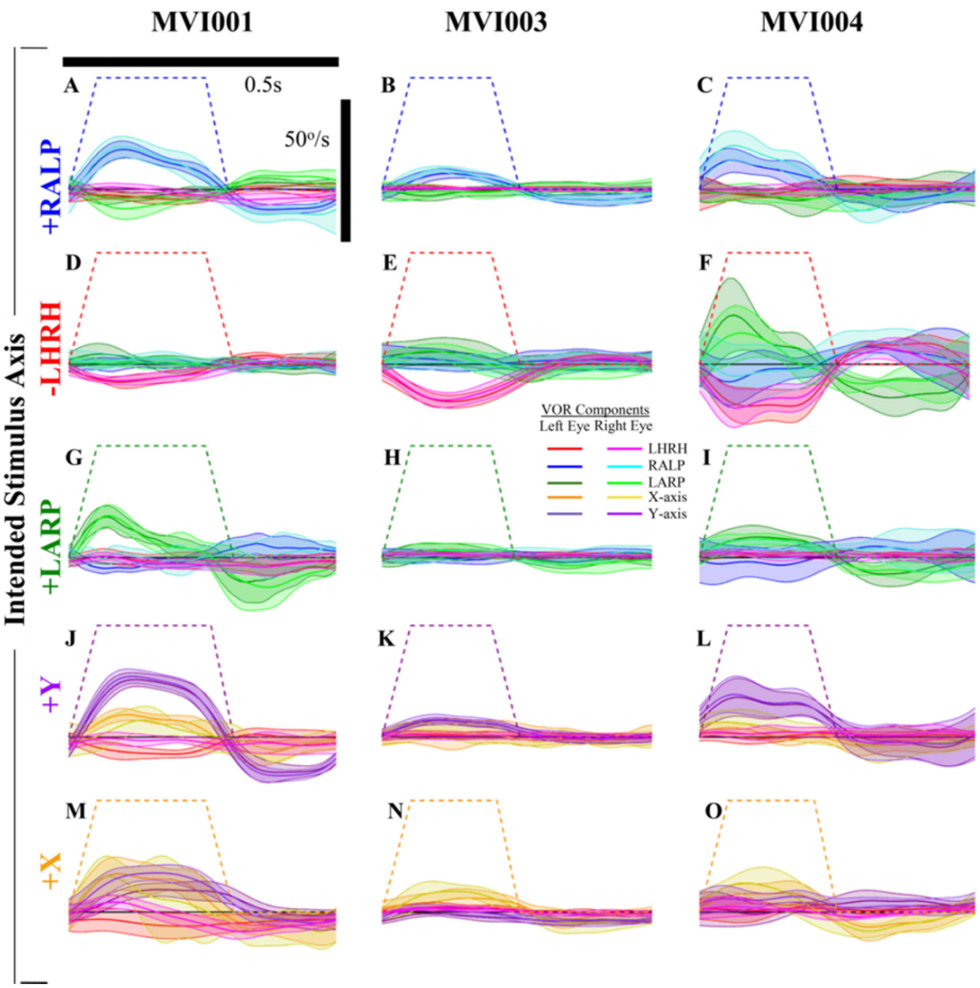

Figure 3.11. Responses to coordinated stimulation via multiple electrodes can approximately encode arbitrary head rotation axes (MVI001, MVI003, and MVI004). (**A,D,G,J,M**) For subject MVI001 combining modulation of electrodes E3 and E11 out of phase produced a predominantly vertical eye movement (**J**), while modulating E3 and E11 in-phase (**M**) evoked a binocular eye movement with comparable positive vertical and torsional eye velocities (which is a principally RALP eye movement when converted into anatomic canal coordinates). (**B,E,H,K,N**) MVI003 produced eye velocities well aligned with the intended head motion vectors, though with smaller eye velocities compared to the other subjects. (**C,F,I,L,O**) Subject MVI004 produced selective eye movements for all tested vectors, save for stimuli targeting the LHRH axis (**F**) where an unintended LARP component grew in amplitude with the targeted horizontal eye movement.

3.3.4 Pairing mechanical and electrical stimulation enhances low-frequency vestibulo-ocular reflex responses

To assay VOR performance during mechanical rotations with and without motion-modulated electrical stimulation, subjects were assayed during whole-body passive rotations in an Earth-vertical rotary chair. Each subject was tested with 100°/s whole-body sinusoidal rotations over five frequencies from 0.1-2Hz. The frequency sweep was performed during pre-operative testing, 3 weeks after implantation with the device inactive, and 8 weeks after activating the device to modulate electrical stimulation with head motion. To isolate the contribution of motion-modulated prosthetic stimulation with the device working in its usual mode ("Modulation ON" condition), chair-rotation tests were repeated with the device programmed to present only a tonic stimulus without varying the pulse amplitude or rate ("Modulation OFF" condition).

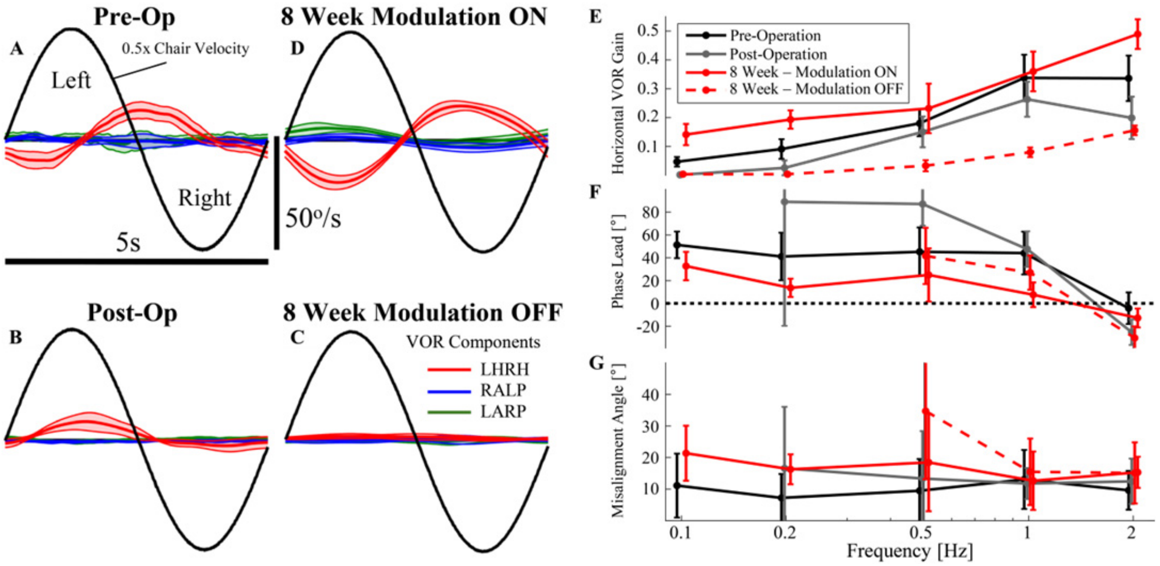

Figure 3.12. Prosthetic electrical stimulation enhances VOR responses to whole-body rotation in darkness. Subject MVI002 was tested using a 100°/s peak velocity sinusoidal frequency sweep (0.1-2 Hz) with an Earth-vertical-axis rotary chair. (**A-D**) Cycle averaged (mean±SD) eye velocity traces during 0.2Hz sinusoids with a head velocity trace shown at 0.5x scale during (**A**) pre-operative testing; (**B**) measurements 3 weeks post-operation; (**C**) trials conducted after 8 weeks of continuous use, with the device in its usual motion-modulated stimulation mode ("Modulation ON"); and (**D**) with the prosthesis delivering constant rate/constant current pulsatile stimulation ("Modulation OFF"). (**E**) Mean±SD VOR gain as a function of frequency for each condition. VOR gain was significantly different between the four conditions (ART two-way repeated measures ANOVA; $F_{[3,932]} = 606.7$, $p < 1e^{-4}$), and post hoc pairwise tests revealed that VOR gain during preoperative testing and during "Modulation ON" testing was significantly different for the 0.1, 0.2, 0.5, and 2Hz stimulus conditions (Wilcoxon rank sum tests: 0.1Hz, Z = 3.63, P < 0.001; 0.2Hz, Z = 4.05, P < 1e-4; 0.5Hz, Z = 2.22, P < 0.05; 2Hz, Z = 4.91, P < 1e-4). (**F**) Phase response during sinusoidal steady state of the cycle averaged response. A positive phase lead here denotes the VOR slow phase response leading the inverse of head velocity. Phase lead differed significantly for all four conditions (ART two-way repeated measures ANOVA; $F_{[3,829]} = 106.5$, $p < 1e^{-4}$) with pairwise post hoc comparisons revealing significant differences between preoperative testing results and data collected during the "Modulation ON" condition from 0.1-1Hz (Wilcoxon rank sum tests: 0.1Hz, Z = 2.82, P < 0.01; 0.2Hz, Z = 3.93, P < 1e-4; 0.5Hz, Z = 2.43, P < 0.05; 1Hz, Z = 4.36, P < 1e-4). (**G**) Misalignment angle as a function of sinusoidal frequency. The increase in misalignment between pre-operative testing and during the "Modulation ON" condition after 8 weeks of continuous stimulation was significant at 0.2, 0.5, and 2Hz (Wilcoxon rank sum tests: 0.2Hz, Z = 2.89, P < 0.01; 0.5Hz, Z = 2.87, P < 0.01; 2Hz, Z = 2.34, P < 0.05). VOR responses <1.5°/s were too small to permit accurate estimation of both phase and misalignment.

Pre-operative testing (Figure 3.12A) revealed subject MVI002's low VOR gain typical of bilateral hypofunction and a phase lead of the peak rightward eye velocity relative to the peak leftward head velocity at 0.2Hz (gain = 0.09±0.03, phase lead = 41.2±20.8°). After implantation, but before initial activation (Figure 3.12B), the subject displayed a reduced VOR response during rotation to the left (seen in the reduced negative phase of the sinusoidal response) and a ~90° phase lead of evoked eye velocity relative to the ideal ocular response. After 8 weeks of continuous motion-modulated stimulation (Figure 3.12C) the excitatory VOR gain grew to 0.19±0.03, and the phase lead at 0.2Hz reduced to 13.7±8.0°. In the "Modulation OFF" condition (Figure 3.12D), the VOR response at this frequency was near 0°/s, significantly lower than pre-op, post-op/pre-activation and the "Modulation ON" condition.

From 0.1-2Hz, the magnitude response (Figure 3.12E) demonstrated a high-pass frequency response across all conditions. The decrease in VOR magnitude from pre-operative (black trace) to post-implantation without electrical stimulation values (gray trace) is consistent with the expectation that implanting the electrode leads in each canal ampulla is likely to disrupt the cupula and therefore residual natural canal sensation. Data collected after 8 weeks of sustained electrical stimulation with the device programmed to provide electrical stimulation that modulated with head motion ("Modulation ON", solid red trace) show an enhancement at low frequencies (0.1-0.5Hz) and at 2Hz. An aligned rank transform (ART) with two-way repeated measures ANOVA confirmed a significant difference in gains for the main effect of MVI condition (pre-operative, post-operative but before any electrical stimulation, "Modulation OFF", and "Modulation ON"; $F_{[3,932]} = 606.7$, $p < 1e^{-4}$). Post hoc pairwise tests revealed that VOR gains for the "Modulation ON" condition were significantly greater than pre-op for 0.1, 0.2, 0.5 and 2Hz stimuli (Wilcoxon rank sum tests: 0.1Hz, $Z = 3.63$, $p < 0.001$; 0.2Hz, $Z = 4.05$, $p < 1e^{-4}$; 0.5Hz, $Z = 2.22$, $p < 0.05$; 2Hz, $Z = 4.91$, $p < 1e^{-4}$). The VOR response dropped below pre-operative values across all frequencies when the subject's device was in the "Modulation OFF" condition (dashed red trace). The phase response (Figure 3.12F) shows a reduction (i.e., improvement) in phase lead during "Modulation ON" trials across all frequencies. Changes in phase lead were significantly different for all four conditions (ART two-way repeated measures ANOVA; $F_{[3,829]} = 106.5$, $p < 1e^{-4}$) with pairwise post hoc comparisons revealing significant differences between the "Modulation ON" and pre-operative testing from 0.1-1Hz (Wilcoxon rank sum tests: 0.1Hz, $Z = 2.82$, $p < 0.01$; 0.2Hz, $Z = 3.93$, $p < 1e^{-4}$; 0.5Hz, $Z = 2.43$, $p < 0.05$; 1Hz, $Z = 4.36$, $p < 1e^{-4}$). While this subject experienced an amplification of VOR gain during "Modulation ON" trials, this gain evidently came at a cost of a significant, but modest increase in VOR misalignment (Figure 3.12G) at 0.2, 0.5, and 2Hz (ART two-way repeated measures ANOVA; $F_{[3,829]} = 148.2$, $p < 1e^{-4}$; post hoc pairwise Wilcoxon rank sum tests: 0.2Hz, $Z = 2.88$, $p < 0.01$; 0.5Hz, $Z = 2.87$, $p < 0.01$; 2Hz, $Z = 2.34$, $p < 0.05$).

In summary, these data indicate:

(1) Pre-operatively, VOR performance during natural stimulation was poor, with the low gains and large phases lead typical of BVH.

(2) Post-operatively, VOR performance became significantly more abnormal (consistent with the expected trauma of implantation).

(3) After 8 weeks of continuous motion-modulated stimulation, VOR performance improved to significantly better than pre-op, although still below normal.

(4) Replacing the motion-modulated stimulation with constant-rate and -current stimulation (which should be interpreted by the adapted central nervous system as an absence of head rotation) caused VOR responses to fall nearly to zero.

Taken together, these results suggest that implantation surgery damages natural canal mechanosensory function (analogous to the effect of *cochlear* implant surgery on cochlear function), motion-modulated prosthetic stimulation can improve VOR function to better than pre-op, and adaptation to head-motion-modulated stimulation results in the CNS responding to constant-rate stimulation as though it encodes zero head velocity.

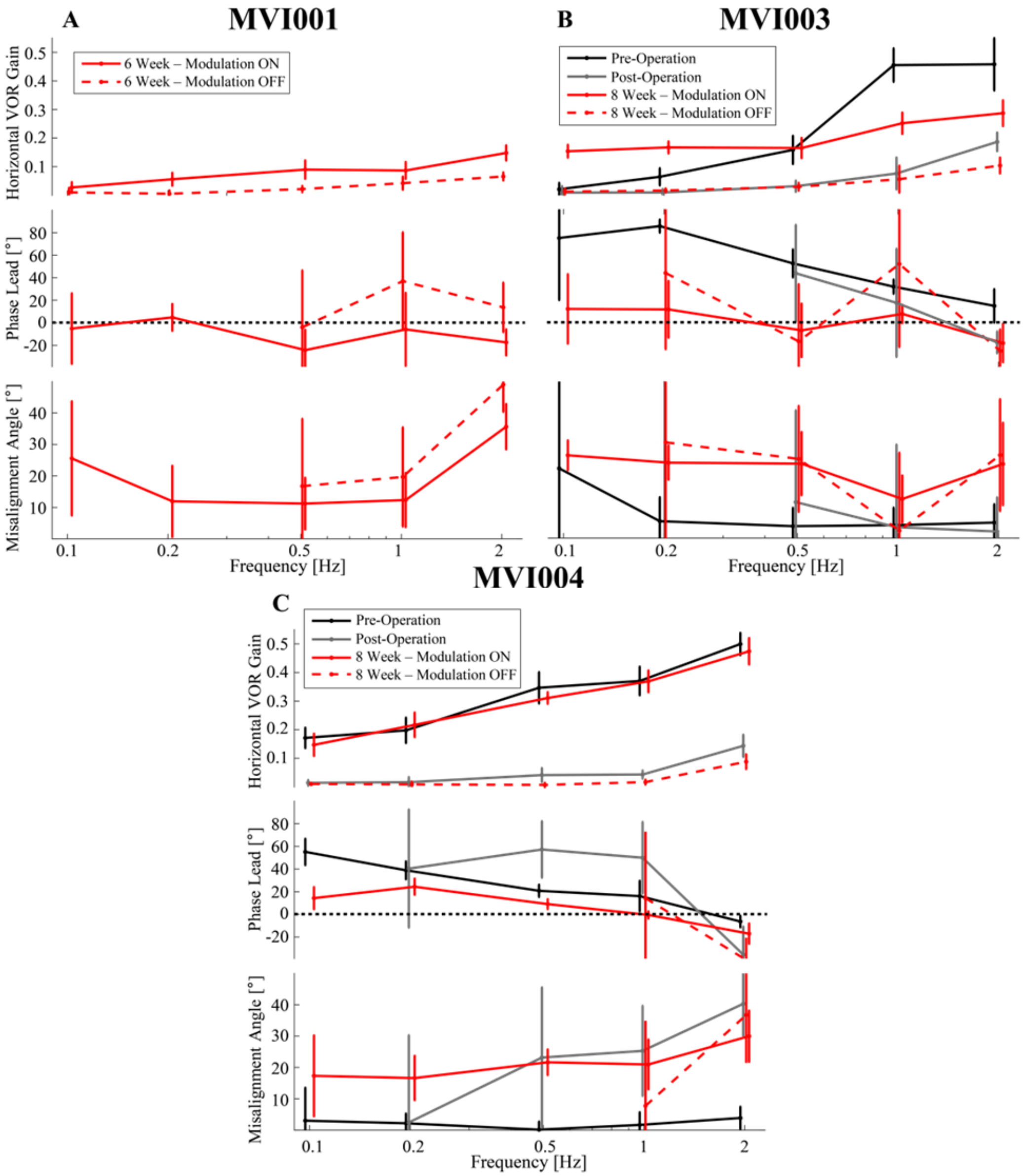

Figure 3.13. Frequency response for combined mechanical and electrical stimulation (MVI001, MVI003, and MVI004. Summarized results from rotary chair testing from subjects (**A**) MVI001, (**B**) MVI003, and (**C**) MVI004. (**A**) Subject MVI001 was not tested pre-operatively or post-operatively before any electrical stimulation. Comparing data recorded after 6 weeks of continuous motion-modulated stimulation in both the "Modulation ON" and "Modulation OFF" conditions, there was a significant increase in VOR gain from 0.2-2Hz (Wilcoxon rank sum tests: 0.2Hz, $Z = 3.38$, $P < 0.001$; 0.5Hz, $Z = 4.19$, $P <$ 1e-4; 1Hz, $Z = 3.55$, $P < 0.001$; 2Hz, $Z = 4.37$, $P <$ 1e-4). (**B**) For subject MVI003, VOR gain significantly increased at 0.1 and 0.2Hz and decreased at 1 and 2Hz (Wilcoxon rank sum tests: 0.1Hz, $Z = 3.07$, $P < 0.01$; 0.2Hz, $Z = 2.93$, $P < 0.01$; 1Hz, $Z = 5.08$, $P <$ 1e-4; 2Hz, $Z = 4.28$, $P <$ 1e-4) when comparing pre-operative data and VOR gain recorded in the "Modulation ON" condition after 8 weeks of motion-modulated stimulation. (**C**) VOR gain recorded from subject MVI004 pre-operatively closely matched data recorded during "Modulation ON" testing after 8 weeks of continuous stimulation, except for 0.5Hz where the increase in VOR gain was significant (Wilcoxon rank sum tests: 0.5Hz, $Z = 2.38$, $P < 0.05$). VOR responses <1.5°/s were too small to accurately estimation of both phase and misalignment.

For subject MVI001 (Figure 3.13A), rotary chair testing was not conducted during the pre-operative test period and thus data acquired after 6-week weeks of MVI™ use in "Modulation ON" (solid red trace) and "Modulation OFF" (dashed red trace) trials are reported alone. These data indicate a high-pass frequency response consistent with data seen in animal models of prosthetic vestibular stimulation, though with low gains at the highest frequencies tested (gain of ~0.14±0.03 at 2Hz). With "Modulation OFF" (dashed line), the excitatory VOR gain decreases across all frequencies, indicating that when modulation is present, central VOR circuits are integrating the motion-modulated electrical stimulus to augment the subject's residual VOR function. The increase in VOR gain was significant for 0.2-2Hz (Wilcoxon rank sum tests: 0.2Hz, $Z = 3.38$, $p < 0.001$; 0.5Hz, $Z = 4.19$, $p < 1e^{-4}$; 1Hz, $Z = 3.55$, $p < 0.001$; 2Hz, $Z = 4.37$, $p < 1e^{-4}$).

For subject MVI003, measurements made post-operatively (but before activating the device) illustrate the reduction in residual vestibular response due to the implantation of the MVI™ electrodes (Figure 3.13B, gray trace). With "Modulation ON" (Figure 3.13B top, solid red trace), this subject shows a significant increase (improvement) in excitatory VOR gain at 0.1 and 0.2Hz compared to pre-operative data (Wilcoxon rank sum tests: 0.1Hz, $Z = 3.07$, $p < 0.01$; 0.2Hz, $Z = 2.93$, $p < 0.01$), almost no change in response at 0.5Hz, and a significant reduction in gain at higher frequency stimuli (Wilcoxon rank sum tests: 1Hz, $Z = 5.08$, $p < 1e^{-4}$; 2Hz, $Z = 4.28$, $p < 1e^{-4}$). The drop in high frequency gain was accompanied by greater (worse) misalignment, probably due to spurious stimulation of non-horizontal ampullary nerve fibers, but also a significant reduction (improvement) in phase lead, resulting in eye movements that were more temporally aligned with head velocity (Wilcoxon rank sum tests: 0.1Hz, Z = 2.29, $p < 0.05$; 0.2Hz, Z = 2.97, $p < 0.01$; 0.5Hz, Z = 4.35, $p < 1e^{-4}$; 1Hz, Z = 5.05, $p < 1e^{-4}$; 2Hz, Z = 4.10, $p < 1e^{-4}$). With “Modulation OFF” (red dashed trace) MVI003 had significantly lower (worse) excitatory VOR responses across all tested frequencies from 0.2-2Hz (Wilcoxon rank sum tests: 0.2Hz, Z = 3.00, $p < 0.01$; 0.5Hz, Z = 4.42, $p < 1e^{-4}$; 1Hz, Z = 4.88, $p < 1e^{-4}$; 2Hz, Z = 4.24, $p < 1e^{-4}$).

Subject MVI004 (Figure 3.13C) produced nearly equivalent VOR gains during pre-operative testing and when tested after 8 weeks of continuous motion-modulated stimulation, apart from a modest but significant increase at 0.5Hz (Wilcoxon rank sum tests: 0.5Hz, Z = 2.38, $p < 0.05$). This subject experienced a significant increase in misalignment (Wilcoxon rank sum tests: 0.2Hz, Z = 4.29, $p < 1e^{-4}$; 0.5Hz, Z = 4.78, $p < 1e^{-4}$; 1Hz, Z = 4.59, $p < 1e^{-4}$; 2Hz, Z = 5.43, $p < 1e^{-4}$) consistent with co-activation of left anterior primary vestibular afferents (as observed previously in Figure 2.7J, Figure 3.5C, and Figure 3.11), but also a significant improvement in phase lead (Wilcoxon rank sum tests: 0.1Hz, Z = 3.72, $p < 0.001$; 0.2Hz, Z = 3.73, $p < 0.001$; 0.5Hz, Z = 4.54, $p < 1e^{-4}$; 1Hz, Z = 3.42, $p < 0.001$; 2Hz, Z = 4.14, $p < 1e^{-4}$). With the system in the “Modulation OFF” setting (Figure 3.13C, dashed red trace), VOR gain significantly dropped below the already small post-operative, pre-activation gain (Figure 3.13C, gray trace) from 0.2-1Hz (Wilcoxon rank sum tests: 0.2Hz, Z = 2.35, $p < 0.05$; 0.5Hz, Z = 4.87, $p < 1e^{-4}$; 1Hz, Z = 4.95, $p < 1e^{-4}$).

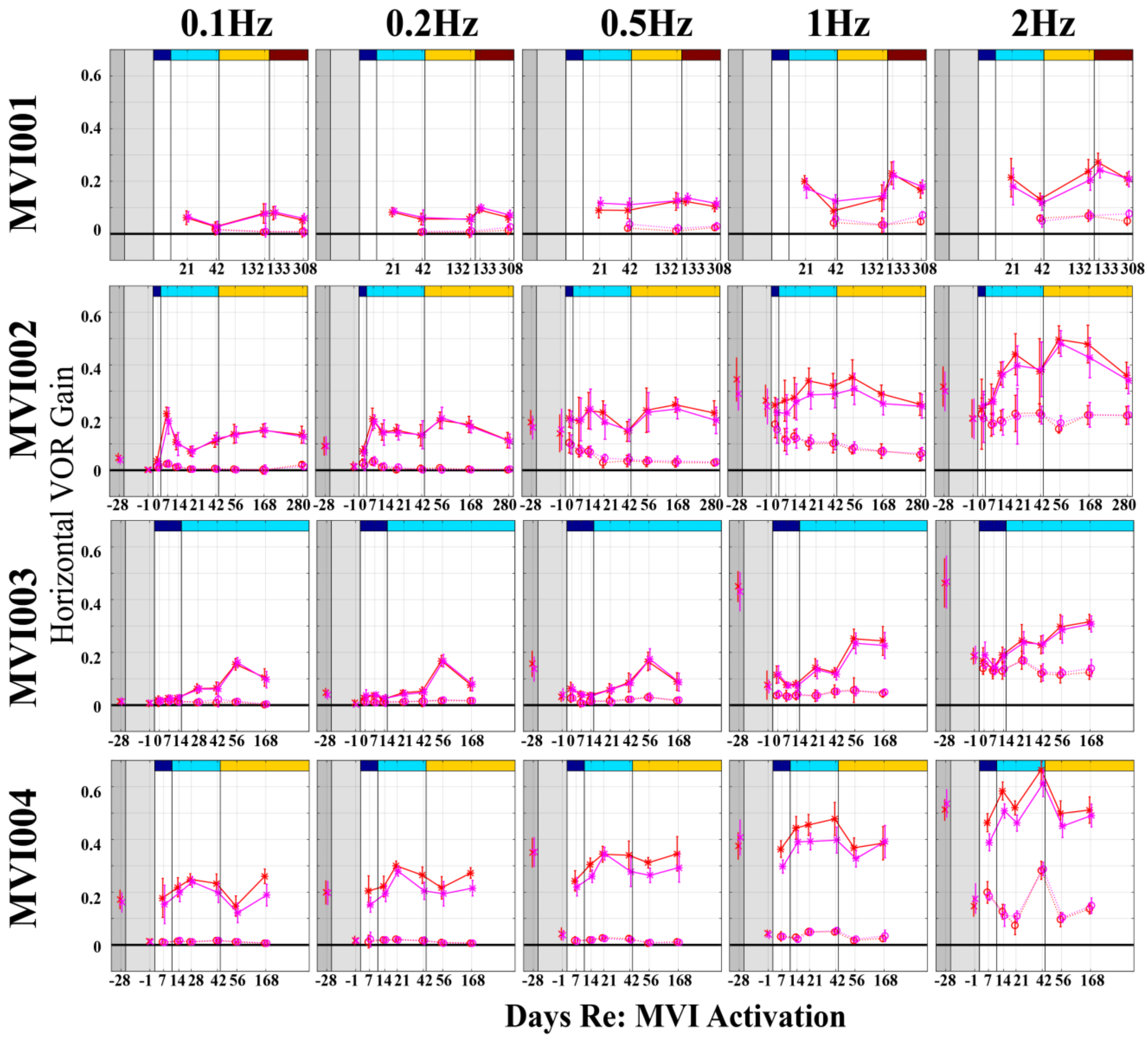

Figure 3.14. Longitudinal horizontal VOR gain assayed using an Earth-vertical rotary chair. Subjects were assayed pre-operatively, post-operatively before any electrical stimulation, and longitudinally up to 308 days after device activation. Horizontal VOR gain during the excitatory (leftward) half cycle is plotted for both the Modulation ON (solid lines) and Modulation OFF (dashed lines) trials during the longitudinal period. Subject MVI001 was not tested before device activation or early visits after device activation. Stimulation parameters programmed for each canal were modified throughout the period of continuous stimulation. Changes in parameters are indicated by the colored bars at the top of each panel and are listed in Table 6.1.

Throughout the post-activation period, changes to each subject's angular VOR were assayed using horizontal mechanical rotations in both Modulation ON and Modulation OFF conditions (Figure 3.14). Subject MVI001 produced stable VOR responses that peaked at ~20°/s at 2Hz in the Modulation ON condition and reduced close to 0 when set to the Modulation OFF state. Subject MVI002 produced an increase in horizontal VOR gain after adding an amplitude modulation mapping on day 42 (Mapping #3, yellow bar in Figure 3.14 second row). In the period following this introduction, the subject experienced a decline in evoked responses across most frequencies, potentially due to the subject resuming anti-anxiety medications (Diazepam) known to suppress vestibular sensation. Data from trials with the device in the Modulation OFF state produced horizontal VOR gains that were in-line or below both pre-operative and post-operative values. For subject MVI003, after introducing amplitude modulation (light blue region in Figure 3.14 third row) horizontal VOR gain increased across the tested frequencies during Modulation ON trials while stimulation parameters remained unchanged. Additionally, this growth was not observed during Modulation OFF trials, providing evidence that central neural circuits are integrating motion-modulated stimulation and relying on evoked responses in canal nerve branches to encode head motion. Subject MVI004 produced horizontal VOR gains that grew over the 168 days post-activation, and throughout the decreases in horizontal amplitude modulation intensity when the subject's PCU was programmed into the Modulation ON condition (colored mappings at the top of Figure 3.14 fourth row). Additionally, responses evoked when the device was programmed into the Modulation OFF state were at or below gains obtained post-operatively.

3.3.5 Subjects report reduction in symptoms

Detailed presentation of dynamic visual acuity and objective measures of posture and gait are beyond the scope of this dissertation; however, the 3D VOR responses detailed above were corroborated by subjects' accounts of symptom improvement, which included categorical changes in their perceived ability to see during head motion and to walk and navigate independently.

An experienced driver and long-distance runner until his gentamicin-induced vestibular loss, subject MVI001 ceased driving entirely after the onset of BVH, and he avoided sitting in the front of a car because his oscillopsia made the scene through the windshield dizzying. Although still going to a gym daily to work out, he had given up outdoor recreational activities such as jogging, sports, and hunting, and he relied on a walking stick during travel. Daily, long-term general fitness and vestibular rehabilitation exercises provided modest subjective benefit that plateaued within a year without categorically changing those aspects of his functional status. After 8 weeks of acclimation to continuous stimulation, he resumed treadmill jogging for the first time since onset of vestibular loss 4 years earlier. Over the subsequent months with continued 24 hour/day use, he resumed outdoor jogging on paved surfaces, went hunting on sandy terrain for the first time in 4 years, mastered jumping rope, took up recreational boxing, and resumed outdoor jogging (though he noted that jogging still causes oscillopsia). He resumed sitting in the front passenger seat of vehicles and wrote that, despite continued adherence to recommendations against driving while using the MVI™, he felt able to resume driving.

Subject MVI002 reported that continuous use of the MVI™ has improved his ability to read signs and perceive faces while walking. Additionally, he described that he felt more comfortable walking without focusing downwards at his feet for the first time in many years. MVI003 transitioned from reliance on furniture, walls or her husband's arm to walking unaided and traveling independently. MVI004 ceased use of an assistive walking pole and realized her goal of resuming independent travel.

3.4 Discussion

Experience of the first four subjects in the Multichannel Vestibular Implant Early Feasibility Study provides strong evidence that a vestibular implant intended to treat bilateral vestibular hypofunction via continuous prosthetic sensory restoration is feasible, efficacious, and effective. In combination with symptom improvements reported by the first four humans to undergo vestibular implantation and continuous, 24 hour/day motion-modulated stimulation, the objective 3D oculographic data presented here provide strong evidence that MVI™ can activate individual semicircular canal nerve branches to evoke directionally appropriate VOR responses.

While previous work with human subjects demonstrated the ability to evoke eye movements in response to occasional experimental sessions of electrical stimulation, the data presented here are unique in that they reveal outcomes after continuous motion-modulated prosthetic stimulation to the human vestibular labyrinth. These data show stable electrically-evoked eye movement responses up to 8-weeks post-activation of the implant, and further responses up to 308 days post-activation with stimulus parameter adjustments. Additionally, this work characterizes eye movements in 3D, allowing a direct assessment of the 3D axis of rotation and component-wise magnitude of evoked responses. While we could not directly assay vestibular afferent fiber activation in this study, characterizing evoked eye movements in 3D rather than 2D allows us to better estimate the relative current spread when delivering electrical stimulation to each electrode contact in the labyrinth.

In this study, subject MVI001 ended the 8 week period of continuous stimulation using only pulse-rate-modulation mapping encoding head rotational velocities, while subjects MVI002, MVI003 (for the LARP and LHRH channels), and MVI004 all ended the same period using a *co-modulation* mapping where both pulse rate and pulse amplitude were modulated to encode rotational velocities about SCC axes (Table 3.1 and Figure 3.2). Previous studies exploring the use of co-modulation encoding schemes for vestibular implants in animal models [34,38] hypothesized that pulse rate modulation mainly controls the spike rate of afferent fibers, while modulating pulse amplitude mainly influences the quantity of recruited afferent fibers (and potentially activates more spurious stimulation of non-target fibers, see section 6.4). While this study did not include a direct comparison of pulse-amplitude- and pulse-rate-modulation, we used a co-modulation scheme to drive enhanced peak eye velocity magnitudes.

In addition, these data provide unique insight into (1) the relative levels to which all 3 human ampullary nerves in an implanted labyrinth are activated and (2) the extent to which eye movements driven by prosthetic stimulation deviate from purely conjugate binocular responses one would expect if stimulus current does not spread to the utricular and saccular nerves. Isolated natural/mechanical stimulation of one or more ampullary nerves, without modulation of utricular or saccular nerve activity, typically produces reflexive binocular vestibulo-ocular responses that are conjugate in 3D (i.e., similar in 3D axis and speed for the left and right eyes) and characterized by an angular velocity component that fades within a few minutes [78,79].

In contrast, natural modulation of utricular and/or saccular nerve activity, as occurs during a static head tilt, centrifugal stimulation, or translational head acceleration, can elicit disconjugate eye movements and persistent deviation in eye angular position from center [7]. Disconjugacy and static eye deviation therefore serve as imperfect proxies for the presence of utricular and/or saccular activity modulation in a test subject instructed not to voluntarily activate vergence, eccentric gaze or other non-vestibular oculomotor systems that elicit disconjugate and static eye deviations. If intense enough to modulate neuronal activity, spurious stimulation might drive otolith-ocular and vestibulospinal reflexes and/or cause illusory perception of head tilt and translation.

Eye movement data presented here suggest that current spread to the utricle and saccule may have elicited otolith-ocular reflex responses, but those responses were relatively small compared to responses driven by ampullary nerves. Prosthetic stimulation targeting one or more ampullary nerves typically produced eye movements that were approximately conjugate in 3D and dominated by angular velocity without static deviation of angular position. This finding supports a conclusion that prosthetic stimulation via electrodes in the ampullae can activate ampullary nerve afferent activity sufficient to drive angular vestibulo-ocular reflexes while comparatively avoiding significant activation of utricular/saccular-ocular reflexes.

An exception to this was seen in subjects MVI001 and MVI002, where stimulation via electrodes in the anterior and posterior canals elicited disconjugate eye movements not only during the initial testing (Figure 2.6A,C, respectively) but also after 8 weeks of continuous motion-modulated stimulation (Figure 3.4 and Figure 3.5) and throughout longer periods of continuous stimulation (Figure 3.6 and Figure 3.7). Interestingly, the pattern of disconjugacy was both electrode- and eye-dependent. For example, stimulation via MVI002's left posterior canal electrode elicited left eye movement aligned with the RALP plane but right eye movement with more nearly equal and opposite polarity LARP and RALP component amplitudes (Figure 2.6, Figure 2.7, and Figure 3.4). An analogous but opposite pattern was observed during electrical stimulation via an electrode in the left anterior canal. The physiologic basis for this pattern is unclear. It was consistently observed in MVI001 and MVI002, but not in all subjects. VOG system artifact was excluded because calibration recordings made during LARP head rotations with a subject viewing an Earth-stationary full-field distant scene in light yielded conjugate eye movements with a mean angle between the left and right eye 3D rotational velocity axes of 9.5±4.5°, significantly less than the 30.5±10.2° evident in Figure 3.4 (Wilcoxon rank sum test: $Z = 2.77$, $p < 0.01$, data is presented in Figure 6.3). This disconjugacy might be due to spurious activation of the utricular and saccular nerves; however, the pattern of utricular/saccular activity that would elicit such eye movement responses is not obvious. Another possibility is a latent esotropia observed in subject MVI002 causing convergence of the eyes during testing in darkness. Previous work investigating the influence of initial binocular 3D position on the angular VOR showed that vergence leads to disconjugate responses during natural stimulation of the posterior and anterior canals [80].

In comparison to the other three subjects, MVI004 produced misaligned response when assaying modulatiing pulsatile stimulation delivered to electrode E6 in the horizontal canal (Figure 3.5C). Evoked responses showed both the intended LHRH component and a spurious LARP component when assayed after 8 weeks of sustained motion-modulated use (and into up to 140 days post-activation in Figure 3.9). This result is consistent with activation of the left horizontal and left anterior ampullary nerves when modulating both the pulse rate and current amplitude of the electrical stimulus, creating more misaligned responses compared to modulation of pulse rate alone (example shown in Figure 6.4). Previous studies in chinchillas [33] and non-human primates [37] provided strong evidence that VOR directional plasticity mechanisms rapidly and significantly minimized off-axis VOR components over the first 7 days of continuous, motion-modulated prosthetic stimulation, presumably via the same sort of neuronal learning mechanisms that can reorient VOR direction when a normal subject views the world through prisms or other optical manipulations that cause the visual scene to rotate about an axis other than the exact inverse of the head rotation axis [81–84]. In this study, MVI004 did not show this cross-axis adaptation effect (as evidenced by the strong LARP component seen binocularly 140 days post-activation in Figure 3.9). One potential reason could be the difference in encoding schemes used in each scenario. The pre-clinical animal studies only used pulse-rate-modulation to encode head rotations, likely creating a uniform electric field during modulation of pulsatile stimulation to encode head rotations. In contrast, subject MVI004's device was programmed to modulate both pulse rate and current amplitude, changing the amount of charge injected to encode head velocity waveforms.

When assaying VOR responses to sinusoidal whole body rotations after MVI™ implantation and activation, our data show both an increased VOR gain at low frequencies (in subjects MVI002 and MVI003) and an increased reliance on motion-modulated input (for all subjects). After 8 weeks of continuous stimulation, data measured with the device temporarily set to the "Modulation OFF" (constant stimulus pulse rate and amplitude) condition (Figure 3.12E and Figure 3.13, dashed red traces) produced reduced left-sided excitatory VOR gains compared to data recorded pre-operatively (Figure 3.12E and Figure 3.13, black traces) and values recorded 3 weeks after implantation, but before initial activation (Figure 3.12E and Figure 3.13, gray traces). This reduction in the evoked eye movement when turning off motion-modulation suggests continuous stimulation has adjusted central VOR circuitry to rely upon prosthetic input to encode head motion. When integration of head motion data from the HWU is turned off ("Modulation OFF" condition), the tonic electrical current and stimulation rate provide a pattern of neural activity that signals the subject's head is not moving. This static signal may conflict with the latent mechanical sensitivity in the non-operated ear and reduce the evoked VOR response below post-operative responses. Data acquired past the 8 week period for are consistent with these findings for all subjects (Figure 3.14).

The 3D VOR responses reported in this study indicate MVI™ stimulation is providing patterned activity in canal afferent nerve bundles that produce eye movements that closely approximate anatomic canal axes, can be combined to encode arbitrary 3D vectors, and can be scaled with modulation intensity. However, the overall eye movement magnitudes evoked in these human subjects were below the amplitudes generated in studies with non-human primates [35–40], chinchillas [30–34], and guinea pigs [24–28]. While anatomical and physiological differences between species may explain the modest responses seen in our human subjects, variances between the experimental design of pre-clinical studies and the etiologies of our human subjects may provide insight into the modest observed responses. In pre-clinical experiments adult animals used were treated with intratympanic injections of gentamicin to cause partial vestibular hair cell loss and consequently BVH, as indicated by a severe reduction in VOR gain during whole-body rotation in darkness [36]. Additionally, the animals used in those studies were prosthetically stimulated within months after gentamicin treatment. In contrast, the human subjects participating in the present study were all older individuals who received ototoxic doses of aminoglycoside during their pre-enrollment insult that was delivered via intravenous delivery (MVI001, MVI003, MVI004) or intratympanically using streptomycin (MVI002). Additionally, the ototoxic events occurred between 1.5 and 9 years before participating in this study. The long delay between the loss of afferent activity from the injury and the prosthetic intervention may have induced neuronal decay not seen in animal models where experiments began shortly after the intratympanic injections [85]. Conversely many acute studies in animals produced robust VOR responses with intermittent electrical stimulation during experiments assaying implant function, with long stretches without prosthetic stimulation while animals were participating in other studies (in particular, the data presented in Chapter 4 was acquired >4 years after intratympanic gentamicin treatment in both animals without continuous stimulation between experiments for more than 7 days).

Chapter 4 Effect of Temporal Discretization on the Electrically-Evoked VOR

4.1 Introduction

Cochlear implants (CIs) aimed to restore hearing sensation in individuals suffering from profound sensorineural hearing loss use a linear array of electrode contacts to electrically stimulate the auditory nerve at different locations along the cochlea's tonotopic axis. Early signal processing schemes encoded individual frequency band waveforms via continuous analog (CA) modulation of electrical current delivered concurrently to each electrode in the intracochlear array [1,2]. While initially successful, simultaneous delivery of current across multiple channels produced broad activation of spiral ganglion neurons, causing distortion of perceived auditory cues. To reduce current spread to non-target neural fibers, researchers at the Research Triangle Institute (RTI) developed the continuous interleaved sampling (CIS) cochlear implant stimulation strategy to asynchronously deliver pulses to each intracochlear contact [86].

In CIS, the pulse frequency of the electrical stimulus is held constant and each stimulation channel is amplitude modulated to encode a frequency banded envelope in a non-overlapping, “round robin”-type fashion. This spatial separation of activated electrode contacts provided an increase in the quantity of functional stimulation channels and improved speech recognition over previous CA processors [86]. Modern CIs use a variation of the CIS approach, where additional signal processing schemes usually aim to encode the fine structure or fundamental frequency of each band to enhance auditory perception [88].

To further development of a commercially viable vestibular implant (VI) aimed as a clinical treatment for BVH, it would be advantageous to integrate existing CI stimulators to leverage advances in miniaturized stimulator design and lower the regulatory burden for a commercial VI device. Additionally, BVH candidates for a future VI may also suffer from hearing loss that can be treated with a CI, motivating merging VI and CI technologies. Moreover, if the VI portion of a combined VI/CI device requires only a subset of the stimulator’s electrodes, the remaining electrodes could be implanted in the cochlea and used for hearing restoration.

Using pulse-frequency-modulation (PFM) to encode head motion via prosthetic electrical stimulation has been successful in many pre-clinical [24,25,30,31,33,35–40,89] and pilot clinical studies [47] of VI technology. These studies used smooth modulation of stimulus pulse frequency above/below an adapted electrical stimulus rate to mimic the spike rate modulations about the spontaneous discharge rate of primary vestibular afferent fibers [76,90]. While other studies have shown pulse-amplitude-modulation (PAM) can successfully evoke compensatory VOR responses [39,40,44–46,52], successfully integrating PFM stimulus encoding methods into a CIS signal processing framework would promote the development of a future VI/CI combined device.

Merging a PFM-based VI and a CIS-based CI creates a tradeoff, as temporal discretization necessary for the round-robin CIS approach prevents the smooth modulation of pulse frequency, creating errors in patterned timing of pulsatile stimuli. While these errors would distort the temporal dynamics of pulsatile waveforms used to encode head velocity, we hypothesize that they will produce negligible effects on the gain, phase, and misalignment of evoked eye movements due to the low-pass filtering inherent to VOR circuitry.

To test this hypothesis, we created two head velocity-to-pulse rate maps to encode head motion: a smooth PFM map (sPFM) that continuously modulates stimulus pulse frequency with head velocity and a map corrupted by temporal discretization errors (dPFM) typifying errors that would occur in a VI/CI using CIS. We tested both mappings using a series of virtual head velocity waveforms and assayed evoked 3D VOR responses in two rhesus macaques.

4.2 Methods

4.2.1 Surgical procedures

Two female rhesus macaques (RhF20124B and RhF060738G, 5-7 kg) were used for all experiments performed in accordance with a protocol approved by the Johns Hopkins Animal Care and Use Committee. Methods of head cap assembly for head-fixation and dual scleral magnetic search coil implantation in primates have been described previously [35,91–93]. In brief, using general inhalational anesthesia (1.5-5% isoflurane) and sterile conditions, a head cap constructed from poly-ether-ether-ketone was attached to the skull using poly-methyl methacrylate and titanium bone screws. Two search coils were fabricated from Teflon-coated steel wire (Cooner Wire, Chatsworth, CA). Wire leads were tightly twisted to minimize artifacts induced in the magnetic search coil system. Connectors were fashioned out of 1mm pitch pin headers and routed out of the animal's head cap. Both coils were sutured to the sclera of one eye (left eye for RhF20124B and right eye for RhF060738G), with one coil implanted around the iris and the other positioned approximately orthogonal to the first. Post-operative procedures included treatment with analgesics and antibiotics for ~72 hours.

After characterization of each animal's natural vestibular function, an electrode array was implanted into the left labyrinth using a transmastoid approach analogous to that used for cochlear implantation, but with a transcutaneous connector embedded in the animal's head cap [33,38]. RhF20124B was implanted with an electrode array fashioned from pairs of Teflon-insulated Pt-Ir wire (Cooner Wire, Chatsworth, CA) for each stimulating electrode and reference electrodes. This electrode array used 6 stimulating electrodes (E0-1 in the left anterior canal, E2-3 in the left horizontal canal, and E5-6 in the left posterior canal) and two reference electrodes (E4 in the common crus and E7 near temporalis muscle). RhF060738G was implanted with an electrode array designed using 3D reconstructions of CT images of rhesus macaque vestibular labyrinths [35]. This array comprises nine stimulation electrodes (E1-3 in the left posterior canal, E4-6 in the left horizontal canal, and E7-9 in the left anterior canal) and two reference electrodes (E10 located near the temporalis musculature and E11 in the common crus) all embedded within a silicone carrier, where electrode contacts and leads are fabricated from a 90/10 platinum/iridium alloy.

Following unilateral electrode implantation, each animal underwent bilateral intratympanic gentamicin treatment using a modified procedure typically performed in humans [9], adjusted with the use of general inhalational anesthesia (1.5-5% isoflurane) for ~30 minutes with the left ear reoriented up to promote diffusion into the inner ear. Each treatment consisted of ~0.5 mL of 26.7 mg/mL buffered gentamicin solution injected through the ear drum into the middle ear. VOR responses were assayed ~3 weeks after treatment and gentamicin injections were repeated until VOR gains across all treated canals were <10% of normal characterized gains. Typically this required 2-3 injections per ear for each animal of this study. Re-injections such as this are not uncommon in human patients treated with gentamicin to reduce symptoms associated with Ménière's disease [94].

4.2.2 Eye movement recording

The search coil system used to record 3D eye movements has been described in detail previously [91,93]. Each animal was seated in a plastic chair and restrained by the implanted head cap. The coil system superstructure comprised three pairs of field coils generating magnetic fields along the X (naso-occipital, +nasal), Y (interaural, +left), and Z (superoinferior, +superior) axes of the monkey's restrained head and oscillated at 79, 53 and 40kHz, respectively. Each animal's head was reoriented about the +Y-axis either +15° (RhF20124B) or +2° (RhF060738G) to align the animal's horizontal canal plane (as estimated using CT scans acquired after head cap implantation [60]) with the Earth horizontal plane. Currents induced on scleral search coils were demodulated to produce voltages proportional to the angles between each coil and the three magnetic fields. All signals were filtered using an analog eight-pole Butterworth low pass filter with a corner frequency of 100Hz and sampled at 1kHz. Misalignments between positioning of the two coils were corrected using an algorithm for computing instantaneous angular position of the implanted dual coil pair when they are not exactly orthogonal.

4.2.3 Data analysis and statistics

Rotation vectors describing angular position in X ('roll'), Y ('pitch'), and Z ('yaw') coordinates were calculated from raw search coil data using standard techniques [91,93,95], including an algorithm for correcting misalignments between positioning of the two coils when they are not exactly orthogonal [96]. 3D angular velocity vectors were computed from the rotation vectors [57], transformed into components along the mean anatomic axes of the LARP, RALP, and LHRH coplanar canal pairs, and smoothed using a running spline interpolation filter. All polarities are expressed using right hand rule conventions. A custom semi-automatic algorithm detected quick phases of elicited vestibular responses, blanked out the detected region, and connected over blanked regions using spline interpolation. Responses along each 3D component were separately cycle-averaged after removing cycles corrupted by blinks.

To compare VOR performance for each mapping, we computed peak eye velocity, phase lead, and misalignment for each stimulus condition. The peak eye velocity was determined by finding the largest magnitude eye velocity about the correct canal axis with appropriate polarity. For example, excitation of the left horizontal ampullary nerve branch should encode head rotation to the left (positive by convention) and produce a compensatory eye movement to the right (negative by convention). In contrast, excitation of the left posterior and left anterior canals encode conventionally negative head velocities and thus should produce a positive slow phase eye velocity in the intended plane. The component-wise angular velocity magnitudes at this peak determined the VOR response vector. This vector was normalized with its L^2 norm to produce a unit vector axis of rotation for the 3D VOR response. A positive phase lead was defined where the VOR response leads the inverse of head velocity. Lastly, misalignment was defined as the angle between the unit vector VOR axis of rotation and the ideal canal axis. All values are reported as mean ± one standard deviation.

Statistical analysis was performed in Matlab (Mathworks, Natick, Massachusetts) and R (RStudio, Inc., Boston, MA) to evaluate differences between the sPFM and dPFM mappings. Eye movement responses often did not meet normality criteria necessary for standard analysis of variance (ANOVA) and post hoc t test methods. For this reason, we used the aligned rank transform (ART) procedure [61–63] to perform non-parametric, multi-factorial repeated measures ANOVA hypothesis testing and post hoc Wilcoxon rank sum tests for pairwise comparisons where necessary, with statistical significance set to $p < 0.05$. In these tests we used factors of *Mapping* ("sPFM" and "dPFM") and either *Frequency* (0.1-2Hz) or *Intensity* (50-400°/s).

4.2.4 Stimulation paradigm

Electrical stimulation was delivered using a MED-EL PULSAR CI100 stimulator, a hardware interface box (either the Research Interface Box developed at the University of Innsbruck [77] or the MED-EL MAX Programming Interface), and a custom Matlab software package in a manner analogous to work described previously [97]. The stimulator was programmed to deliver biphasic, charge balanced 150µs/phase current pulses with no interphase gap delivered to the electrode arrays implanted in each canal using the common crus electrode as the return/reference contact. Calibration experiments using mock electrode arrays with series sense resistors confirmed the stimulator faithfully delivered current pulse waveforms.

For all experiments described here we wanted to isolate the effect of each PFM mapping and remove any contributions from residual vestibular function, visual input, or any non-prosthetic influence to the evoked responses. The animal's head was held stationary within the plastic chair, the superstructure was locked in place, and the lights in the experimental chamber were all turned off. A LED was illuminated directly in front of the animal between trials to re-center gaze.

	RALP		**LHRH**		**LARP**	
Animal ID	**Electrode Contact**	**Pulse Amp. [µA]**	**Electrode Contact**	**Pulse Amp. [µA]**	**Electrode Contact**	**Pulse Amp. [µA]**
RhF20124B	E5	150	E3	150	E0	150
RhF060738G	E2	375	E8	200	E5	275

Table 4.1 Summary of electrode contacts and current levels for discrete pulse-frequency-modulation (dPFM) experiments. All electrical stimuli used 150µs/phase biphasic, charge balanced current pulses. Note, different electrode arrays were implanted in each animal. Refer to section 944.2.1 for full details of each array.

At the start of each experiment, the animal was adapted to a constant current amplitude, 94 pulse-per-second (pps) electrical stimulus aimed to mimic the resting discharge rate of primary vestibular afferent fibers in rhesus macaques [76]. The active electrode and current amplitude within each canal was chosen to maximize evoked VOR magnitude and minimize 3D misalignment as defined above. Electrode contacts and current amplitudes are outlined in Table 4.1. Animals were acclimated to this tonic electrical stimulus in light with an Earth-fixed target, and brief intermittent periods in darkness to isolate eye movement responses. This procedure lasted between 60-90 minutes and continued until the evoked slow phase nystagmus dropped below 5°/s.

After the animal was acclimated to constant current/rate stimulation, pulsatile stimulus waveforms encoding a series of sinusoidal head velocity waveforms tested VOR responses using both the sPFM and dPFM mapping. Each virtual head velocity waveform targeted a single canal via modulation of the baseline rate on that canal's active electrode while holding the pulsatile rate of the active electrodes on the other canals at 94pps. Virtual head velocity waveforms tested each mapping encoding different peak head velocities (50-400°/s at 0.5Hz) and different stimulus frequencies (0.1-2Hz at 300°/s peak velocity) with the animal's head stationary.

4.2.5 Discrete Pulse Frequency Modulation (dPFM) mapping

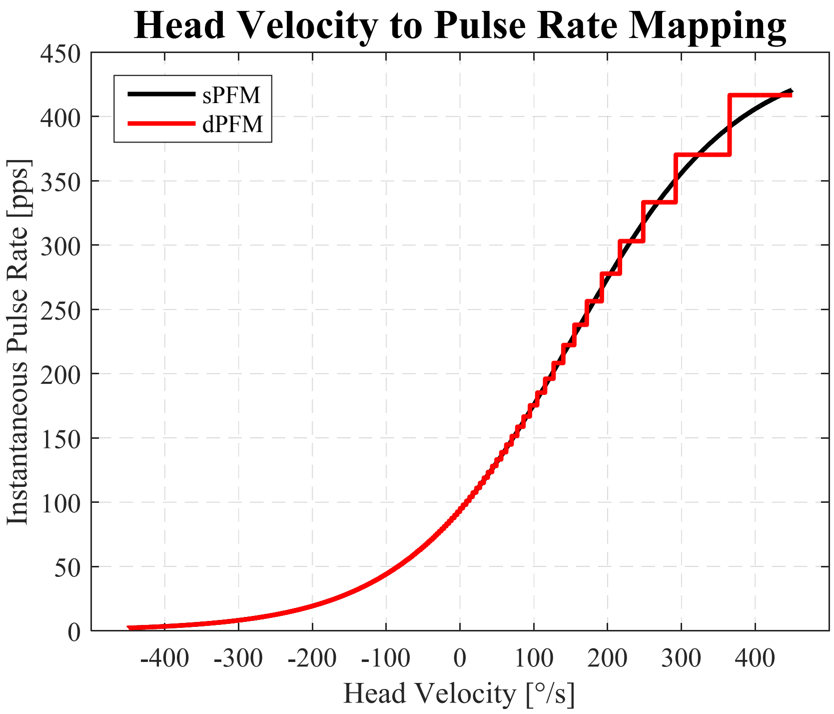

Figure 4.1: Head velocity-to-pulse rate maps encoding head motion using pulse-frequency-modulation (PFM). Each animal was tested using both a smooth pulse-frequency-modulation (sPFM, black in figure) and a discretized PFM map (dPFM, red in figure) representing the discretization inherent to a cochlear implant (CI) using a continuous interleaved sampling (CIS) signal processing strategy. : smooth PFM (sPFM). The dPFM map was constructed by assuming the maximum pulse rate possible on the stimulator used in the study (PULSAR CI100 with a maximum total pulse rate of 50K pps) was divided among 15 electrodes in a round-robin-type fashion (3 electrodes dedicated to vestibular PFM stimulation and 12 electrodes assumed to be routed to a linear cochlear array). This reduces the maximum per-channel rate of ~3,333pps, and thus a minimum inter-pulse-interval (IPI_0) of 300μs. Thus, to deliver high pulse rates used to encode large positive angular velocities, the dPFM mapping approximates the desired pulse rate using integer multiples of IPI_0, creating stair-step discontinuities.

Each mapping was generated using a sigmoid curve (similar to that described in section 3.2.1) with a pulse rate corresponding to no motion (0°/s) of 94 pps and a maximum input velocity of 450°/s (corresponding to a peak pulse rate of ~425pps) [36,97]. For the dPFM map (Figure 4.1), we modeled a combined VI/CI with a maximum aggregate pulse rate of 50kpps (such as the MED-EL PULSAR device), a total of 12 CI channels spanning the cochlea's tonotopic axis, and 3 VI channels for each canal in the left ear. Such a device would be capable of stimulating a single electrode at a maximum per channel rate of ~3,333pps (i.e., a minimum inter-pulse-interval (IPI_0) of 300μs). The CPU of such a device would determine if the stimulator delivers a pulse every 300μs on each channel in a round-robin, CIS-like fashion. For example, to approximate a desired pulse rate of ~335pps, the dPFM map would deliver a pulse after waiting of $10{*}IPI_0$ (i.e., deliver a pulse every 10*300μs, or 3ms constructing a ~333pps instantaneous pulse rate). The dPFM mapping uses this integer multiple of IPI_0 to approximate all target pulse rates between 317-351pps (and thus encoding head velocities between ~248-292°/s according to the sPFM map).

This per-channel rate is advantageous for the CI portion of the proposed device, as high constant pulse rate stimulation allows smooth amplitude modulation to encode the envelope of sound for a given CI frequency band. Yet for the VI portion of a combined implant, using a dPFM coding scheme constrains pulse rates to $\frac{1}{K*IPI_0}$, where K is an integer. For low stimulus pulse rates (and thus long inter-pulse-intervals) this does not pose a substantial problem; the desired rate can be closely approximated (i.e., Figure 4.1 between -450°/s and 0°/s). For high pulse rates (or short inter-pulse-intervals, Figure 4.1

between 100°/s and 450°/s), only a single integer multiple of IPI_0 can approximate the desired rate for a range of input velocities. This approximation discretizes the sPFM map, creating 'stair-step' discontinuities as seen in Figure 4.1.

The discretization seen when approximating high rate stimuli is exacerbated when using the dPFM mapping to encode low frequency head velocity stimuli where the pulse frequency needs to stay in high pulse rate regions of the head velocity-to-pulse rate mapping for sustained modulation periods. For example when encoding a 0.1Hz (Figure 4.2A) or 1Hz (Figure 4.2B) 50°/s sinusoidal head velocity waveform the dPFM map closely approximates the instantaneous pulse rate used to encode the head velocity waveform. The 0.1Hz stimulus spends more time in the highly discretized region at the peak of the waveform compared to the 1Hz stimulus, though both accurately approximate the desired stimulus waveform.

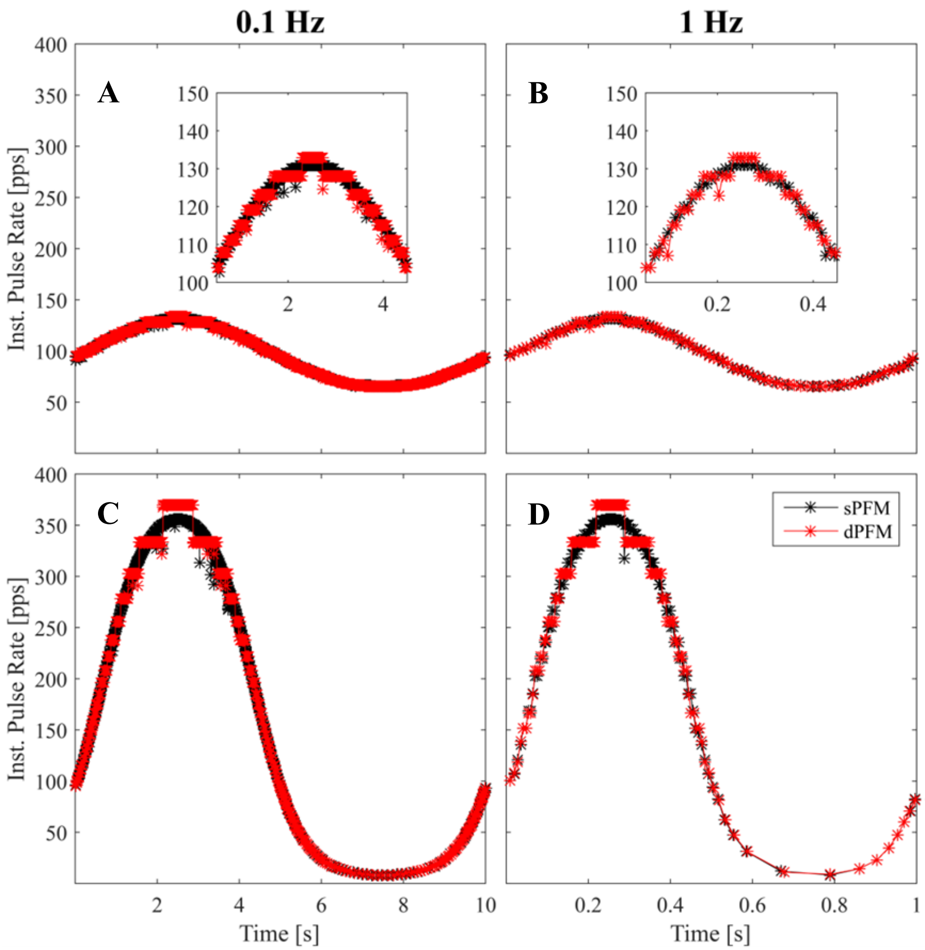

Figure 4.2: Examples of PFM waveforms using the sPFM and sPFM mappings. Example pulsatile waveforms using PFM to encode sinusoidal head rotations generated using the sPFM (black markers) and dPFM (red markers) at (**A**,**C**) 0.1Hz and (**B**,**D**) 1Hz. When encoding lower amplitude 50°/s stimuli (**A**,**B**), the dPFM mapping closely approximates the smooth sPFM waveform. In contrast, when encoding large amplitude stimuli (300°/s, **C**,**D**) the dPFM creates stair step discontinuities that discretize the prosthesis output.

When peak rotational head velocity amplitude increases into the heavily discretized region of the dPFM mapping, the resulting PFM waveform no longer accurately approximates the sPFM signal creating significant temporal errors. For example when coding 300°/s sinusoidal stimuli (Figure 4.2C,D), the instantaneous pulse rate delivered to encode the head velocity waveform becomes jagged with "stair-step" discontinuities and overshoots the peak pulse rate (i.e., the sPFM map called for a pulse rate of 356pps coding a 300°/s head velocity, where the closest dPFM approximation is 370pps).

To quantify the differences in evoked VOR responses with both mappings, we will perform an intensity series at 0.5Hz to assay changes in VOR responses using a range of peak virtual head velocity amplitudes large amplitude stimuli (50-400°/s). Additionally, we will quantify differences in the electrically-evoked VOR as a function of stimulus frequency by assaying responses to a series of virtual sinusoidal waveforms with frequencies from 0.1-5Hz with a 300°/s peak head velocity.

4.3 Results

4.3.1 dPFM produces robust, selective eye movements

Sinusoidal modulation of pulse frequency delivered to primary vestibular afferents in both animals produced robust 3D eye movements that rotate about axes that approximate anatomic canal axes of the targeted canals (exemplified with animal RhF060738G in Figure 4.3). Virtual head velocity waveforms representing 0.5Hz, 300°/s head motions about the RALP (Figure 4.3A,B), LHRH (Figure 4.3C,D), and LARP (Figure 4.3E,F) canal axes produced robust (~150°/s peak velocity), directionally appropriate slow phase compensatory responses that were dominated by the intended canal component. Additionally, large opposite polarity quick phases during excitatory half-cycles are seen in all examples of both mappings, consistent with PFM stimulation creating afferent spike patterns activating downstream VOR circuits in a manner comparable to the healthy vestibular periphery.

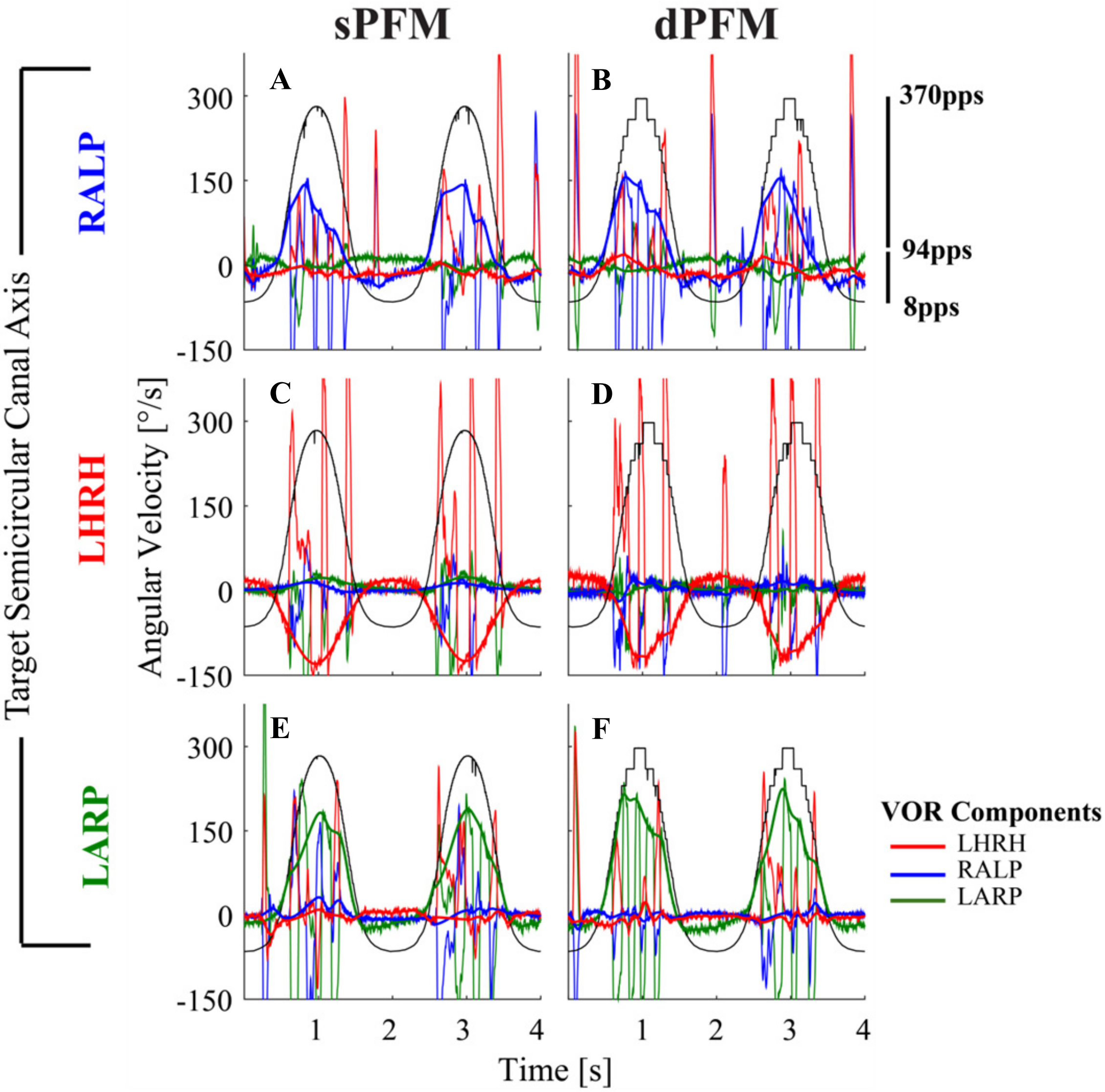

Figure 4.3: Raw / processed 3D aVOR data using sPFM and dPFM mappings. Electrically-evoked VOR responses to 300°/s virtual 0.5Hz sinusoidal stimuli in the LARP plane in animal RhF060738G. Eye velocity is decomposed into LARP (green), RALP (blue), and LHRH (red) components. The PFM stimulus rate is plotted in black for reference.

After removing quick phases from 3D traces and cycle averaging responses uncontaminated by blinks (Figure 4.4), the sPFM and dPFM mappings produced nearly equivalent 3D VOR waveforms across each canal with minimal cross-talk to non-target canal afferents. Additionally these examples demonstrate an excitation/inhibition asymmetry, where excitatory phases for each virtual head velocity waveform (representing ipsiversive head motion and corresponding to an increase in the stimulus pulse rate) producing larger magnitude eye movements compared to the inhibitory half cycle (encoding contraversive head velocities by decreasing pulse rates).

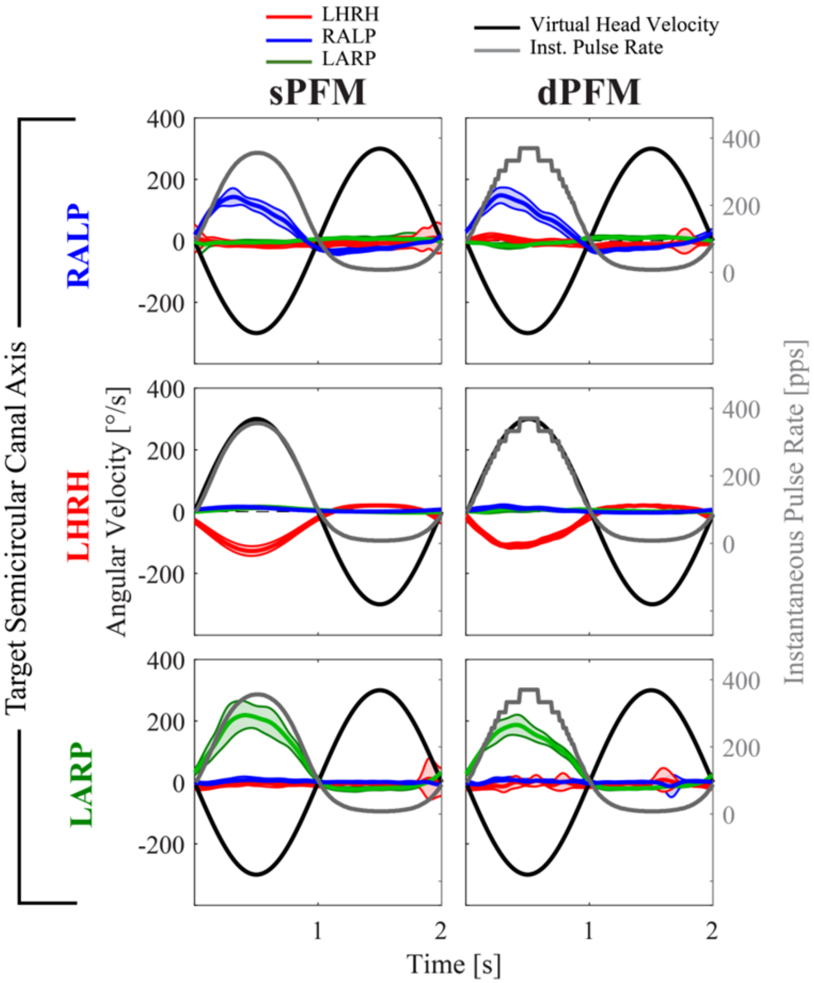

Figure 4.4: Cycle averaged 3D VOR responses to the sPFM and dPFM mappings. 3D cycle averaged responses from animal RhF060738G from 0.5Hz, 300°/s stimuli delivered to electrode contacts in each canal. Virtual head velocity traces are shown in black, while dynamics of instantaneous pulse rate are shown in gray. Note, due to the right-hand-rule convention used in data analysis, the head velocity waveform for LARP and RALP stimulation is shown as negative leading, while the LHRH waveform is positive leading.

4.3.2 Effect of dPFM mapping on encoding head velocity

Sweeps of PFM intensity to encode virtual 0.5Hz sinusoids with different peak velocities amplitudes evaluated the effect of temporal discretization on encoding head velocity (Figure 4.5). For this experiment, 0.5Hz was chosen as a tradeoff between using a slow enough stimulus modulation frequency to add sufficient durations of discretization and the time needed to acquire a complete data set during experimental sessions. Virtual peak head velocities ranged from 50-400°/s, where larger amplitude peak velocities inherently produce more temporal discretization compared to slower head motions (Figure 4.2 top vs. row). In this case, we expect lower amplitude stimuli using the dPFM mapping to evoke similar eye movements compared to the sPFM mapping, since in this region of the dPFM mapping pulse train patterns closely approximate the smooth, sPFM version. In contrast, at high amplitude peak head velocities, the peak amplitude region of the stimulus creates longer durations of 'flat' transient steps in pulse frequency.

The electrically-evoked VOR produced nearly identical peak slow phase eye velocities about the intended canal axis when stimuli were processed using both the sPFM and dPFM mappings in both animals (Figure 4.5A-F). Peak eye velocity steadily increased with virtual head velocity up to 300°/s and plateaued or slightly decreased when tested with 400°/s peak velocity virtual sinusoids, showing a possible saturation of the electrically-evoked VOR. Using both mappings VOR peak amplitudes reached >120°/s across all canals, while stimuli delivered to the left anterior canal in animal RhF060738G (Figure 4.5C) and the left horizontal canal in animal RhF20124B (Figure 4.5E) reached ~200°/s.

To assay the 3D alignment of the evoked 3D VOR response, we computed the angle between evoked 3D VOR axes of rotation and the ideal anatomic canal axis (Figure 4.5G-L). In most cases, the misalignment angle remained <10° as the VOR magnitude grew indicating selective activation of the targeted canal afferent nerve branches. In animal RhF20124B during modulation of the electrical stimulus delivered to the left anterior canal (Figure 4.5L) the misalignment remained ~30° through all levels tested due to global excitation of the labyrinth, producing unintended RALP and LHRH 3D components with both mappings.

Overall, both mappings produced consistent 3D VOR responses throughout the entire programmed head velocity input range. Small differences in 3D VOR responses were not significant for each frequency tested (ART two-way repeated measures ANOVA; RALP: $F_{[1,262]} = 1.55$, $p = 0.21$; LHRH: $F_{[1,308]} = 0.64$, $p = 0.43$; LARP: $F_{[1,293]} = 2.54$, $p = 0.11$) indicating that temporal discretization present in the dPFM mapping does not affect vestibular prosthetic encoding of angular head velocity peak amplitude.

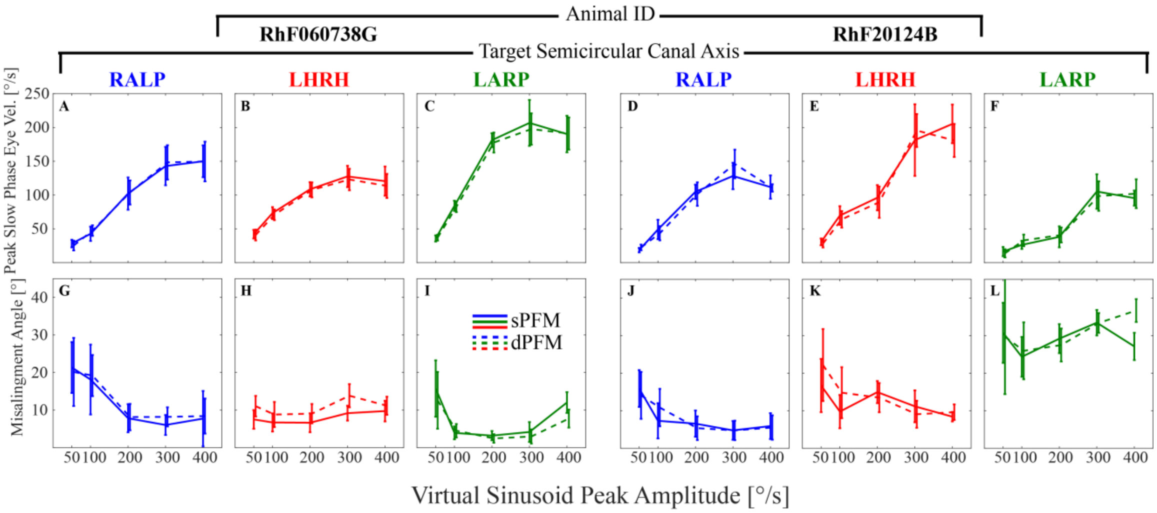

Figure 4.5: dPFM vs. sPFM amplitude sweep summary. Virtual head velocity waveforms processed using both the sPFM (solid lines) and dPFM (dashed lines) produced nearly identical 3D VOR responses in both RhF060738G (**A-C**,**G-I**) and RhF20124B (**D-F**,**J-L**). Differences in peak slow phase velocity and misalignment angle were not significant (ART two-way repeated measures ANOVA; RALP: $F_{[1,262]} = 1.55$, $p = 0.21$; LHRH: $F_{[1,308]} = 0.64$, $p = 0.43$; LARP: $F_{[1,293]} = 2.54$, $p = 0.11$)

4.3.3 Effect of dPFM mapping on encoding head motion frequency

In addition to encoding peak head velocity, VI technology aimed to prosthetically replicate natural vestibular function should faithfully encode frequency response characteristics of the vestibular periphery and drive a compensatory VOR. This goal is complicated when using a dPFM map, where low frequency head motion stimuli produce PFM pulsatile waveforms with increased durations of temporal discretization (i.e., more time-per-cycle in the 'discretized' region of the dPFM mapping in Figure 4.1). To examine the effect of temporal discretization on frequency response characteristics of the eeVOR, we assayed 3D VOR responses to virtual sinusoidal head velocity stimuli between 0.1-5Hz with 300°/s peak head velocities. This high amplitude was chosen to examine an extreme case of temporal errors and maximize the discretization effects of the mapping.

Data acquired with sPFM and dPFM mappings produced nearly equivalent magnitude responses across both animals and all 6 tested canals (Figure 4.6A-F). Consistent with data reported previously, prosthetic vestibular stimulation using sinusoidal PFM encoding produces a high-pass response characteristic. In both animals, electrodes in the left posterior canal (Figure 4.6A,D) produced the largest gains, seen at 2 and 5Hz. Animal RhF060738G produced a gain of 1 (and thus an angular velocity of ~300°/s) at these frequencies, while animal RhF20124B generated gains >1 at 5Hz.

Phase lead and misalignment response characteristics from both mappings were near equivalent for the frequency band tested. Response profiles indicate a 20-30° phase lead that decreased as a function of frequency, with a slight phase lag at 5Hz. Response misalignment remained low across frequency for animal RhF060738G, indicating well aligned 3D VOR responses. Animal RhF20124B produced less aligned responses consistently across both mappings.

Differences in VOR frequency response characteristics were not significant between the dPFM and sPFM mappings (ART two-way repeated measures ANOVA; RALP: $F_{[1,311]} = 2.15$, $p = 0.14$; LHRH: $F_{[1,413]} = 0.70$, $p = 0.40$; LARP: $F_{[1,258]} = 1.94$, $p = 0.17$). The negligible changes in VOR gain, phase response, and 3D alignment indicate that reducing temporal resolution should have a minimal effect on VI performance of a future combine VI/CI device.

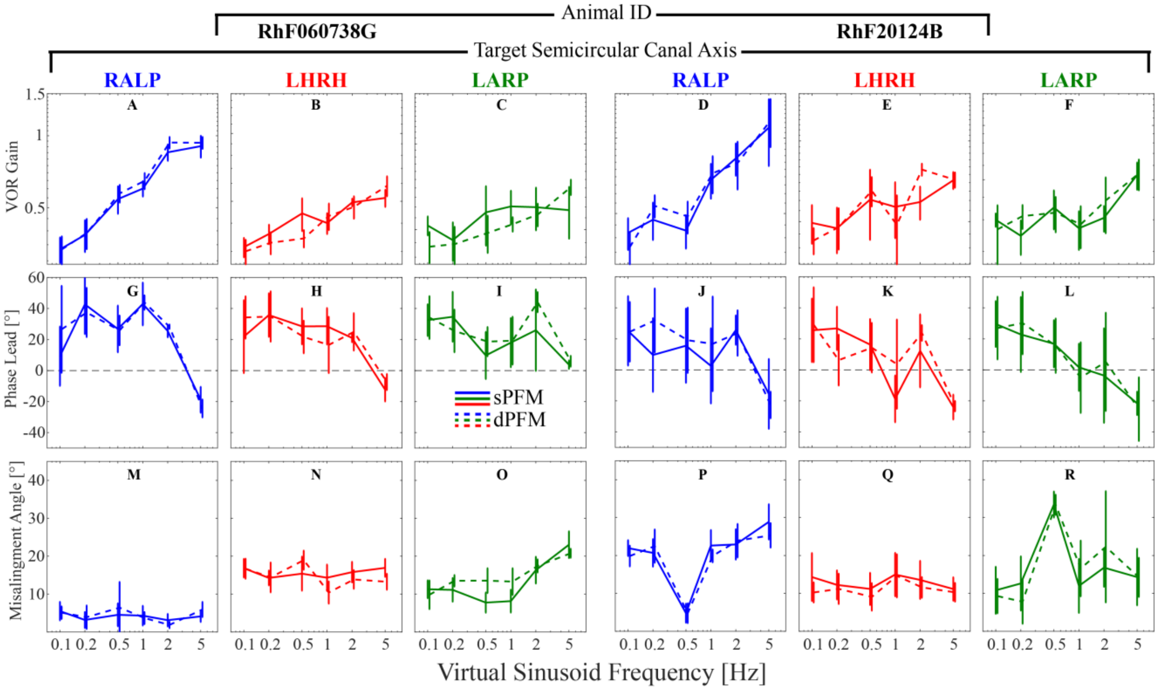

Figure 4.6: dPFM vs. sPFM frequency response summary. 3D VOR responses from both RhF060738G (**A-C**,**G-I**,**M-O**) and RhF20124B (**D-F**,**J-L**,**P-R**) were practically indistinguishable using the sPFM (solid lines) and dPFM (dashed lines) mappings. Residuals between the two mappings were not found to be significant (ART two-way repeated measures ANOVA; RALP: $F_{[1,311]} = 2.15$, $p = 0.14$; LHRH: $F_{[1,413]} = 0.70$, $p = 0.40$; LARP: $F_{[1,258]} = 1.94$, $p = 0.17$).

4.4 Discussion

Integrating signal processing strategies between VI and CI technologies may require merging VI stimulus encoding via PFM and interleaved modulation of pulse amplitude used in CIS techniques in many modern CIs. The mismatch of temporal precision necessary for smooth modulation of pulse frequency and the fixed rate used in CIS may create temporal errors for VI stimulation delivered by a hypothetical combined VI/CI inner ear implant. This study modeled such a device through the dPFM head velocity stimulus encoding mapping and compared evoked 3D VOR amplitudes in all three canals in the left ear of two rhesus macaques. Overall, our study shows that VOR magnitude, phase response, and 3D VOR misalignment are minimally affected by temporal discretization representing integration of a PFM-based VI with common CI stimulator capabilities (e.g., the MED-EL PULSAR stimulator used in this study, with a maximum overall pulse rate of 50,000pps across all output channels).

A future combined VI/CI will likely benefit from advances in both stimulation hardware capabilities and signal processing schemes that may alleviate the temporal discretization modeled in the dPFM mapping used here. For example, the PULSAR CI100 device contains the I100 electronics platform which integrates individual current sources for each stimulating electrode channel, but only a single current sink used as a reference electrode (typically routed to a metal contact on the CI stimulator housing in clinical applications, and routed to a Pt/Ir electrode implanted in the common crus in this study) [98]. While this has been sufficient for many years due to the non-overlapping coding schemes used by many CIS-based signal processing approaches to avoid current spread, modern techniques such as fine structure processing (FSP) deviate from the CIS approach to improve auditory perception. In contrast to standard CIS processing (where *fixed-rate*, interleaved pulsatile stimulation is *amplitude modulated* to encode slowly varying envelopes of band-pass filtered signals), FSP replicates the high frequency carrier rate via *modulation of pulse rate* to match fine structure frequency content with a *constant current amplitude* (similar to PFM encoding used in prototype VIs). Incorporating FSP on more apical (i.e., low frequency) CI electrodes with traditional CIS-like schemes on higher frequency channels has been successful in encoding information critical for complex auditory percepts such as pitch and timbre [99–101]. Strategies like FSP further complicate the simplified assumptions used in this study, breaking the non-overlapping channel stimulation assumption used to generate the dPFM mapping.

With independent current source/sinks and strategies that may alleviate current spread issues, the average per-channel stimulation rate may be much greater than assumed in this study. This makes our dPFM model a liberal estimate of potential temporal discretization effects, and in reality distortions experienced in PFM stimulation should be lower. The results of this study indicate that the potentially superfluous levels of modulation errors used in our dPFM mapping do not have a significant effect on PFM encoding of both angular head velocity amplitude or frequency response characteristics, thus demonstrating future implementations may not need to consider its effects for a combined VI/CI device.

While these data indicate dPFM has no measureable effect on 3D electrically-evoked VOR performance, it is not clear if the jagged PFM steps seen at high amplitude head velocities and/or low frequency stimuli have any noticeable perceptual differences with the sPFM mapping. In other words, while response dynamics and filtering characteristics of central VOR neuronal circuits may effectively ‘smooth’ evoked compensatory VOR responses, the user of a potential combined VI/CI device may notice a decrease in head motion sensation quality and comfort using the mapping. Since the stimulator/receiver component of the Labyrinth Devices MVI™ System used in Chapter 2 and Chapter 3 of this dissertation is a modified MED-EL CONCERTO implant (which is compatible with the RIB/MAX stimulation software used in the dPFM study), it would be possible to replicate this study and quantify the perceptual differences between each mapping with the MVI™ system.

Additionally, further studies investigating VI coding at the periphery using single unit electrophysiology may shed light on how activation of primary vestibular neurons encode dPFM style modulation waveforms. It would be valuable to understand how dynamic PFM waveforms are encoded in primary afferents to infer what level of discretization is transmitted to later stages in VOR processing. Furthermore, quantifying a vestibular peripheral equivalent of a “flicker fusion frequency” in terms of a minimal quantization error that is represented in both evoked neuronal firing rates of primary afferents and subject perception may help dictate the required temporal resolution for future VI technology.

Chapter 5 Conclusions and Future Directions

5.1 Implications and Limitations

The work presented in this dissertation describes the first efforts towards assaying 3D eye movement responses to electrical stimulation of vestibular afferents in humans. The directionally appropriate, monotonically controlled, and mostly conjugate eye movement responses evoked in this study support use of the MVI™ system as a treatment for BVH. Additionally, this work has shown that continuous, motion-modulated electrical stimulation produces stable eye movement responses after sustained use, providing primary evidence that this device is safe and effective.

Unlike cochlear implants, the MVI™ uses a non-zero rate/current stimulus as a set-point to pulse-rate- or pulse-amplitude-modulate prosthetic stimulation to encode head motions. While this enables a unilaterally implanted prosthesis to encode both excitatory and inhibitory head motion, it requires the individual receiving the device to acclimate to tonic stimulation on three active electrodes. The time course of adaptation and overall subject comfort with stimulation onset will be important to assay whether vestibular implantation activation can be an outpatient procedure and will not require overnight hospital observation. For example, had subjects responded similarly to individuals *losing* vestibular tone, the onset of MVI™ could be debilitating and require an overnight, observed stay in a hospital setting. In contrast, our results show that all four subjects produced a robust nystagmus that decayed to subthreshold levels in under 35 minutes and were able to walk around the clinical space without assistance. Each subject went to their hotel room the night of activation without any adverse events.

This study was organized as a nonrandomized, self-controlled early feasibility study designed to assess the safety and tolerability of the MVI™ system. To this end, we had to balance optimization of subject outcomes via stimulus parameter adjustments and our scientific goals of studying adaptation to prosthetic vestibular stimulation. This allowed us to make modifications to current levels, pulse rates, and additions/subtractions of current/rate modulation techniques to optimize performance. While this permitted us to interact directly with each subject to improve their day-to-day life with our device, it prevented us from employing a uniform set of stimulation parameters that would have facilitated aggregation of data across subjects and over time. Our data do provide observations of VOR performance over long stretches of continuous stimulation without any changes to device parameters that may provide information on central adaptation dynamics.

5.2 Future directions

The results described in this dissertation are a significant step in assessing the safety and efficacy of the MVI™ System. While the data presented here from 4 human subjects produced many similarities; overall angular eye velocity magnitudes, response alignment, and disconjugacy between the two eyes differed between each subject. Enrolling and implanting more subjects will provide a more complete picture of the distribution of responses in the BVH patient population to MVI™ stimulation.

For subject MVI004, initial electrode characterization revealed that electrodes implanted in the left horizontal canal produced a mixed 3D angular VOR response consistent with co-activation of the left horizontal and left anterior ampullary nerve branches. Unlike experiments in animals where continuous motion-modulated electrical stimulation produced cross-axis adaptation changes to 3D alignment [33,37], longitudinal data from MVI004 revealed that the misalignment persisted through 140 days post-activation. We hypothesize that the addition of pulse-amplitude-modulation may have precluded the central adaptation seen in those studies. Future work systematically assessing cross-axis adaptation using modulation of both pulse amplitude and rate may reveal the reason for this discrepancy.

The studies presented here are focused on evoked 3D eye movement responses to prosthetic stimulation of primary vestibular afferents. Advancing this work in humans provides a unique opportunity to quantify perceptual responses to the range of stimuli presented here. Determining stimulus detection thresholds in a rigorous, repeatable manner will allow a direct assessment of individual subject performance and comparisons at different phase durations. Also, quantifying the pulse-frequency- and pulse-amplitude-modulation discretization thresholds, below which there is no perceptual impact, could help optimize stimulus parameter requirements for a future vestibular prosthesis.

5.3 Conclusions

This dissertation outlines the results of the first-in-human clinical trial of a vestibular implant aimed at providing continuous, motion-modulated electrical stimulation of primary vestibular afferents to treat profound BVH. We have shown that MVI™ stimulation can evoke 3D eye movements that rotate about axes approximate the anatomic canal axes. Stimulation of electrodes in all three implanted canals of all four human subject enrolled in this study produced reflexive eye movements consistent with excitation of individual canals in the implanted ear. Additionally, initial onset of a tonic, constant rate/current pulse rate in each canal produced a nystagmus that subsided below 5°/s within 30 minutes in all dimensions.

After continuous use with motion-modulated input, MVI™ produces stable, canal specific eye movements. We also showed that stimulation of electrodes in different canals generated eye movements approximating the vector sum of individual canal anatomic axes. During mechanical rotations, trials with gyroscopic modulation turned on produced significantly larger eye movements than with tonic stimulation and modulation turned off.

Finally, investigating temporal discretization of PFM-based stimulation produced a minimal effect on the evoked 3D angular VOR gain, phase, and misalignment. This result indicates that a potential combined VI/CI could operate with minimal changes to existing CI stimulation strategies. Overall, this work is provides data that vestibular implant technology is a safe, tolerable, and effective restorative therapies for individuals suffering from severe loss of balance sensation.

Chapter 6 Appendix

6.1 MVI™ Electrode Characterization Thresholds

Before MVI™ device activation, all 9 stimulating electrodes were tested to determine a range of effective, yet safe current amplitudes to thoroughly assay VOR responses to electrode characterization. Thresholding experiments used pulse trains modulated at 200pps for 200ms and 0pps for 300ms to find current amplitudes that elicited appropriate VOR responses, subject perceptions, and avoided discomfort for each phase duration offered by the MVI™ stimulator (50, 100, 200, and occasionally 300µs/phase). All experiments were done with the subject in darkness using the 3DBinoc™ goggles recording eye movements (as described in section 2.2.5) with IR pass filter insets. Subjects typically stayed on a bite-block to stabilize their head during testing, but were free to come off between stimuli to communicate with the study team. Current amplitudes started at 0µA and increased with 50µA increments to determine each threshold. These thresholds were not acquired via psychophysical techniques, but rather via direct assessments of subject tolerance and sensation to assay safe stimulation ranges. Experiments revealed four thresholds used to characterize each electrode/phase duration pair:

- T_P = Perceptual threshold, which subjects verbally reported when they felt a motion percept.
- T_V = VOR threshold, determined online by study team members. Current amplitudes slightly below this level were used as the minimum current amplitude for electrode characterization experiments (sections 2.2.7, and 2.3.1).
- T_M = Maximum tolerable threshold, or the maximum current amplitude that avoided facial twitching, shifts in motion percepts, pain, or auditory percepts. This level corresponds to the maximum current amplitude tested during electrode characterization (sections 2.2.7, and 2.3.1).
- T_S = Stop condition, where any pain, auditory, facial, or non-ampullary nerve afferent sensation was reported.

The MVI™ stimulator was designed to deliver a maximum current amplitude of 700µA for all phase durations to adhere to safe charge injection limits. Thus, $T_M$was occasionally set to 700µA if the threshold finding experiment did not reveal a T_S condition after testing all available current levels. MVI001 was only thoroughly tested using electrodes E3, E7, and E11 due to time constraints. In some cases, the 300µs/phase condition was skipped due to subject preference and high likelihood of clashes during sequential pulse delivery in the activated state due to the longer phase duration.

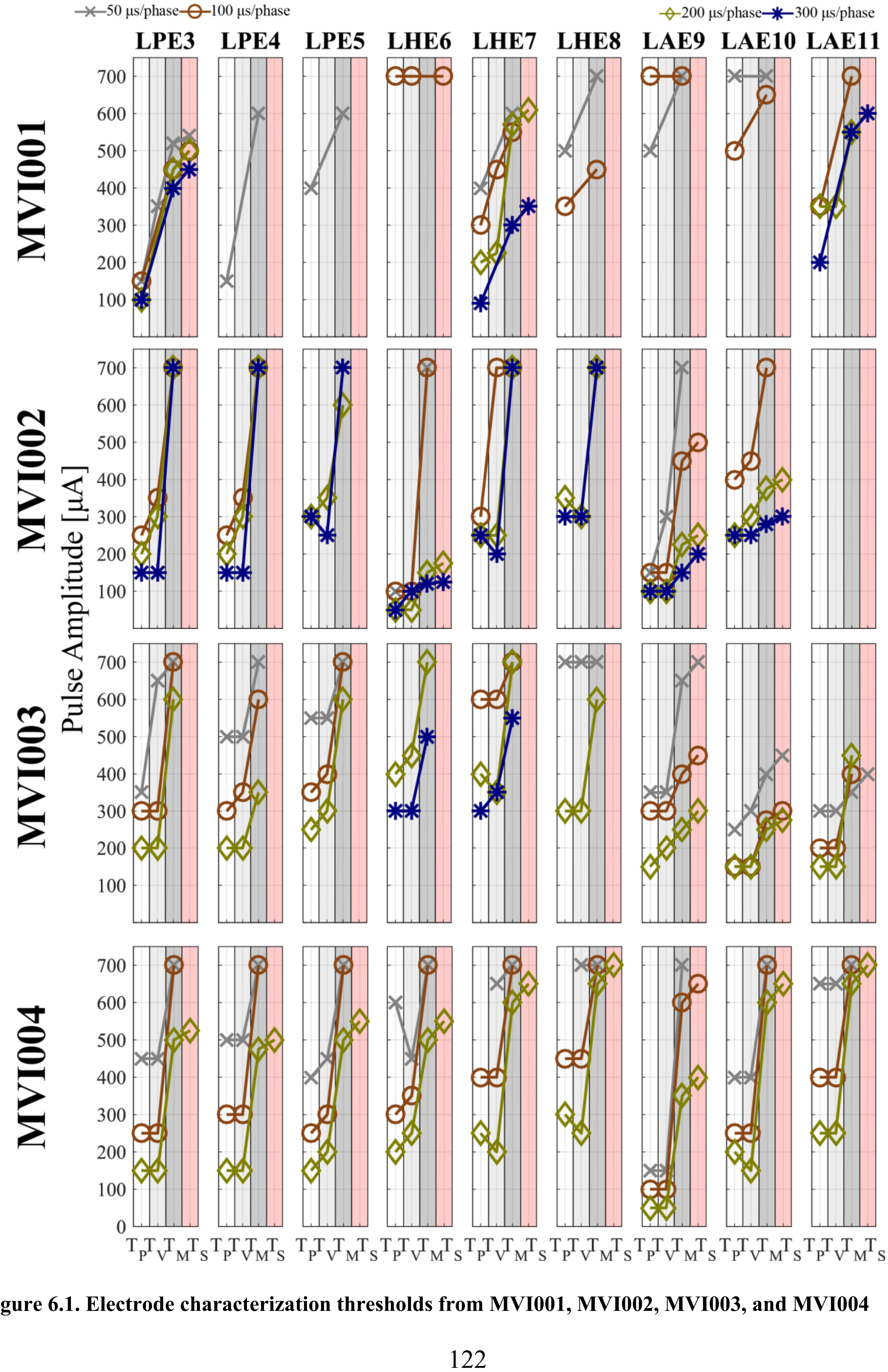

Figure 6.1. Electrode characterization thresholds from MVI001, MVI002, MVI003, and MVI004

6.2 Labyrinth Devices 3DBinoc™ Noise Floor Example

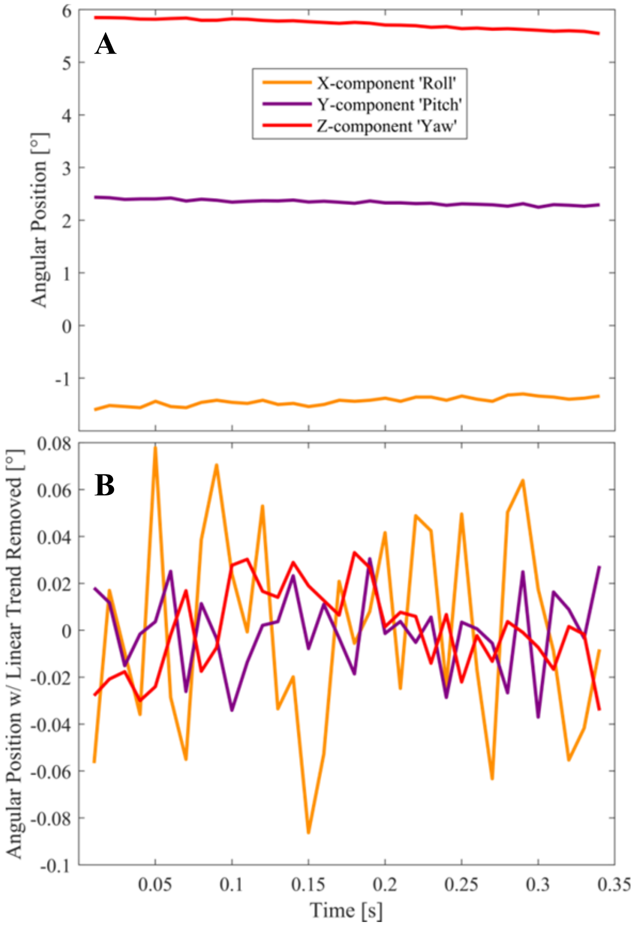

Figure 6.2. Labyrinth Devices 3DBinoc™ Goggles noise floor example. Data collected from the right eye of subject MVI004 pre-operatively during head impulse testing. In this brief segment (**A**), the subject was fixated on an Earth-fixed target in light, free from any re-fixation saccades before a head impulse occured. (**B**) Fitting each 3D component with a least squares linear model (that was subsequently removed in B) to eliminate any offset or slope revealed peak-to-peak noise floors of 0.18, 0.07, and 0.06° for the X, Y, and Z components, respectively.

6.3 Example of low binocular disconjugacy in a normal subject during LARP head movements assayed using the 3DBinoc™ goggles

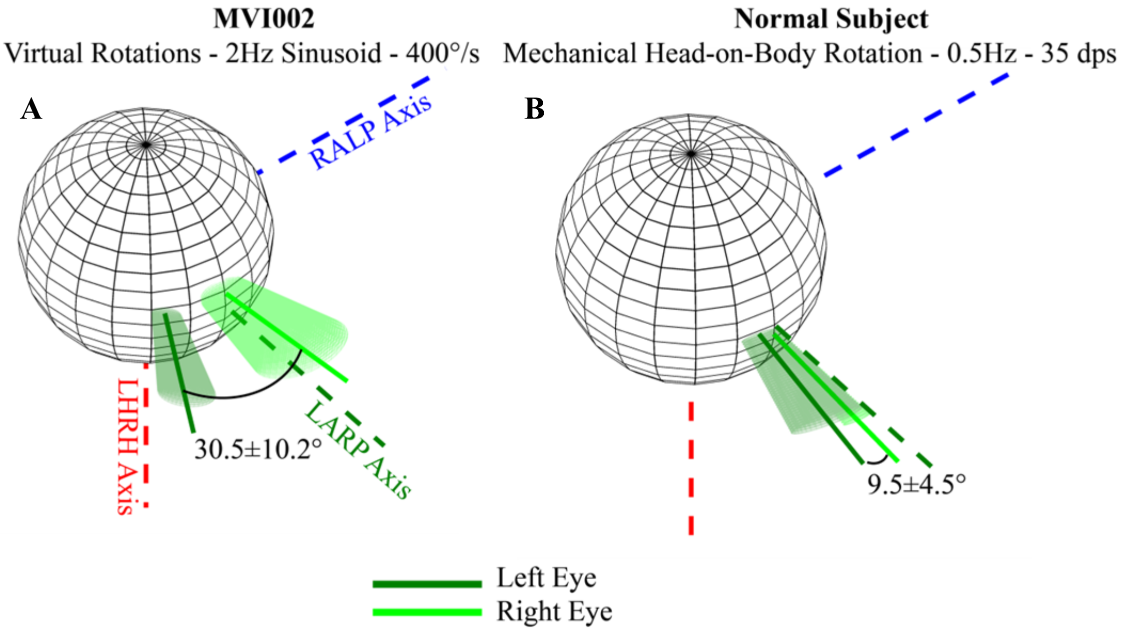

Figure 6.3. Binocular disconjugacy seen in MVI002 compared to data from a normal subject acquired with the 3DBinoc™ goggle set. To rule out if the binocular disconjugacy seen in subject MVI002 when assaying electrodes in both the left anterior canal and left posterior canal both pre-activation (Figure 2.6) and after 8 weeks of continuous stimulation (Figure 3.4, response to 100% modulation depth LARP stimulation shown in **A**) was a VOG data acquisition artifact, (**B**) we recorded 3D VOR responses in a normal subject during head-on-body 0.5Hz sinusoidal at 35°/s peak head velocity. The large disconjugacy between the left and right eyes axes of rotation seen in subject MVI002 during virtual sinusoids at peak modulation depth (30.5±10.2°) was significantly different from the low misalignment seen in a normal subject (9.5±4.5°) when tested using a Wilcoxon ranked sum test ($Z = 2.77$, $p < 0.01$).

6.4 Change in misalignment after adding co-modulation

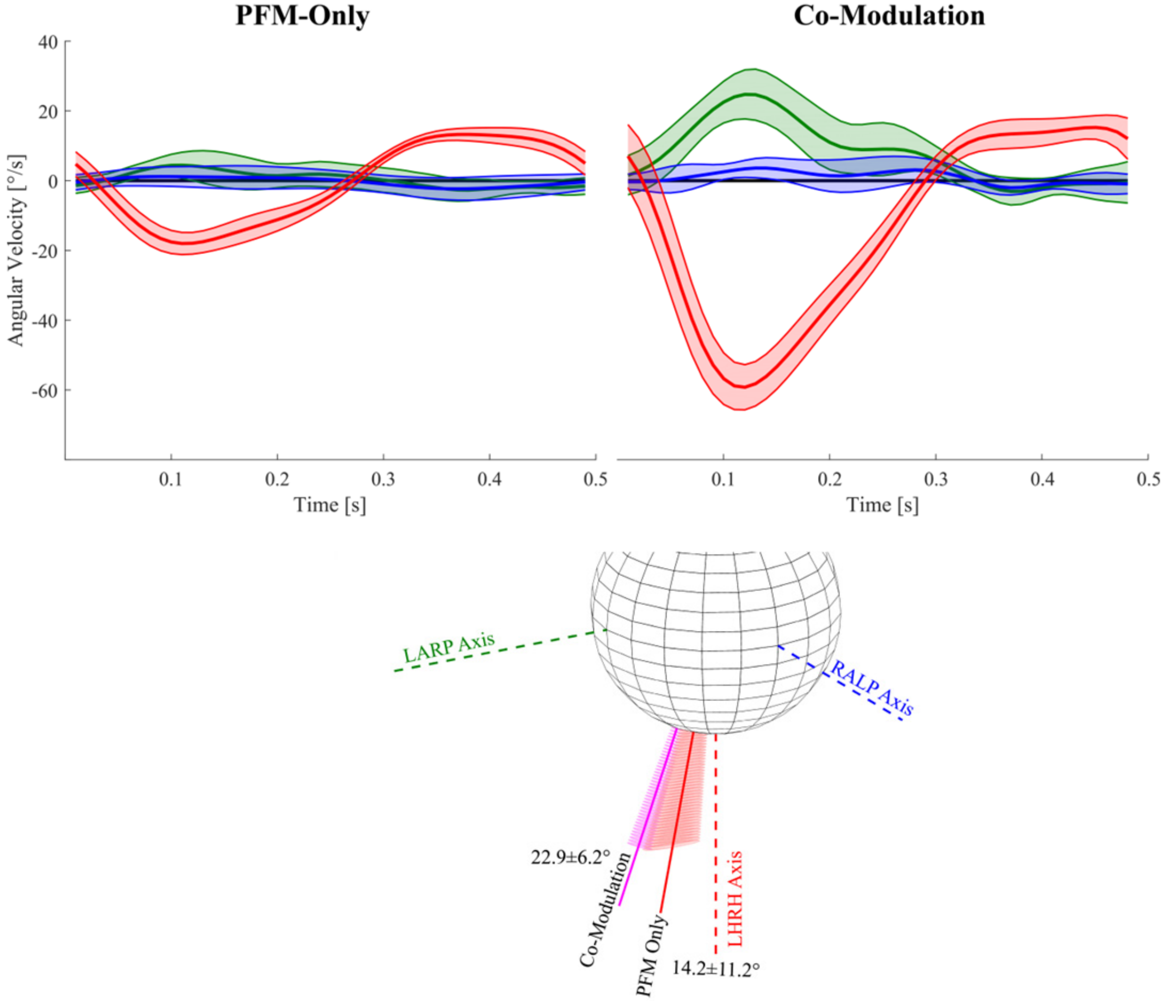

Figure 6.4. Increase in response misalignment after adding amplitude modulation. After 42 days of motion-modulation with a pulse-rate-modulation map only (**A**, cycle averaged 3D responses assayed while testing 100% modulation depth 2Hz sinusoids delivered to electrode E6 in the horizontal canal), we added amplitude modulation to all three channels of subject MVI002 and assayed responses during the same day (**B**, same head velocity waveform as A). Amplitude of the evoked response grew from ~20 to ~60°/s, while misalignment grew from ~14 to ~23°. The increase in misalignment with the anatomic LHRH axis was significant (Wilcoxon rank sum test: Z = 2.15, $p < 0.05$)

6.5 Full Timeline of MVI™ Device Parameter Changes

After determining the optimal set of MVI™ stimulation parameters (including the electrode contact within a specific canal electrode shank, phase duration, and baseline current amplitude) from electrode characterization experiments (section 2.3.1), each subject was activated to a baseline pulse rate of 100pps (section 2.3.2). Baseline pulse rates for subjects MVI002, MVI003, and MVI004 were subsequently increased to 150pps. Following the initial activation day, the MVI™ study team followed an intent-to-treat strategy to optimize each subject's performance by individually adjusting stimulation parameters based upon eeVOR performance, rotary chair testing, and subject reports. The time course of the MVI parameter set for each subject and each canal axis are outlined in Table 6.1. Mapping type definitions are described in section 3.2.1, with the numbered mapping headers color coded for comparison to labels in data figures presented in section 0.

Implant Ear	Left	Subject ID	MVI001				MVI002			MVI003		MVI004		
		Parameter Value	**Mapping #1**	**Mapping #2**	**Mapping #3**	**Mapping #4**	**Mapping #1**	**Mapping #2**	**Mapping #3**	**Mapping #1**	**Mapping #2**	**Mapping #1**	**Mapping #2**	**Mapping #3**
		Date	09/07/2016	09/12/2016	10/19/2016	1/18/2017	11/30/2016	12/02/2016	1/11/2017	02/23/2017	03/08/2017	01/05/2018	01/09/2018	02/16/2018
		Days Since MVI™ Activation	0	5	42	133	0	2	42	0	13	0	4	42
RALP		Electrode ID	E3	E3	E3	E3	E3	E3	E3	E3	E3	E3	E3	E3
		Phase Dur. [us/phase]	50	200	200	200	100	100	100	200	200	200	200	200
	Amp. Mod.	Map Type	Flat	Flat	Flat	Flat	Flat	Flat	Piecewise Linear	Flat	Flat	Piecewise Linear	Piecewise Linear	Piecewise Linear
		Min. Pulse Amp. [uA]	N/A	N/A	N/A	N/A	N/A	N/A	500	N/A	N/A	125	125	125
		Baseline Pulse Amp. [uA]	390	450	450	450	600	600	600	600	600	406	406	406
		Max Pulse Amp. [uA]	N/A	N/A	N/A	N/A	N/A	N/A	700	N/A	N/A	500	500	500
		Compression Factor	N/A	N/A	N/A	N/A	N/A	N/A	N/A	N/A	N/A	N/A	N/A	N/A
	Rate Mod.	Map Type	Sigmoidal	Sigmoidal	Sigmoidal	Sigmoidal	Sigmoidal	Sigmoidal	Sigmoidal	Sigmoidal	Sigmoidal	Sigmoidal	Sigmoidal	Sigmoidal
		Min. PR [pps]	0	0	0	0	0	0	0	0	0	0	0	0
		Baseline PR [pps]	100	100	100	100	150	150	150	150	150	150	150	150
		Max PR [pps]	400	400	400	400	450	450	450	450	450	450	450	450
		Compression Factor	2	2	2	5	5	5	5	2	2	5	5	5
LHRH		Electrode ID	E7	E7	E7	E7	E6	E6	E6	E6	E6	E6	E6	E6
		Phase Dur. [us/phase]	200	200	200	200	100	100	100	200	200	200	200	200
	Amp. Mod.	Map Type	Flat	Flat	Flat	Flat	Flat	Flat	Piecewise Linear	Flat	Sigmoidal	Sigmoidal	Sigmoidal	Sigmoidal
		Min. Pulse Amp. [uA]	N/A	N/A	N/A	N/A	N/A	N/A	150	N/A	610	220	220	220
		Baseline Pulse Amp. [uA]	570	700	600	600	160	350	350	620	620	320	320	320
		Max Pulse Amp. [uA]	N/A	N/A	N/A	N/A	N/A	N/A	550	N/A	700	500	500	470
		Compression Factor	N/A	N/A	N/A	N/A	N/A	N/A	N/A	N/A	20	20	4	3
	Rate Mod.	Map Type	Sigmoidal	Sigmoidal	Sigmoidal	Sigmoidal	Sigmoidal	Sigmoidal	Sigmoidal	Sigmoidal	Sigmoidal	Sigmoidal	Sigmoidal	Sigmoidal
		Min. PR [pps]	0	0	0	0	0	0	0	0	0	0	0	0
		Baseline PR [pps]	100	100	100	100	150	150	150	150	150	150	150	150
		Max PR [pps]	400	400	400	400	450	450	450	450	450	450	450	450
		Compression Factor	2	2	2	2	5	5	5	2	2	5	5	5
LARP		Electrode ID	E11	E11	E11	E11	E9	E9	E9	E9	E9	E11	E11	E11
		Phase Dur. [us/phase]	200	200	200	200	100	100	100	100	100	200	200	200
	Amp. Mod.	Map Type	Flat	Flat	Flat	Flat	Flat	Flat	Piecewise Linear	Flat	Sigmoidal	Piecewise Linear	Piecewise Linear	Piecewise Linear
		Min. Pulse Amp. [uA]	N/A	N/A	N/A	N/A	N/A	N/A	500	N/A	400	220	220	220
		Baseline Pulse Amp. [uA]	480	700	700	700	600	600	600	400	400	550	550	550
		Max Pulse Amp. [uA]	N/A	N/A	N/A	N/A	N/A	N/A	700	N/A	420	600	600	600
		Compression Factor	N/A	N/A	N/A	N/A	N/A	N/A	N/A	N/A	20	N/A	N/A	N/A
	Rate Mod.	Map Type	Sigmoidal	Sigmoidal	Sigmoidal	Sigmoidal	Sigmoidal	Sigmoidal	Sigmoidal	Sigmoidal	Sigmoidal	Sigmoidal	Sigmoidal	Sigmoidal
		Min. PR [pps]	0	0	0	0	0	0	0	0	0	0	0	0
		Baseline PR [pps]	100	100	100	100	150	150	150	150	150	150	150	150
		Max PR [pps]	400	400	400	400	450	450	450	450	450	450	450	450
		Compression Factor	2	2	2	2	5	5	5	2	2	5	5	5

Table 6.1. Timeline of MVI™ device parameter settings for all subjects.

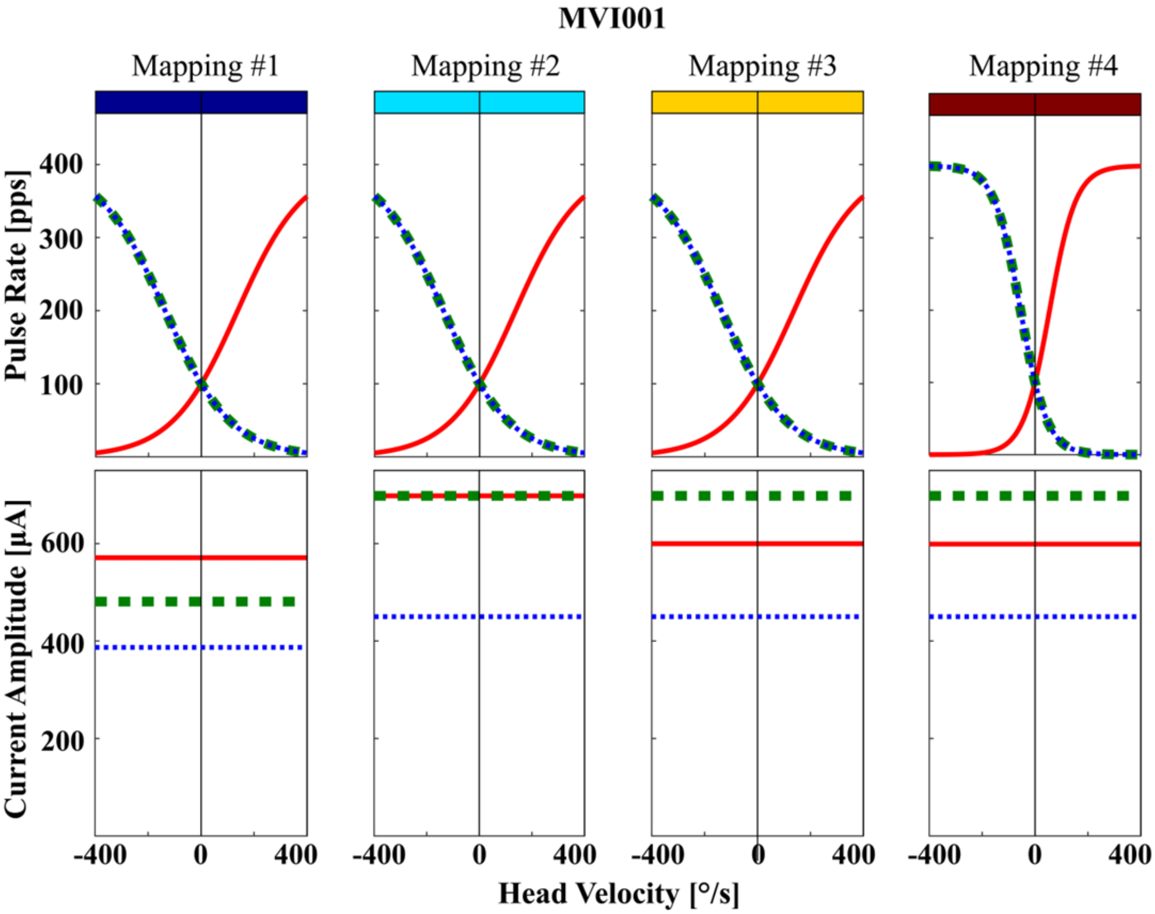

Figure 6.5. Subject MVI001 longitudinal pulse rate and pulse amplitude mappings. Graphical representation of stimulus parameters describing head velocity-to-pulse rate and –pulse amplitude for each active electrode in all 3 canals throughout the period of continuous, motion-modualted electrical stimulation. This subjects was adapted to a 100pps baseline stimulation rate that was unchanged throughout the continuous stimulation period. Rate modulation mappings remained constant until 133 days post activation, where the compression factor for all 3 canals was increased from 2 to 5 in order to boost responses to head velocities at lower head velocities. Following activation (Mapping #1), the study team increased the current amplitude on all channels and increased the phase duration of the biphasic pulses delivered to the left posterior canal from 50 to 200 µs/phase (Mapping #2). The subject subsequently reported discomfort when turning his head to the left, and the current amplitude was decreased from ~700 to ~600µA.

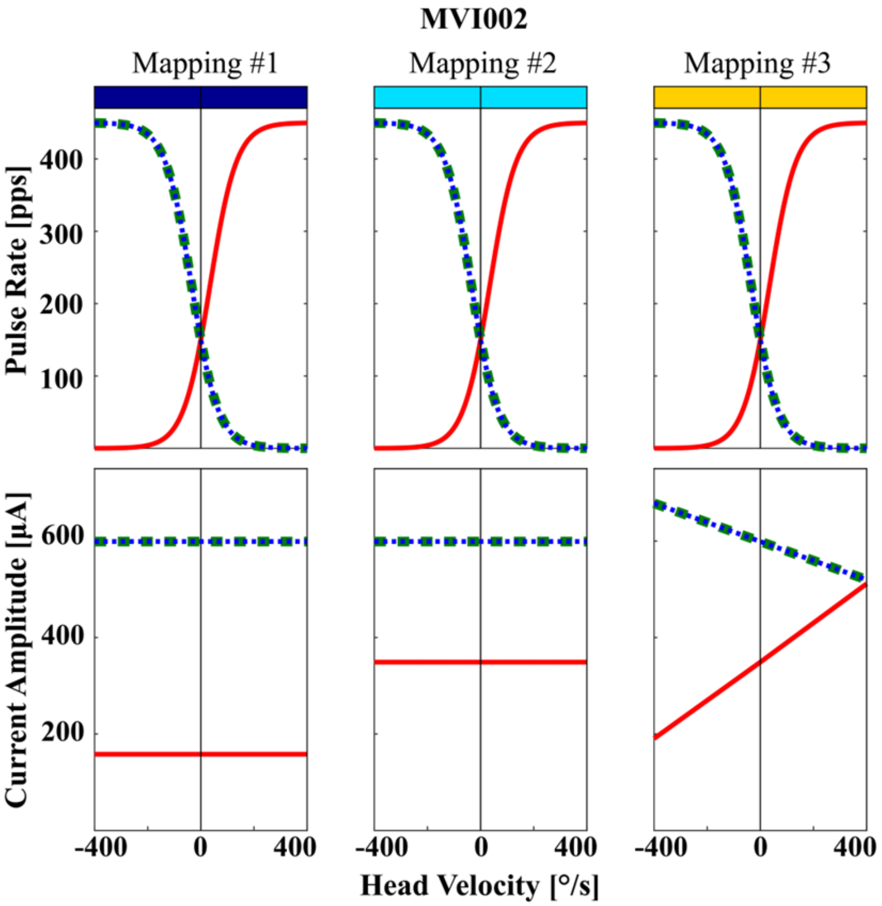

Figure 6.6. Subject MVI002 longitudinal pulse rate and pulse amplitude mappings. Graphical representation of stimulus parameters describing head velocity-to-pulse rate and –pulse amplitude for each active electrode in all 3 canals throughout the period of continuous, motion-modualted electrical stimulation. This subject was first adapted to a 100pps baseline stimulation rate on all canal electrodes, which was increased to 150pps the same day (Mapping #1). Following activation, rate modulation parameters were unchanged throughout the period of continuous stimulation. After two days of continuous stimultion, the current amplitude of the horizontal channel was increased to optimize responses to isolated horizontal canal stimulation. An amplitude modualtion mapping that spanned the threshold and maximum tolerable current level was added 42 days after device activation (Mapping #3).

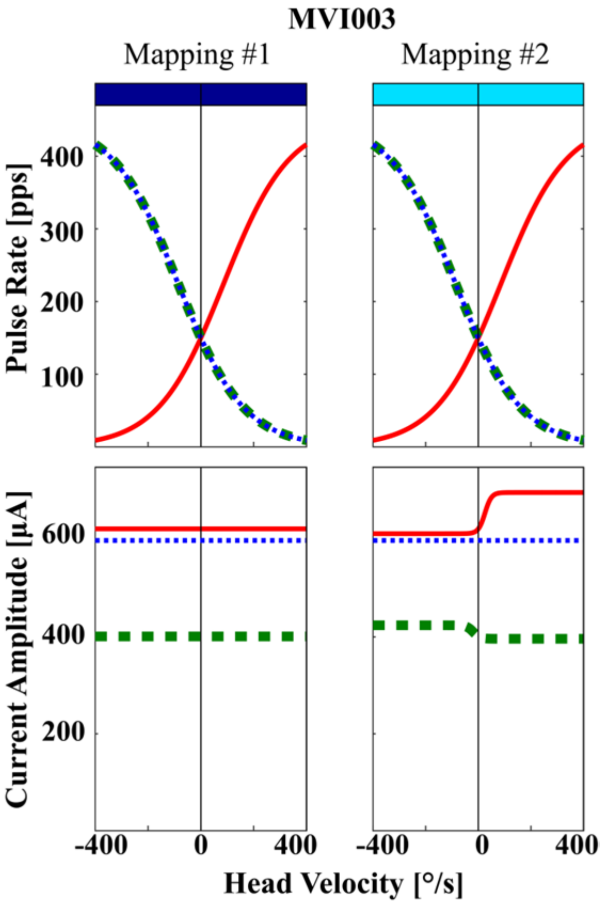

Figure 6.7. Subject MVI003 longitudinal pulse rate and pulse amplitude mappings. Graphical representation of stimulus parameters describing head velocity-to-pulse rate and –pulse amplitude for each active electrode in all 3 canals throughout the period of continuous, motion-modualted electrical stimulation. This subject was first adapted to a 100pps baseline stimulation rate on all canal electrodes, which was increased to 150pps the same day (Mapping #1). Rate modulation parameters remained constant with a compression factor of 2. After 13 days of continuous stimulation, an amplitude modulation mapping was added to stimulus mappings for the left horizontal and left anterior canal branches. This mapping did not change current ampitude for inhibitory head motions, but insteadrapidly increased from the baseline current amplitude to the maximum tolerble current found during eletrode characterization.

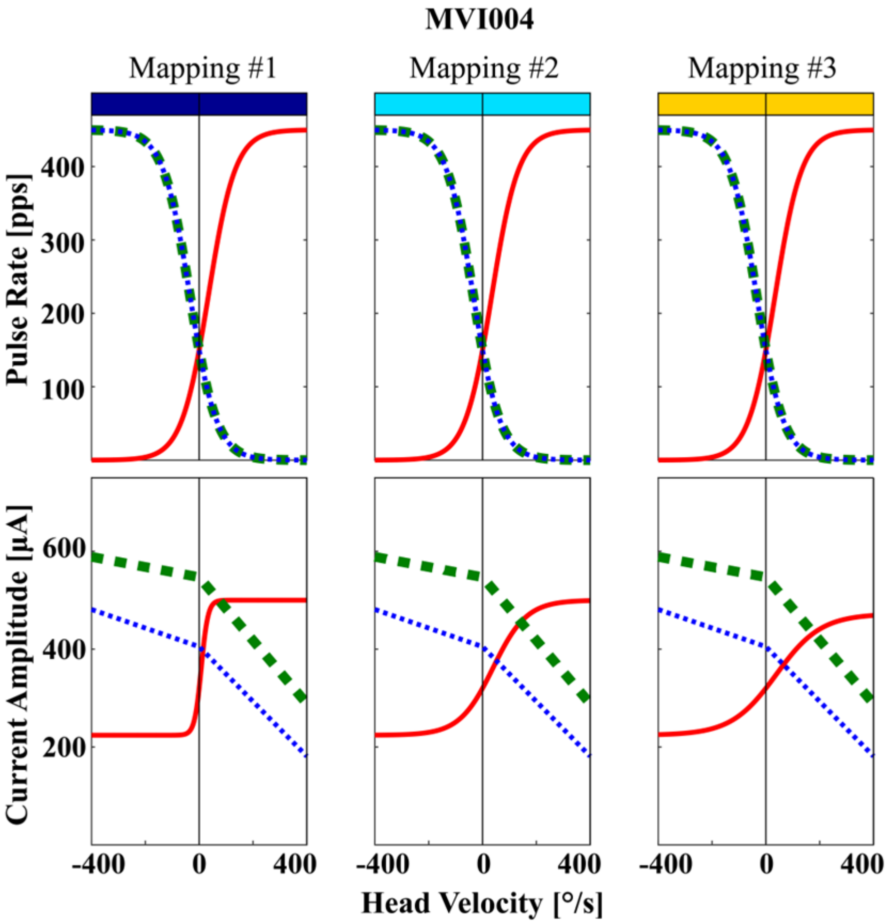

Figure 6.8. Subject MVI004 longitudinal pulse rate and pulse amplitude mappings. Graphical representation of stimulus parameters describing head velocity-to-pulse rate and –pulse amplitude for each active electrode in all 3 canals throughout the period of continuous, motion-modualted electrical stimulation. This subject was first adapted to a 100pps baseline stimulation rate on all canal electrodes, which was increased to 150pps the same day (Mapping #1). Rate modualtion parameters for all channels remained constant with a compression factor of 5. This subject was activated with an amplitude modulation mapping set for all 3 canal channels. The steep (compression factor of 20) slope of the amplitude modulation channel set for the left horizontal canal was decreased to 4 (Mapping #2) and later 3 (Mapping #3) to reduce discomfort reported by the subject.

6.6 Complete longitudinal MVI™ responses

This section presents longitudinal, visit-by-visit VOR responses from all 4 subjects for up to ~300 (MVI001 and MVI002) or ~160 days (MVI003 and MVI004) post-MVI™

device activation. During this time, each subject received continuous, 24 hours/day motion-modulated electrical stimulation designed to encode head rotation components about each subject's anatomic canal axes. Data are presented for trials assaying responses to (section 6.6.1) *virtual* 2Hz sinusoidal amplitude sweeps from 20-400°/s delivered to each active canal electrode (presented as sweeps from 5-100% modulation depth), (section 6.6.2) *virtual* 100°/s sinusoidal frequency sweeps from 0.1-2Hz delivered to each canal active electrode, and (section 6.6.3) *mechanical* 100°/s sinusoidal rotations from 0.1-2Hz about the anatomic LHRH axis using a rotary chair in both the "Modulation ON" and "Modulation OFF" conditions (section 3.2.3).

Each figure presents the following VOR metrics:

- Peak Eye Velocity = Binocular VOR amplitudes for each 3D component, determined at the peak response for the intended 3D component.
- VOR Gain = Binocular VOR gain for the target canal component (for sections 6.6.2 and 6.6.3).
- Phase Lead = Sinusoidal phase lead, where a positive value is defined as the peak eye velocity leading the inverse of the head motion trace.
- Misalignment angle = Angle between the mean VOR axis of rotation and the ideal anatomic canal axis, computed for each eye separately.
- Binocular disconjugacy = Angle between mean axes of rotation of the left and right eye.
- Gain asymmetry = $\left(\frac{(G_E - G_I)}{(G_E + G_I)}\right)$, where G_E is the target 3D canal component excitatory VOR gain and G_I is the inhibitory gain. Each eye is plotted separately.

VOR magnitudes below 1.5°/s were too small to accurately estimate response phase lead, misalignment, disconjugacy, or gain asymmetry and were not computed for the figures below.

6.6.1 2Hz Virtual Amplitude Sweep

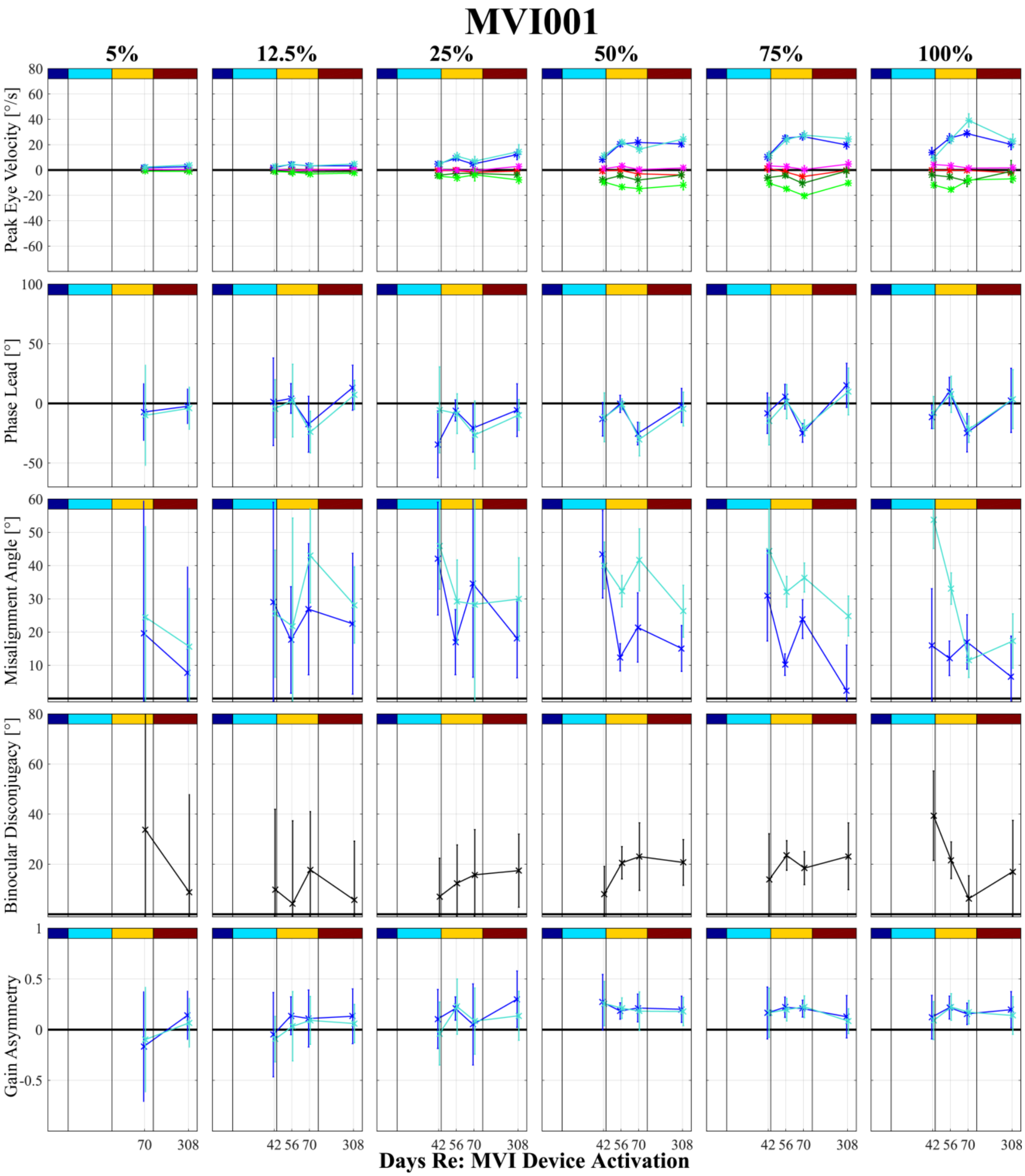

Figure 6.9. MVI001: LPE3: Longitudinal 2Hz virtual amplitude sweep.

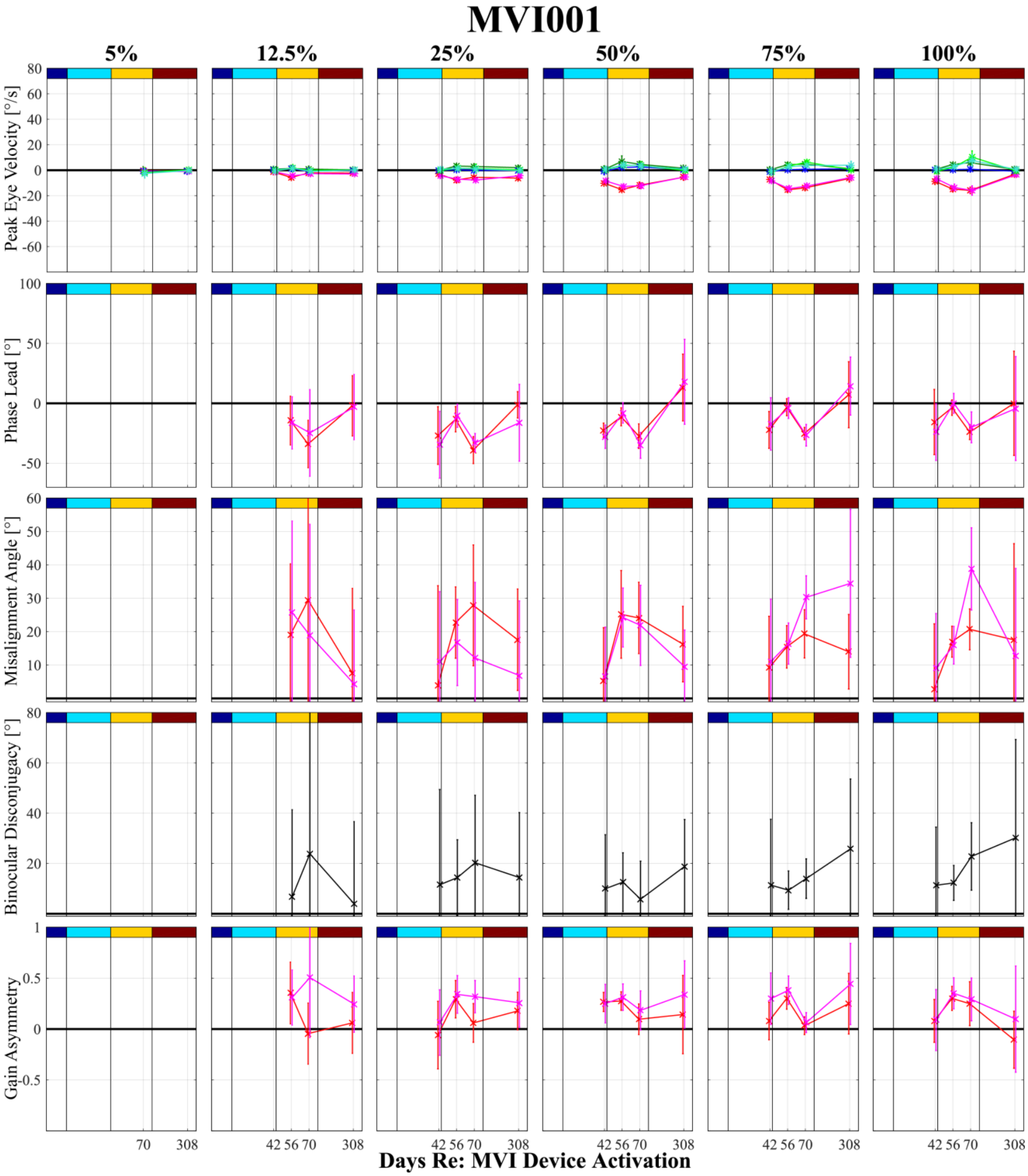

Figure 6.10. MVI001: LHE7: Longitudinal 2Hz virtual amplitude sweep.

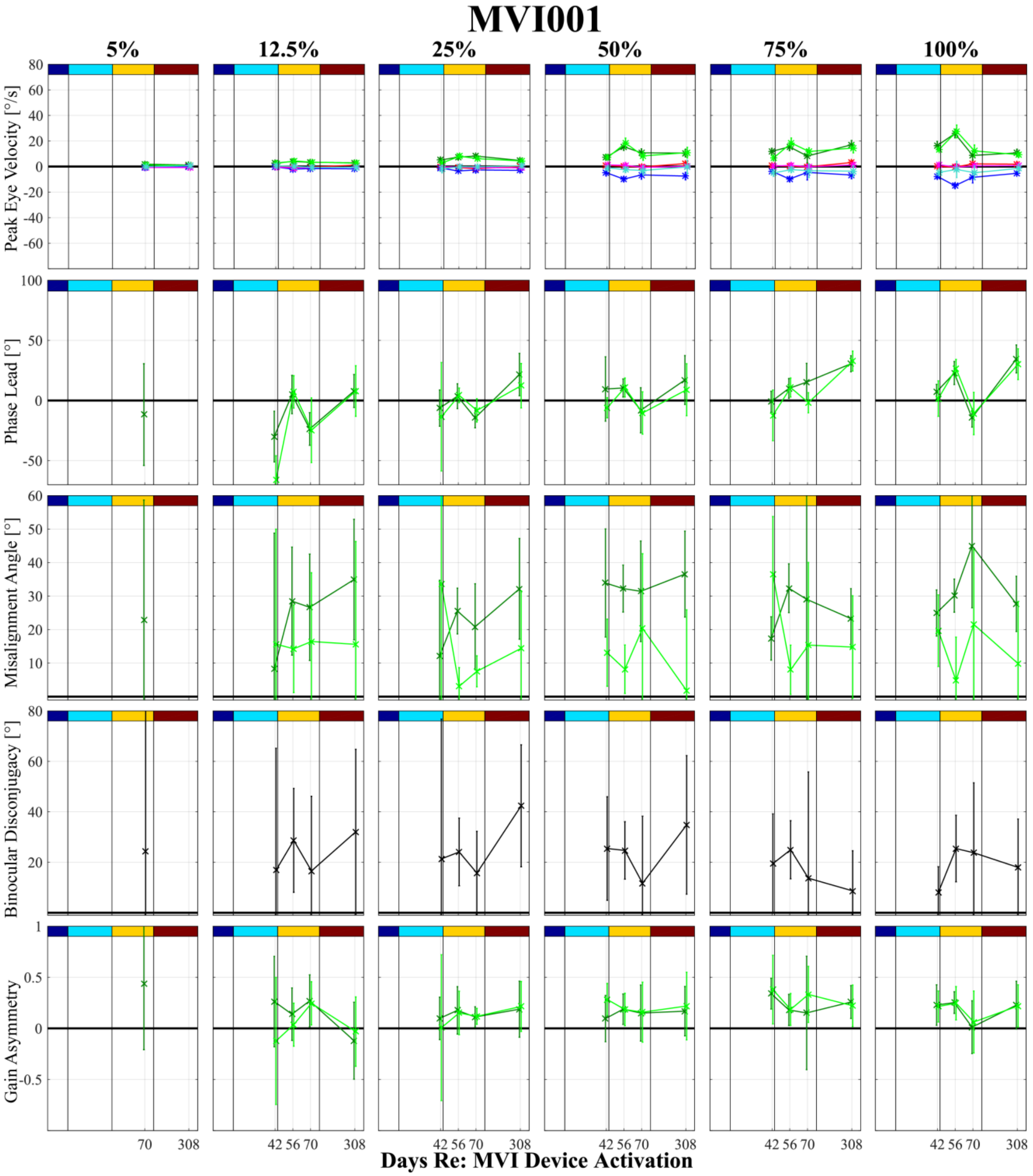

Figure 6.11. MVI001: LAE11: Longitudinal 2Hz virtual amplitude sweep.

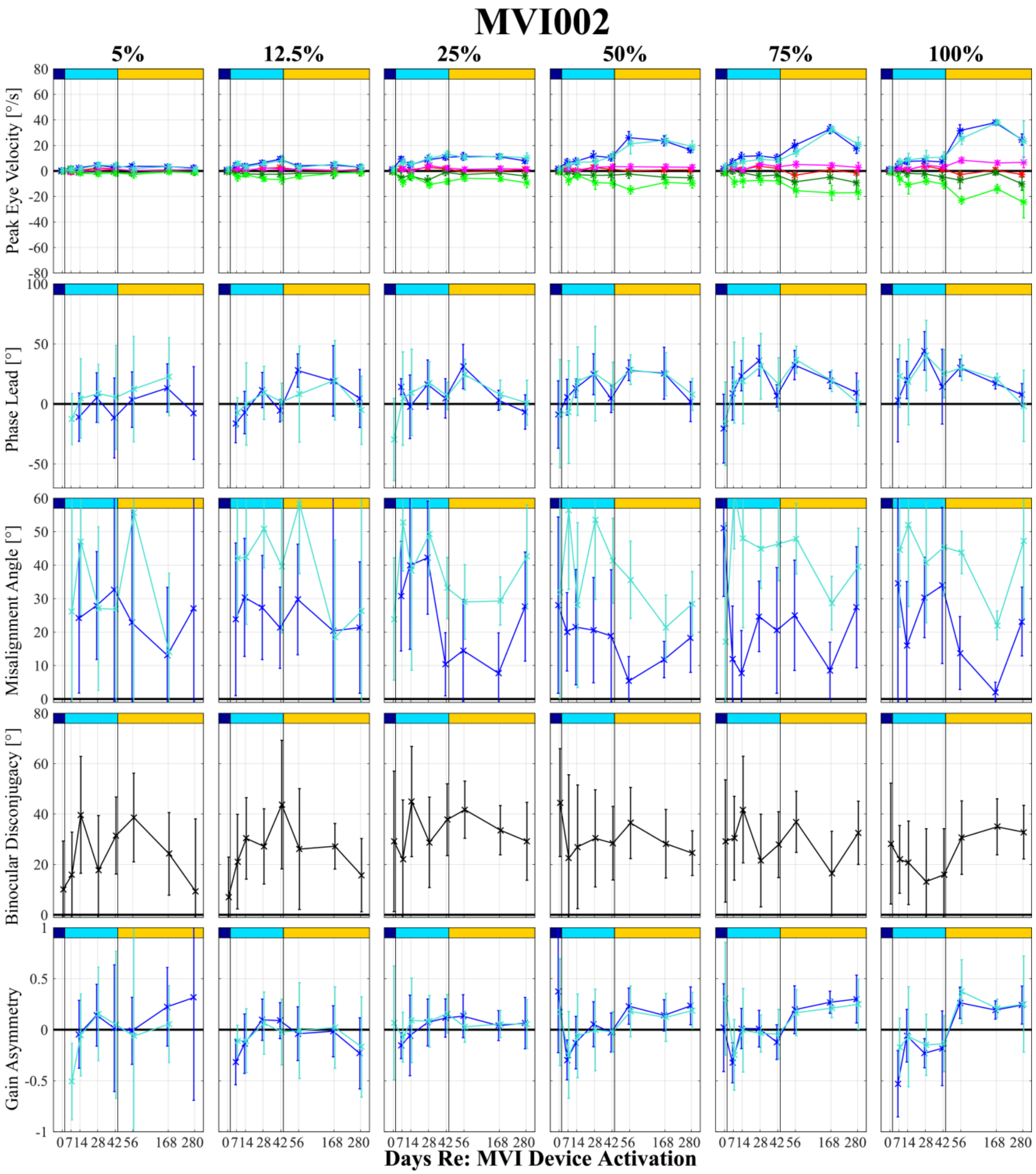

Figure 6.12. MVI002: LPE3: Longitudinal 2Hz virtual amplitude sweep.

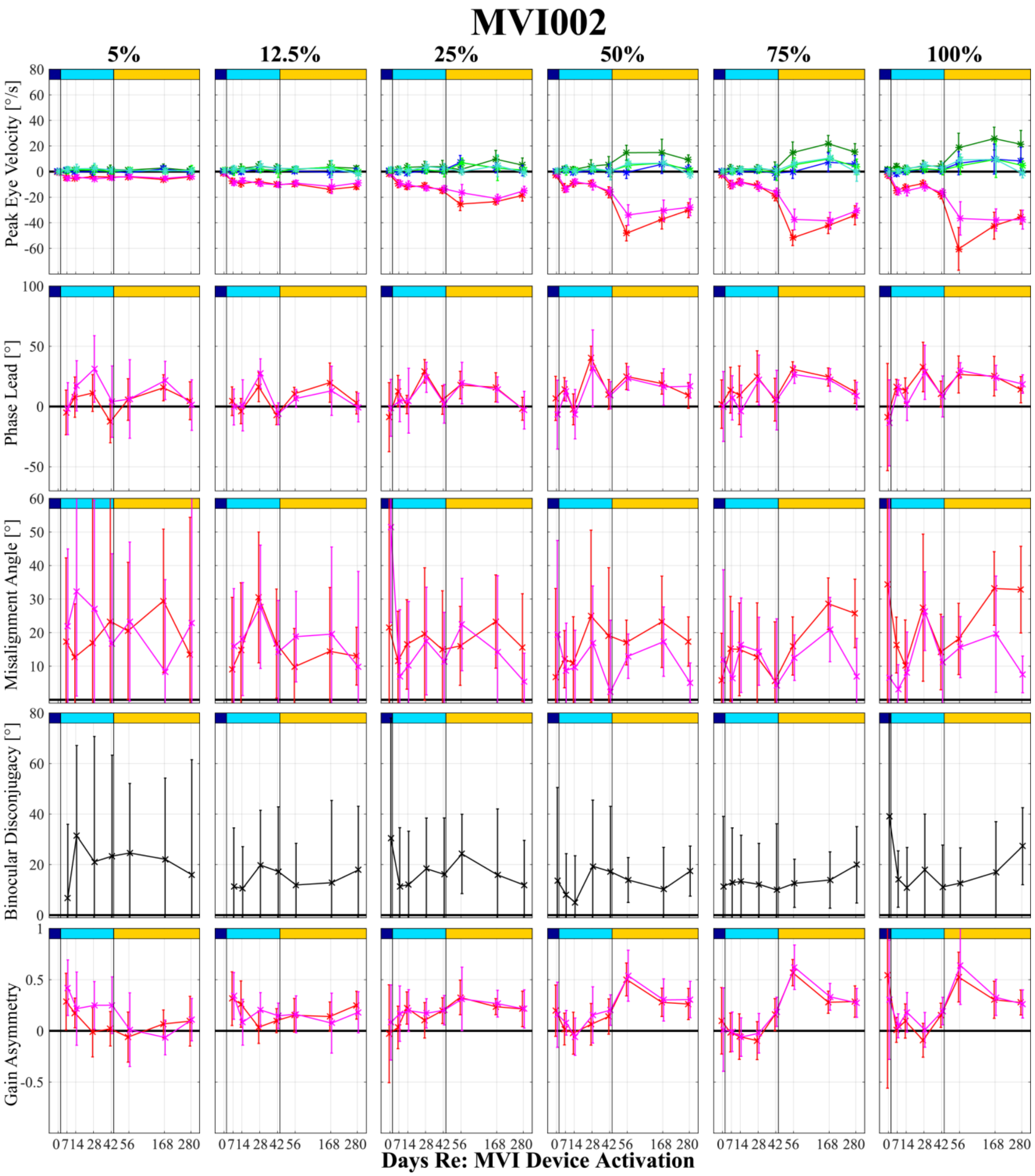

Figure 6.13. MVI002: LHE6: Longitudinal 2Hz virtual amplitude sweep.

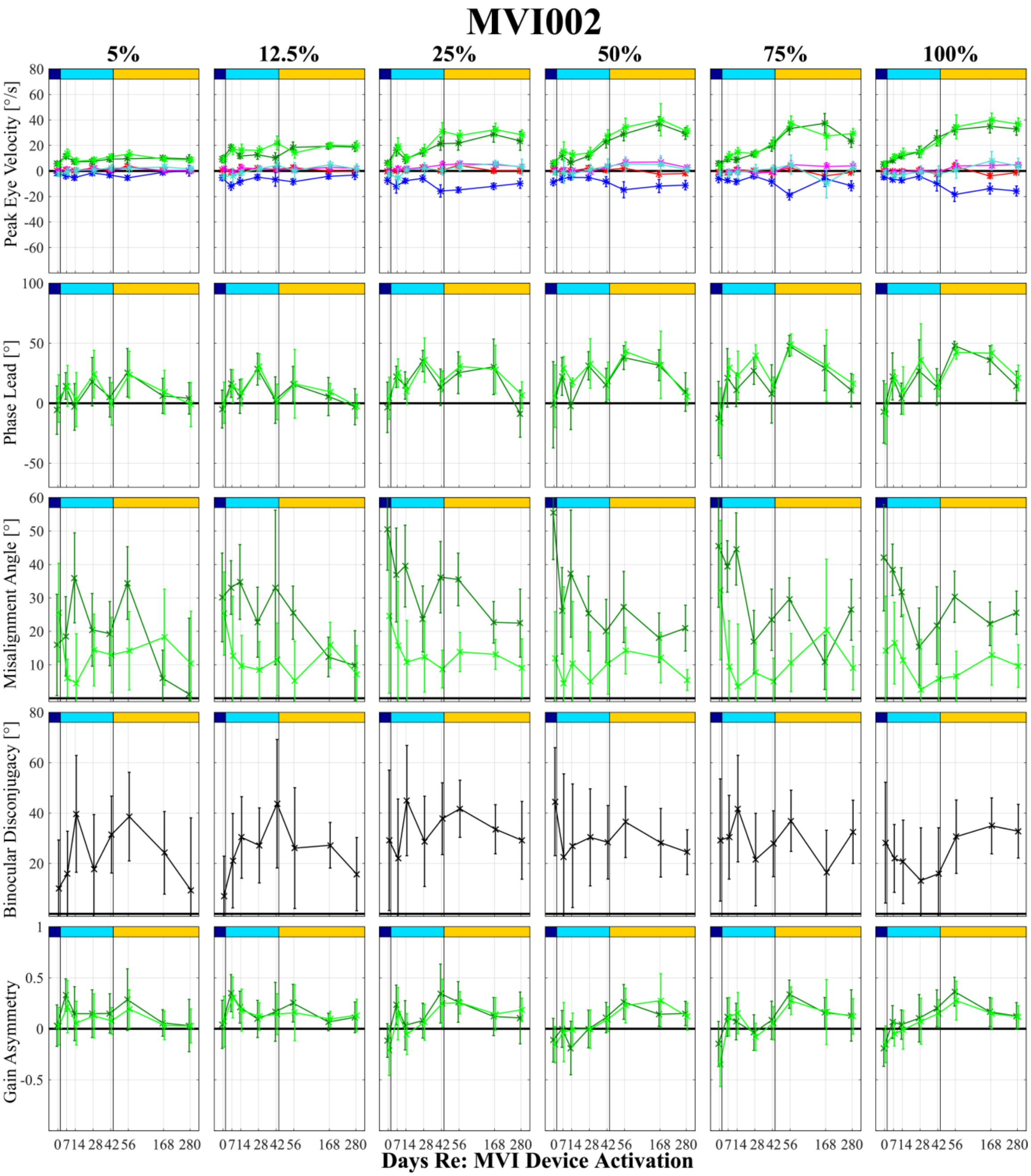

Figure 6.14. MVI002: LAE9: Longitudinal 2Hz virtual amplitude sweep.

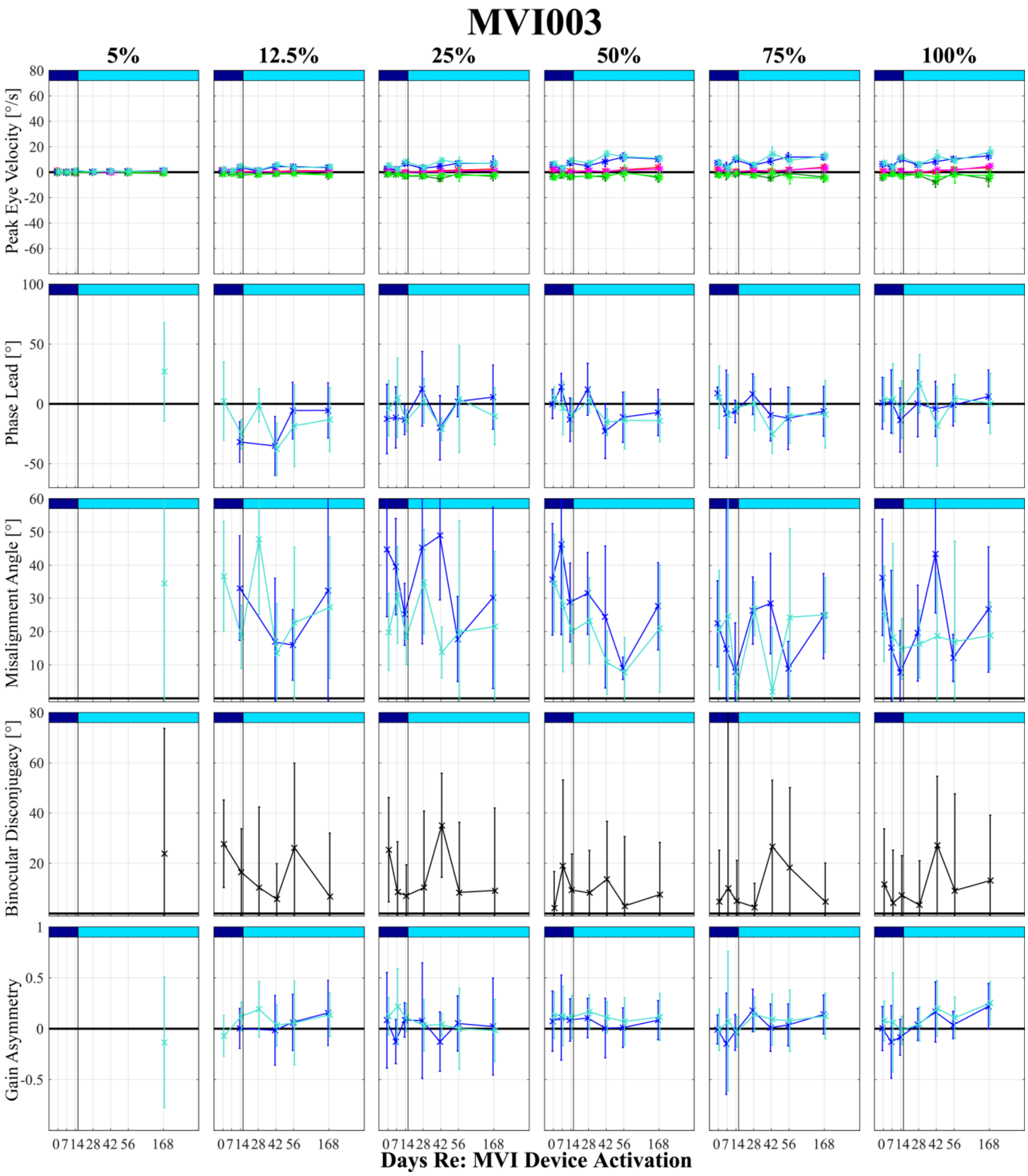

Figure 6.15. MVI003: LPE3: Longitudinal 2Hz virtual amplitude sweep.

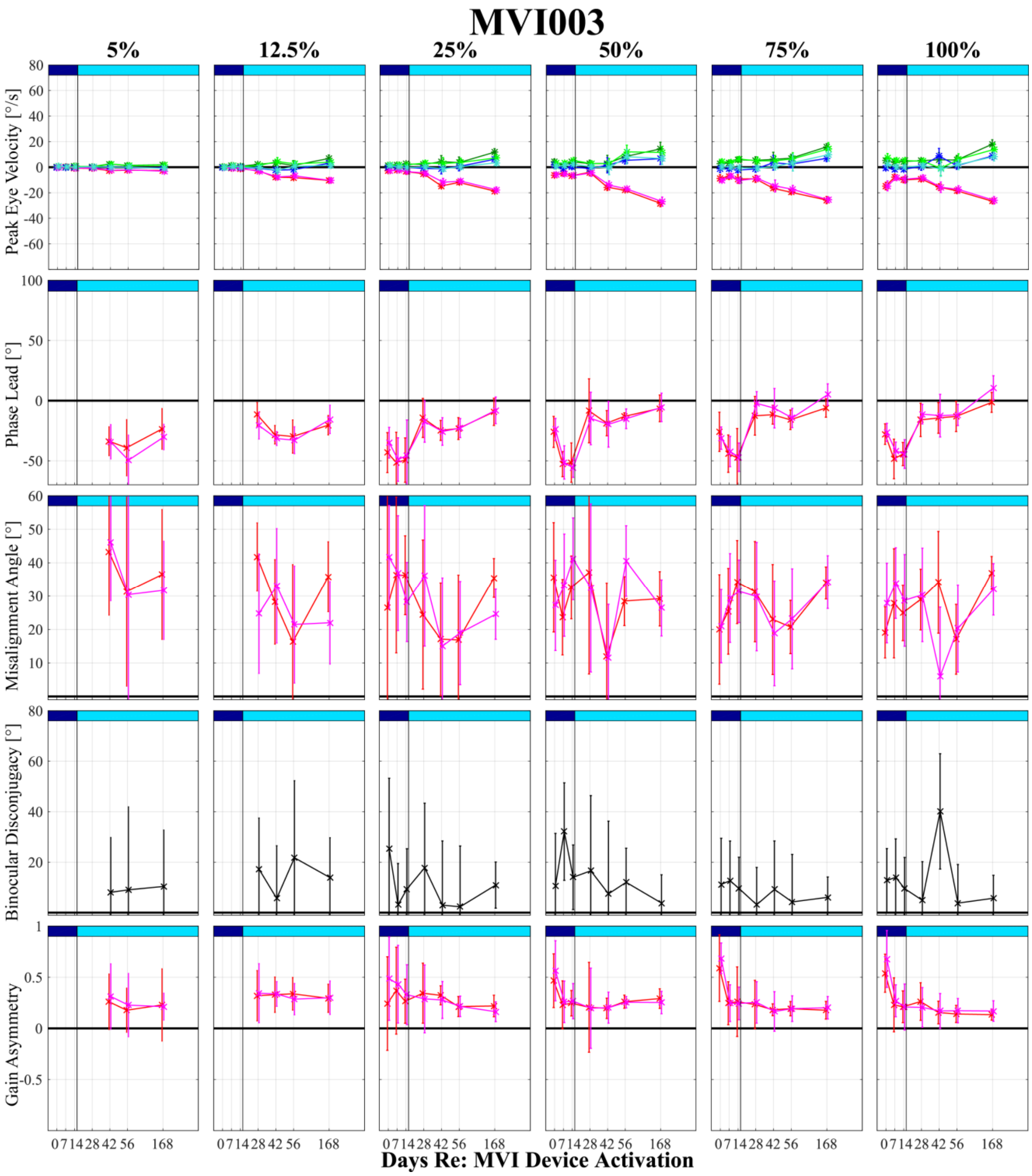

Figure 6.16. MVI003: LHE6: Longitudinal 2Hz virtual amplitude sweep.

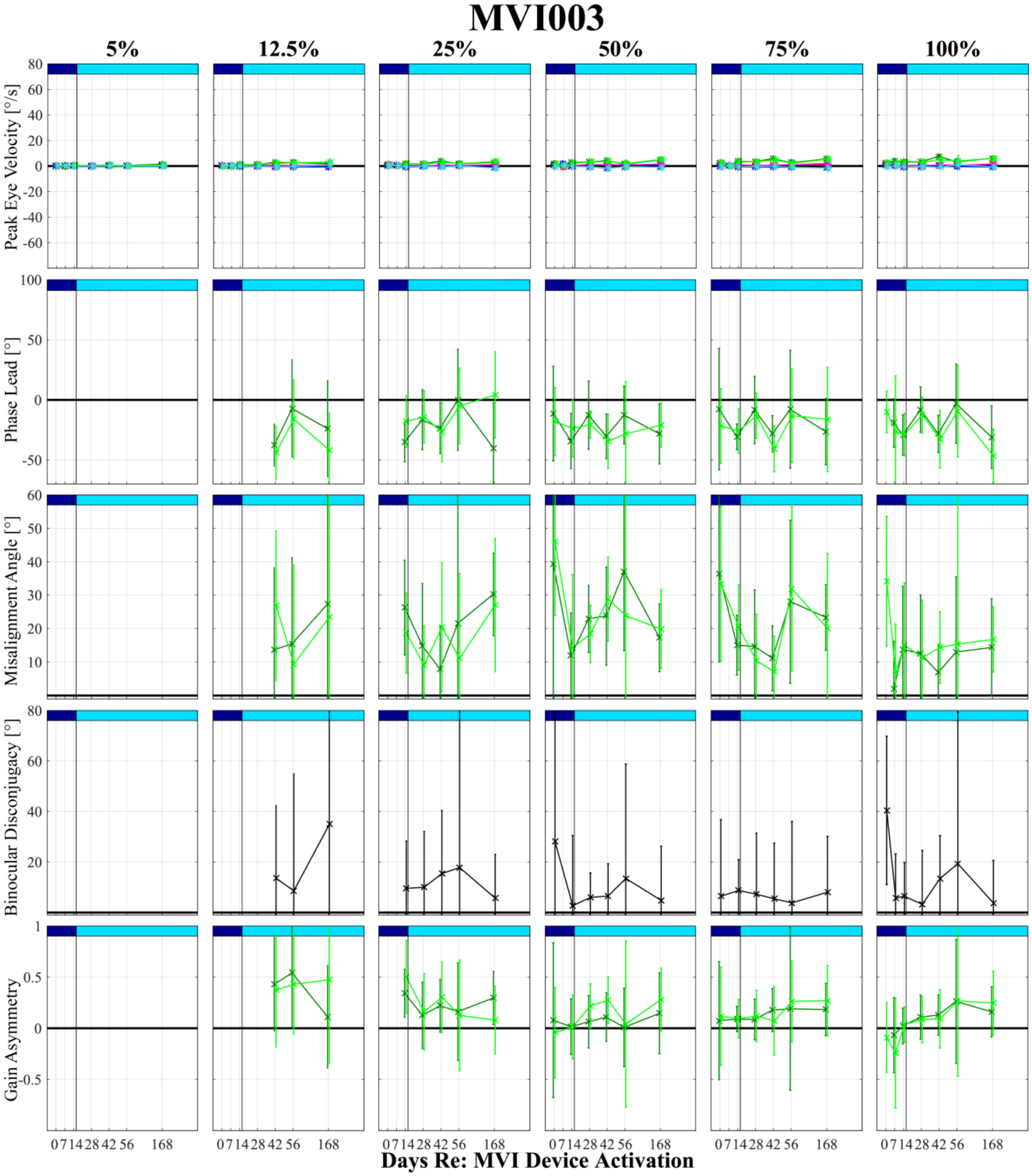

Figure 6.17. MVI003: LAE9: Longitudinal 2Hz virtual amplitude sweep.

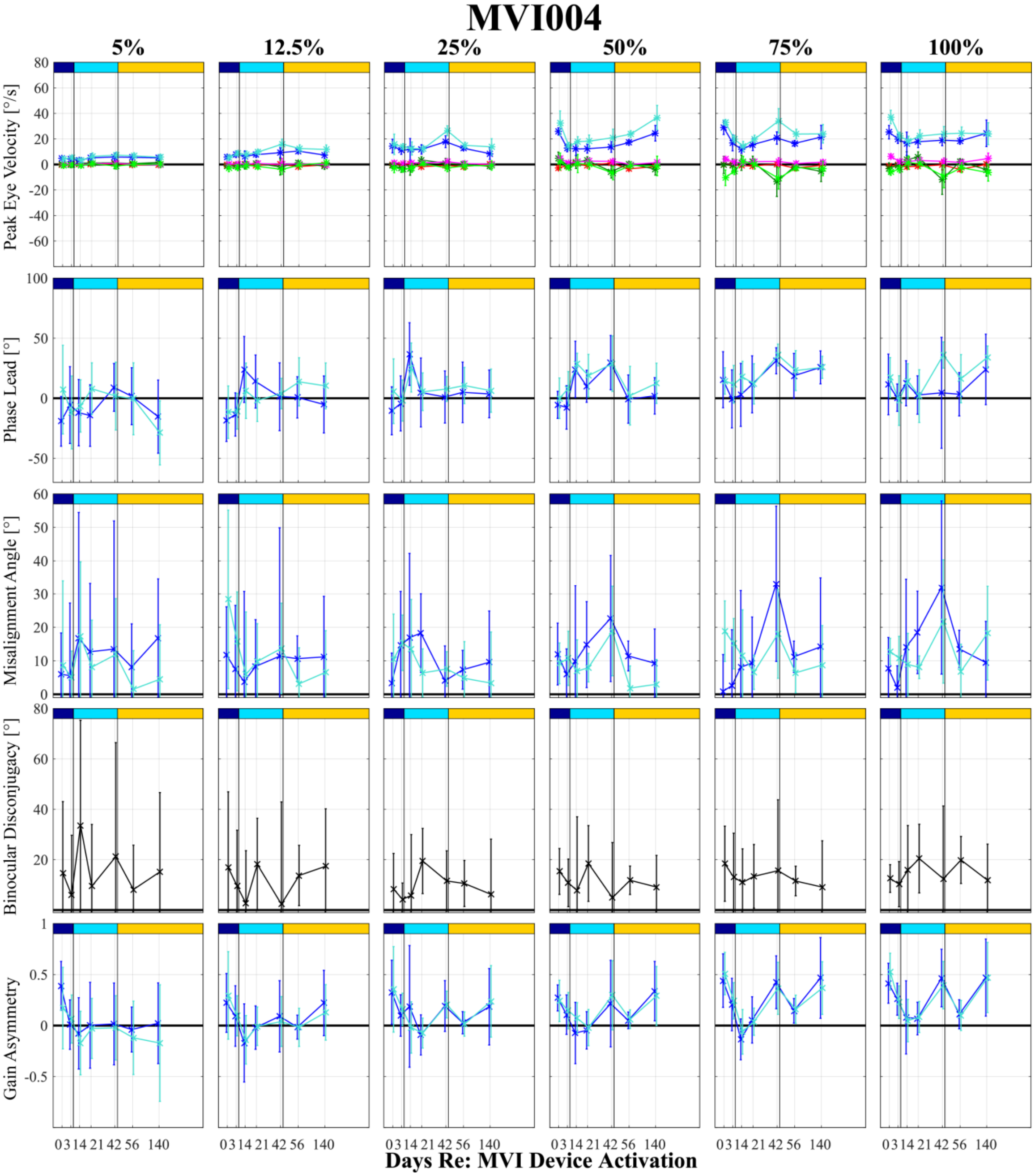

Figure 6.18. MVI004: LPE3: Longitudinal 2Hz virtual amplitude sweep.

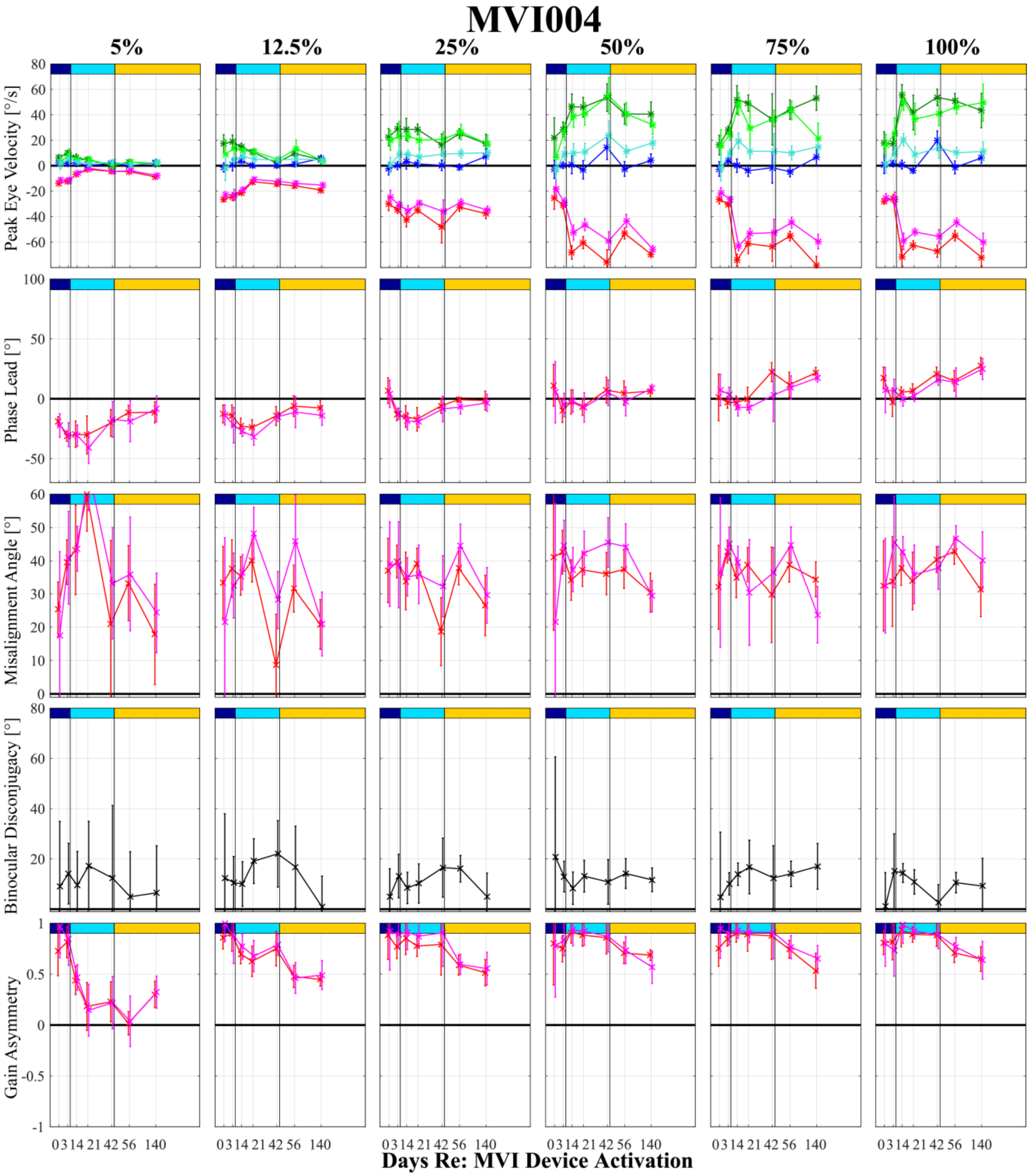

Figure 6.19. MVI004: LHE6: Longitudinal 2Hz virtual amplitude sweep.

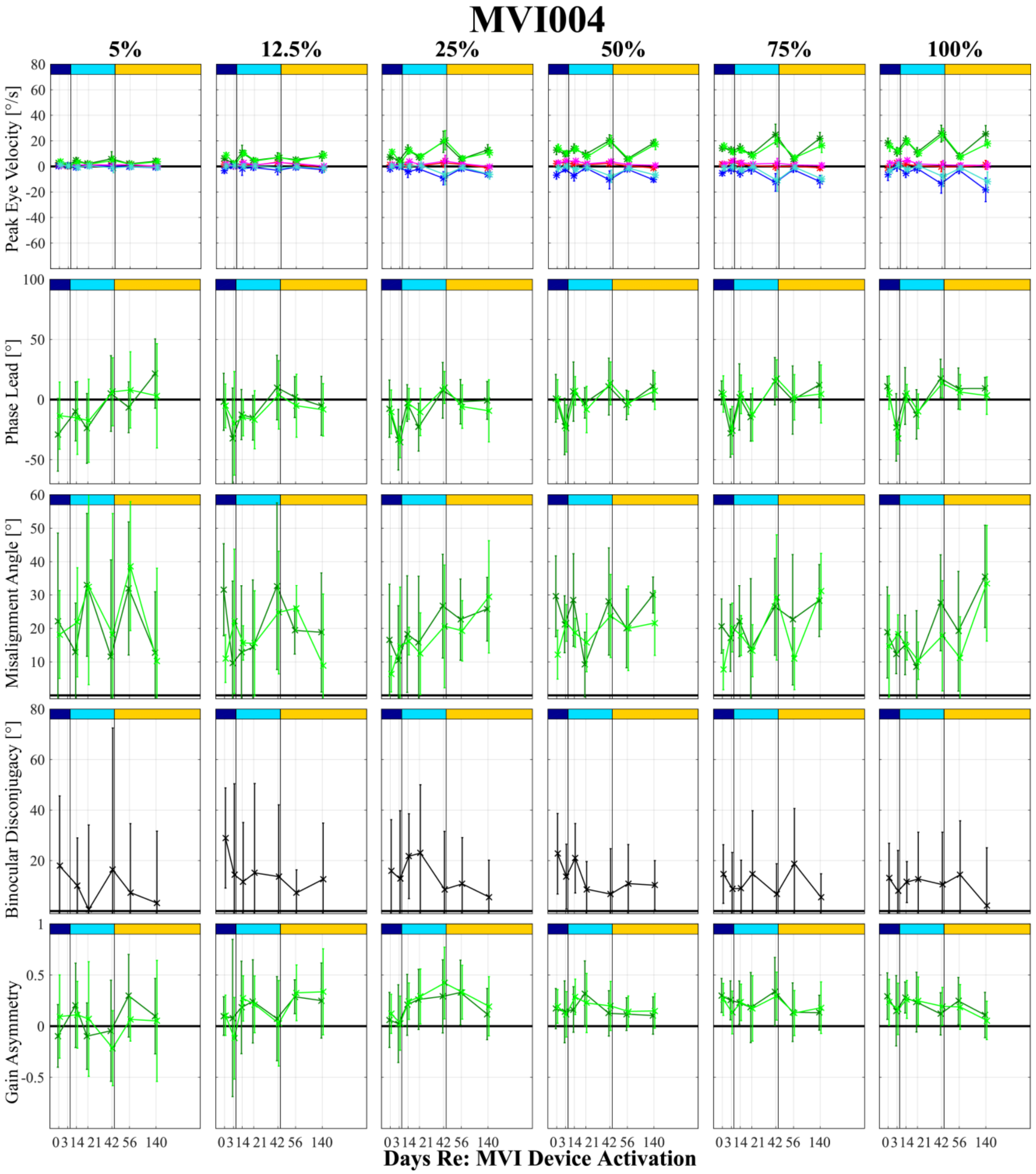

Figure 6.20. MVI004: LAE11: Longitudinal 2Hz virtual amplitude sweep.

6.6.2 100°/s Virtual Frequency Sweep

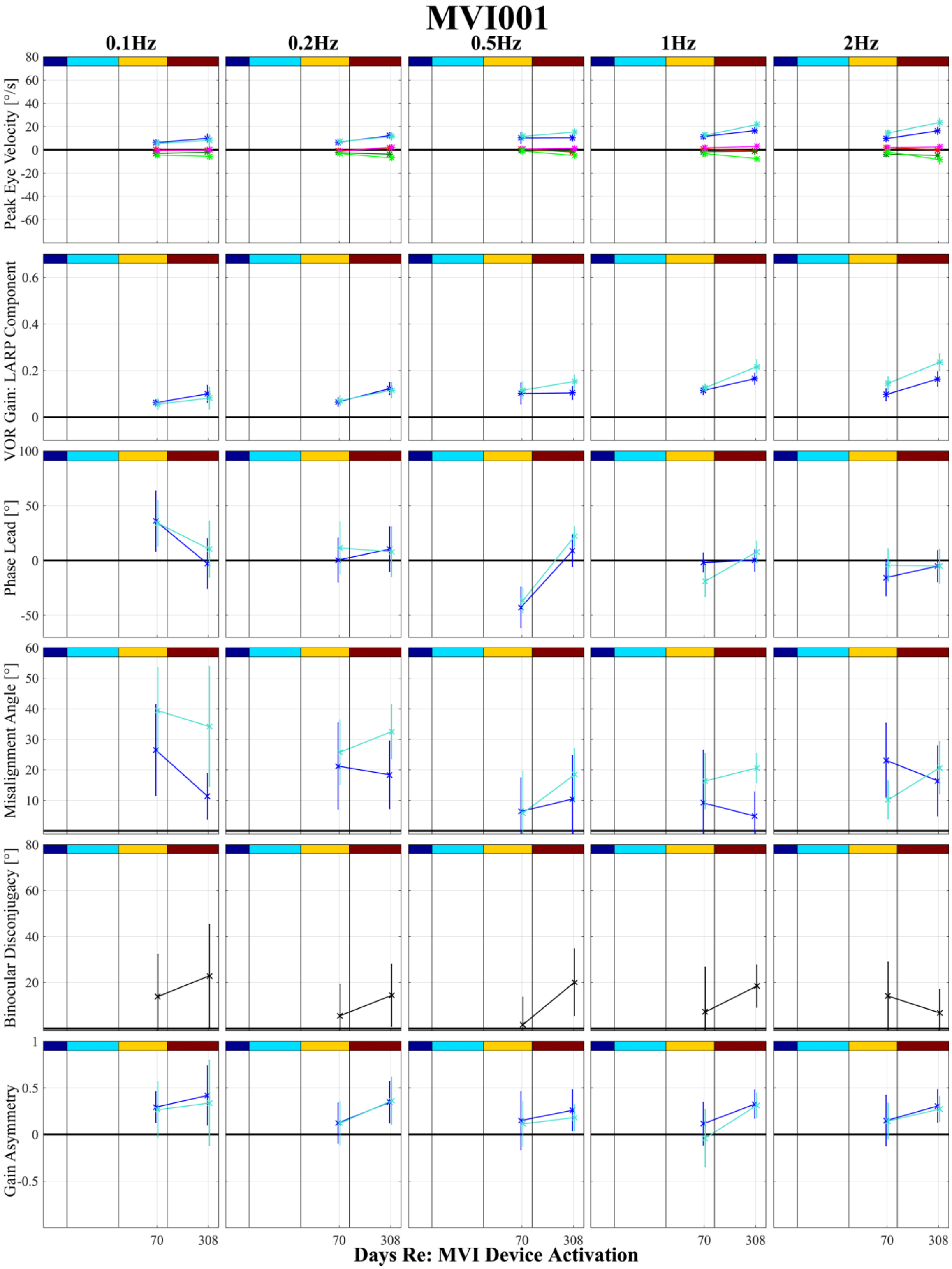

Figure 6.21. MVI001: LPE3: Longitudinal 100°/s virtual frequency sweep.

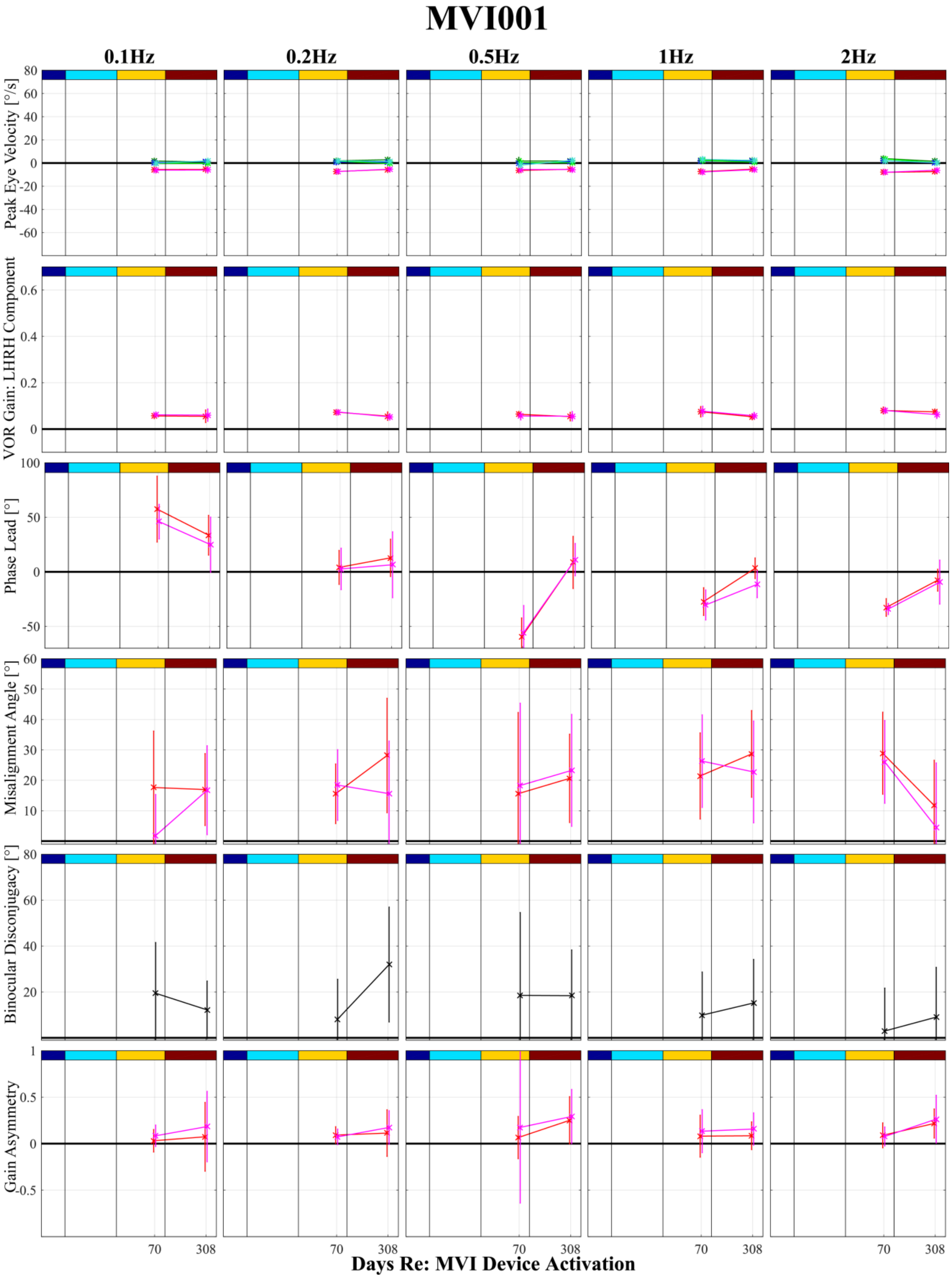

Figure 6.22. MVI001: LHE7: Longitudinal 100°/s virtual frequency sweep.

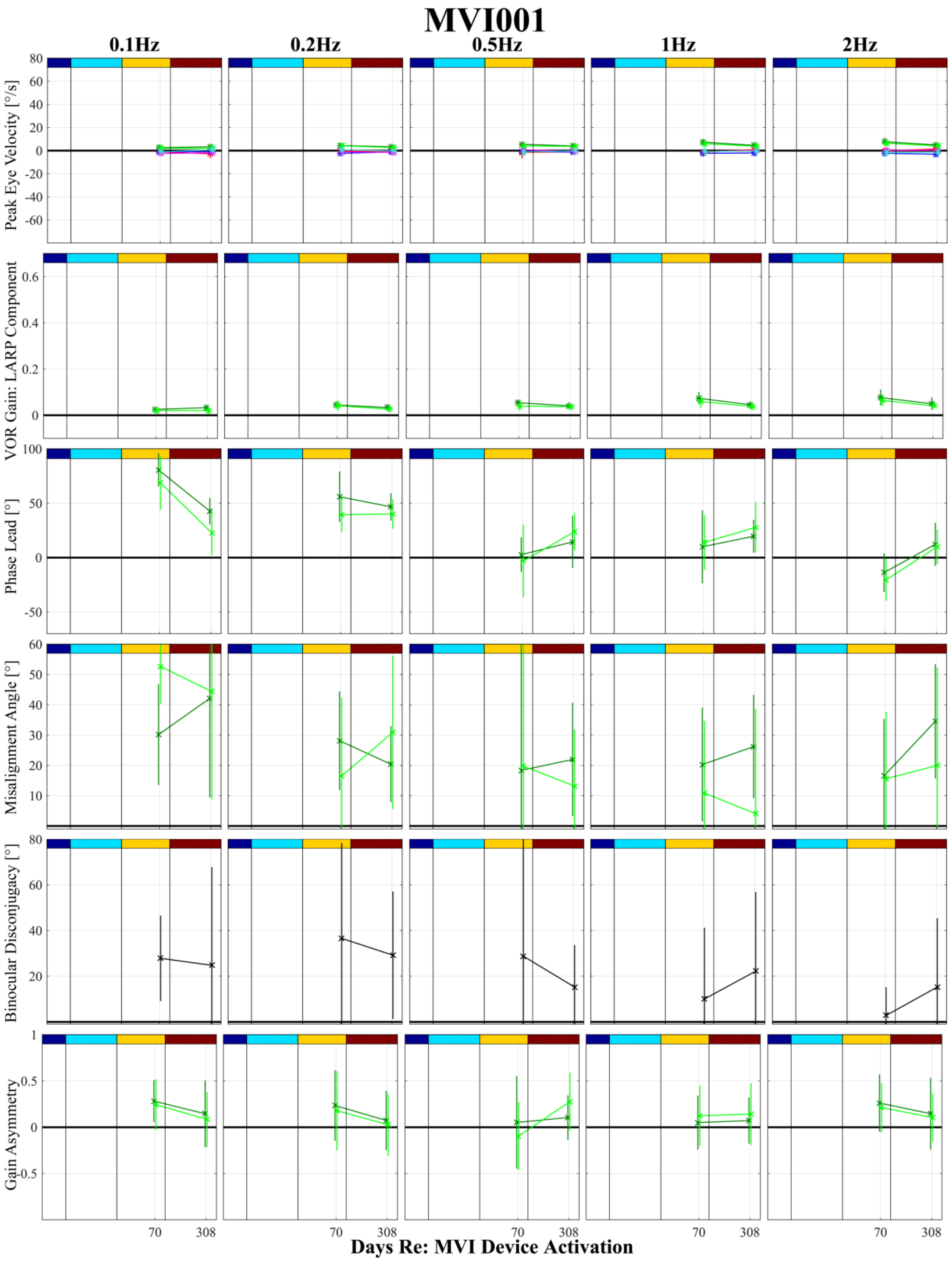

Figure 6.23. MVI001: LAE11: Longitudinal 100°/s virtual frequency sweep.

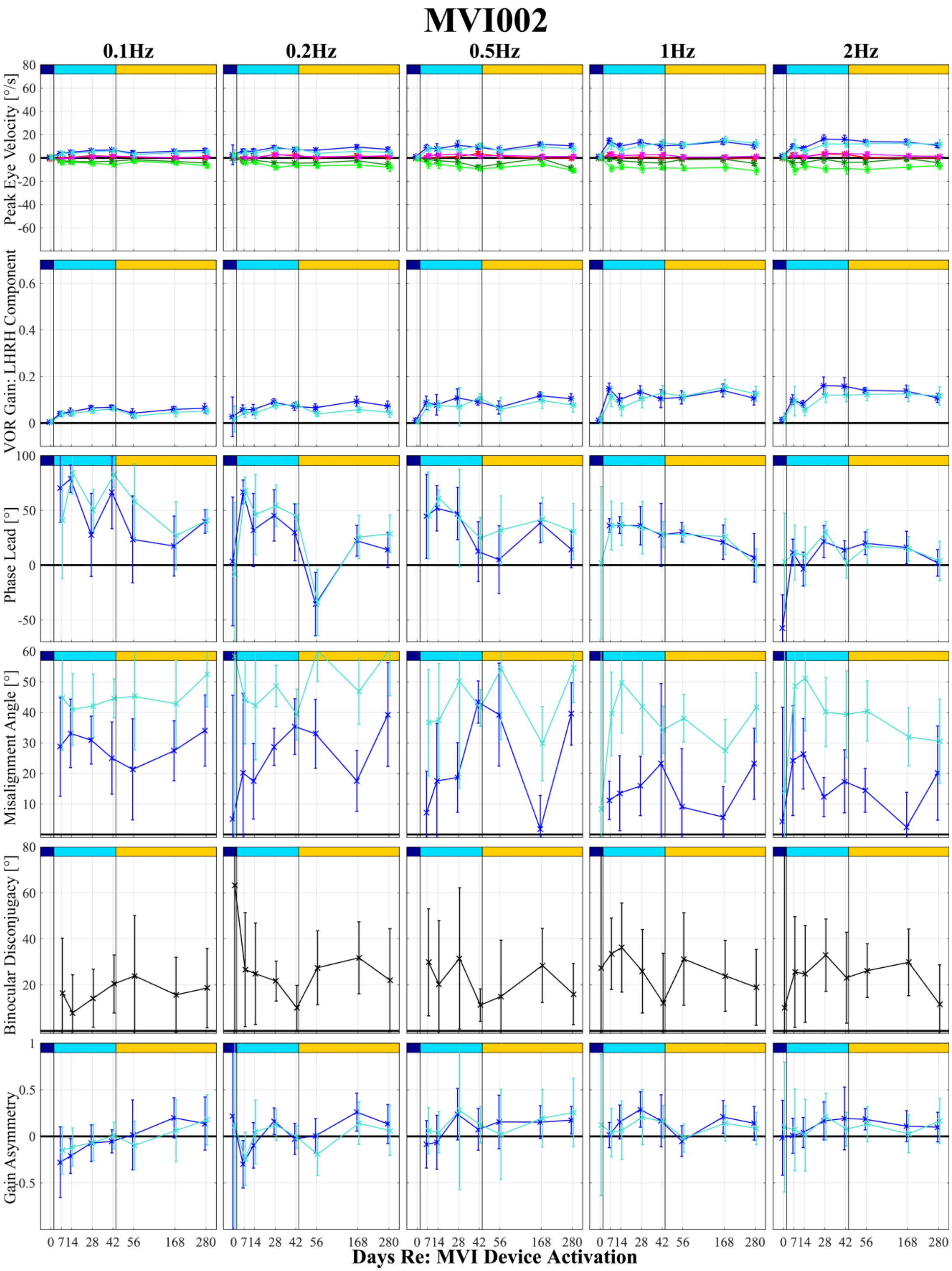

Figure 6.24. MVI002: LPE3: Longitudinal 100°/s virtual frequency sweep.

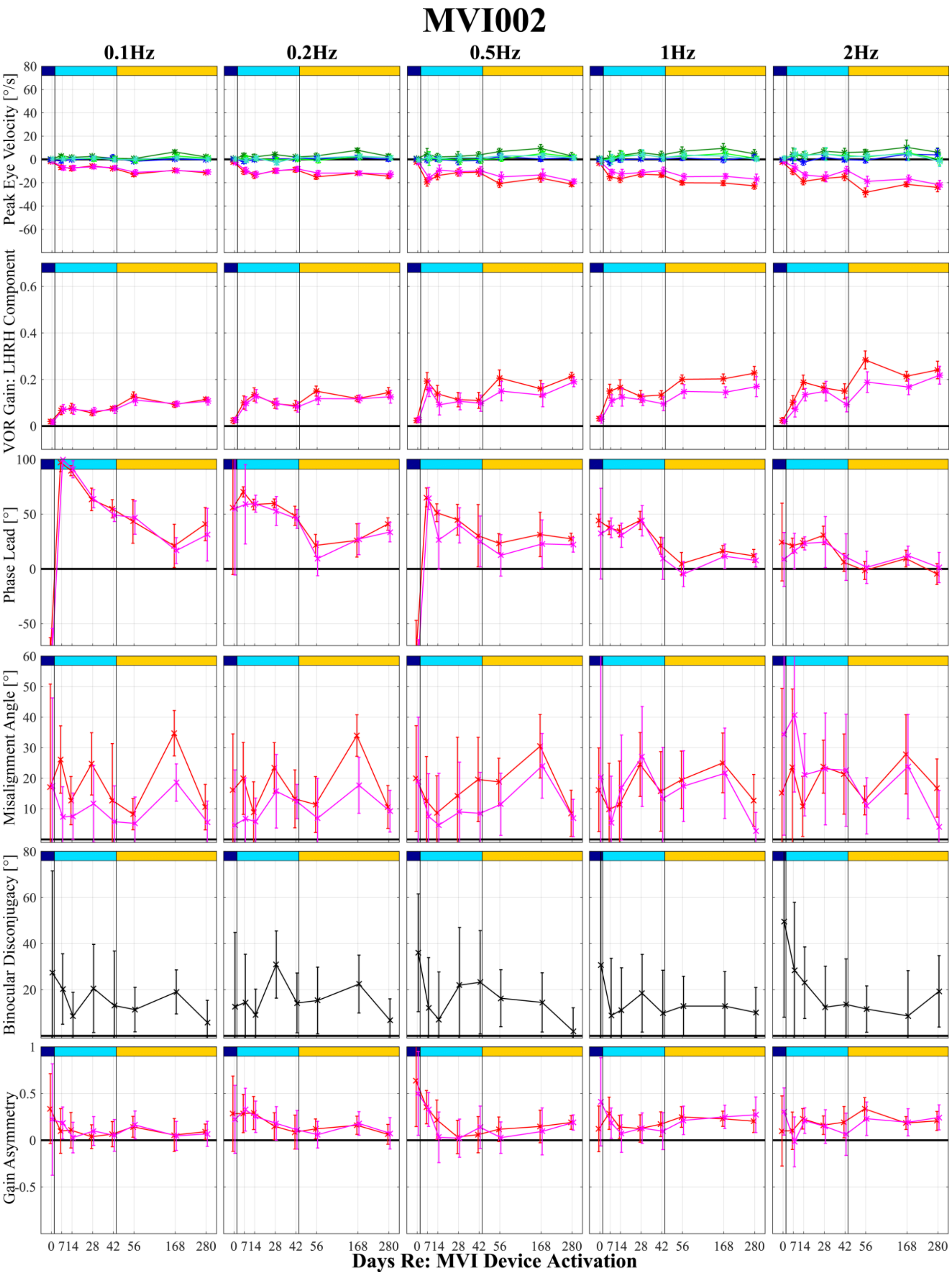

Figure 6.25. MVI002: LHE6: Longitudinal 100°/s virtual frequency sweep.

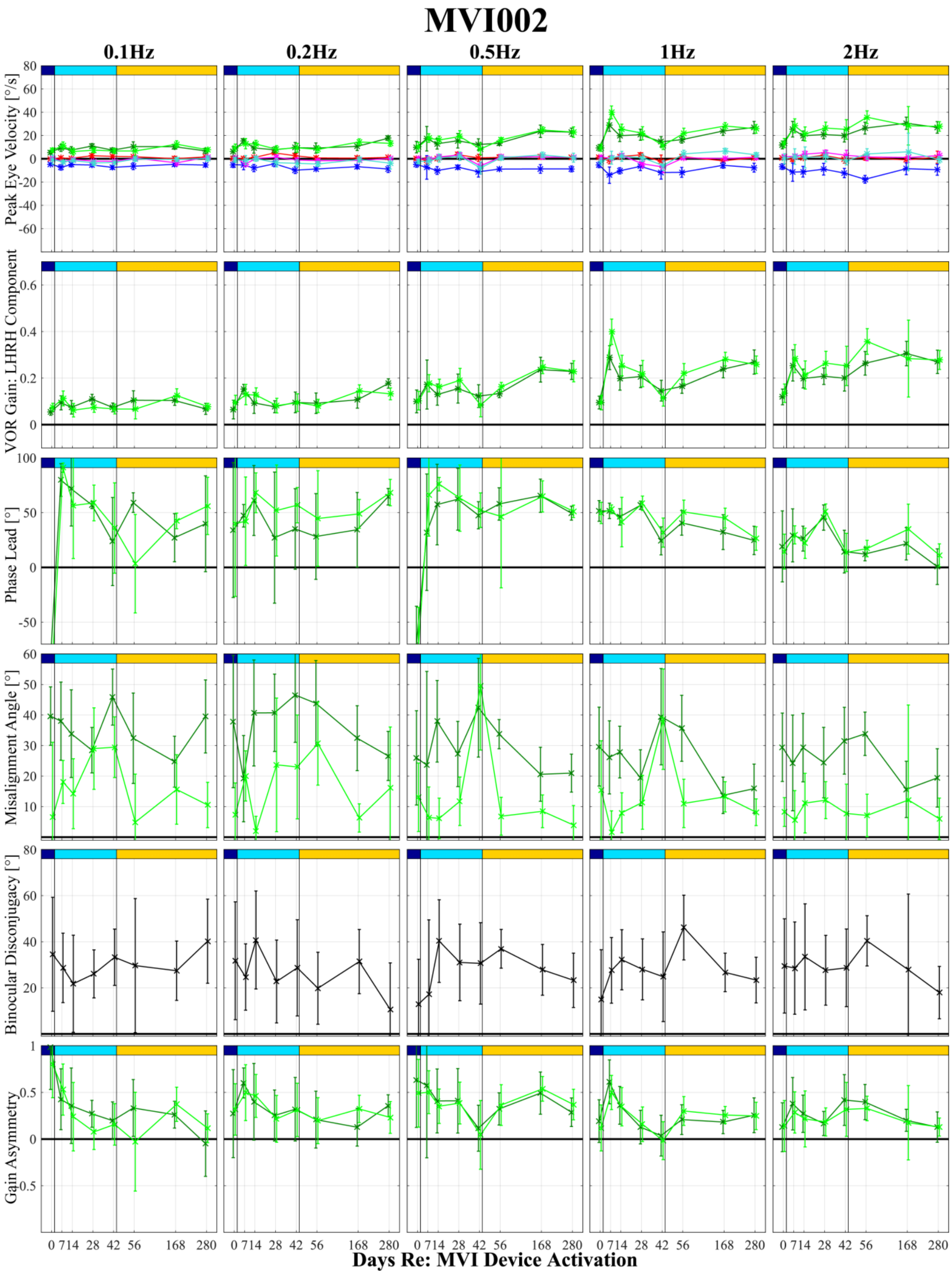

Figure 6.26. MVI002: LAE9: Longitudinal 100°/s virtual frequency sweep.

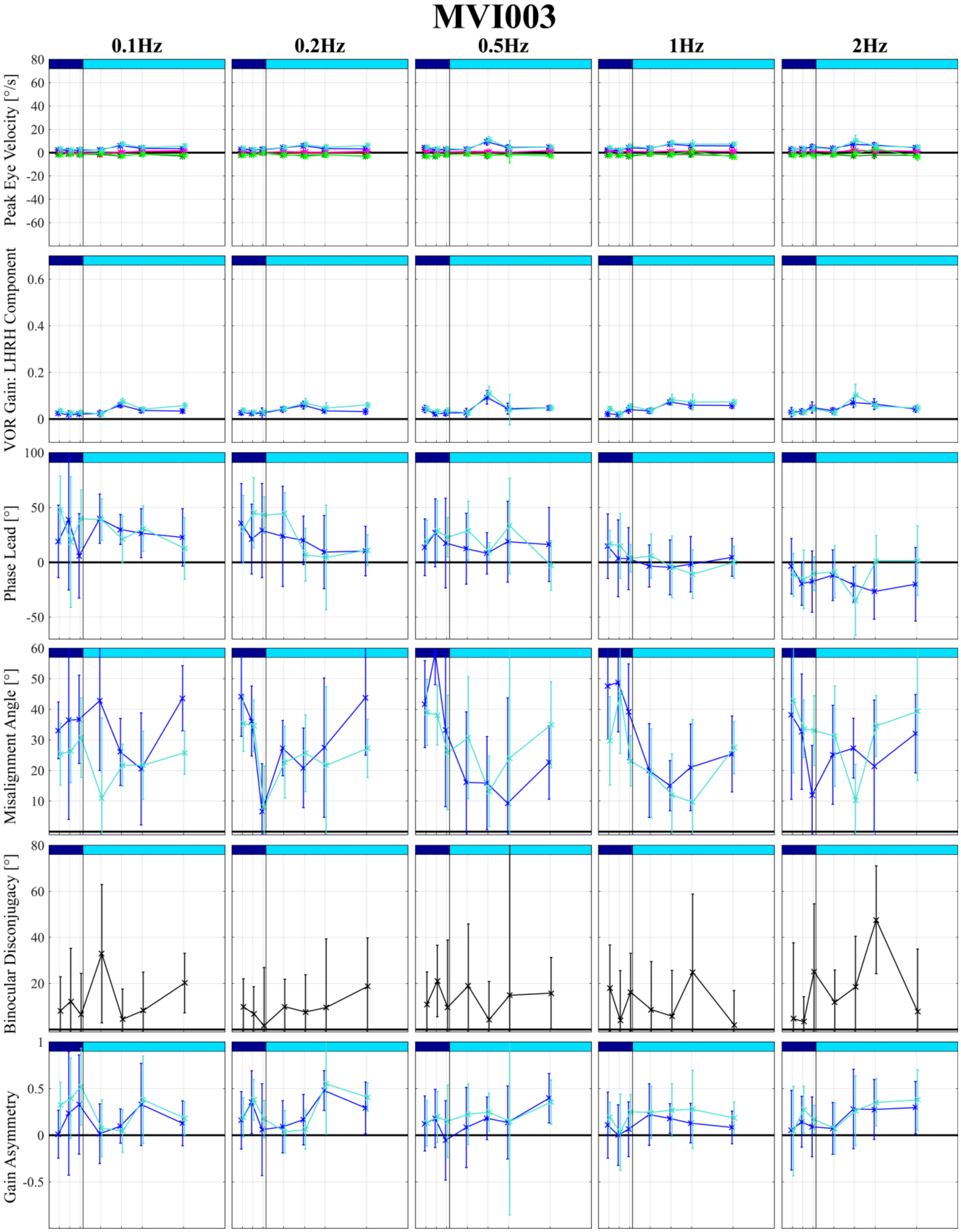

Figure 6.27. MVI003: LPE3: Longitudinal 100°/s virtual frequency sweep.

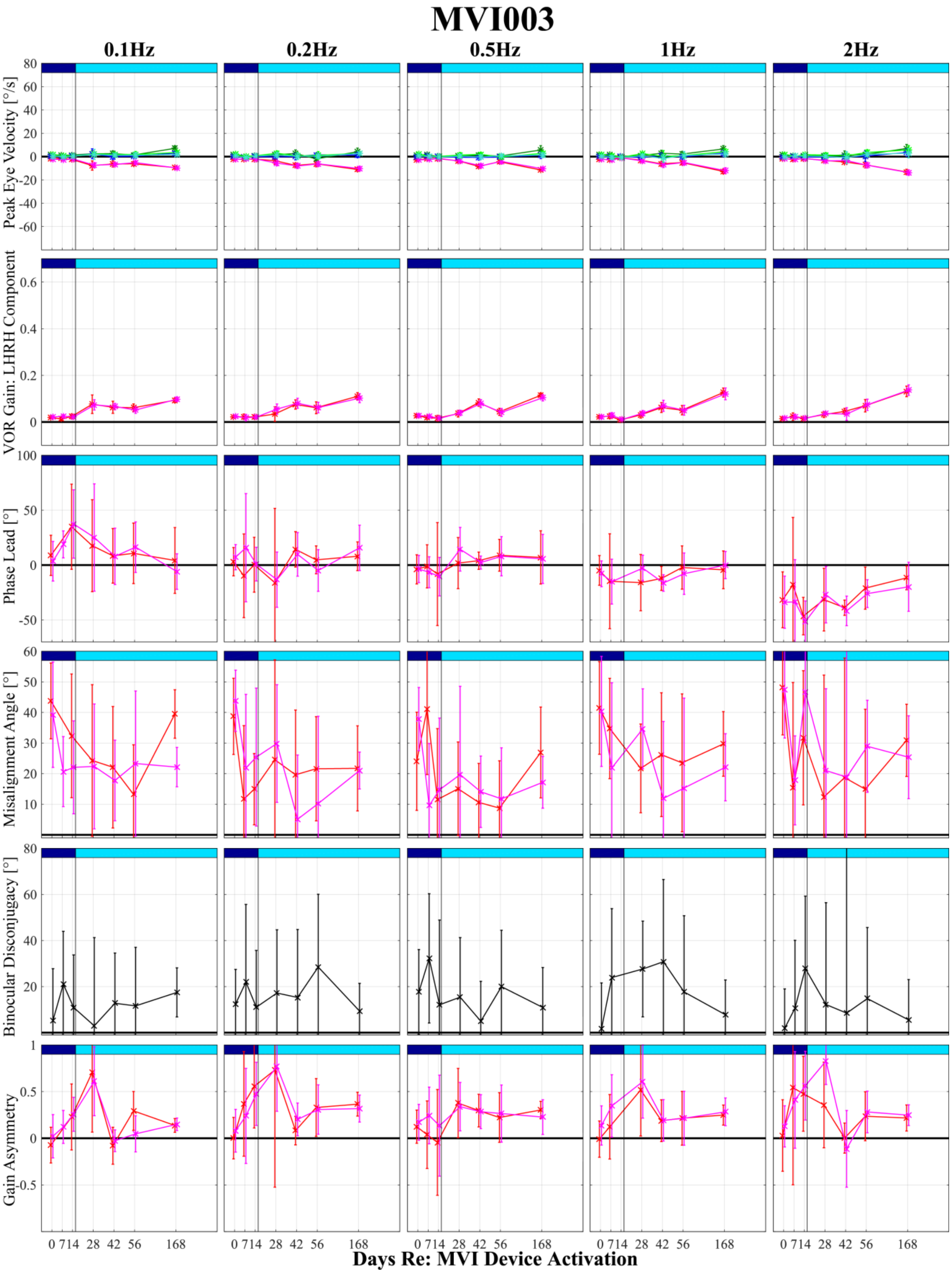

Figure 6.28. MVI003: LHE6: Longitudinal 100°/s virtual frequency sweep.

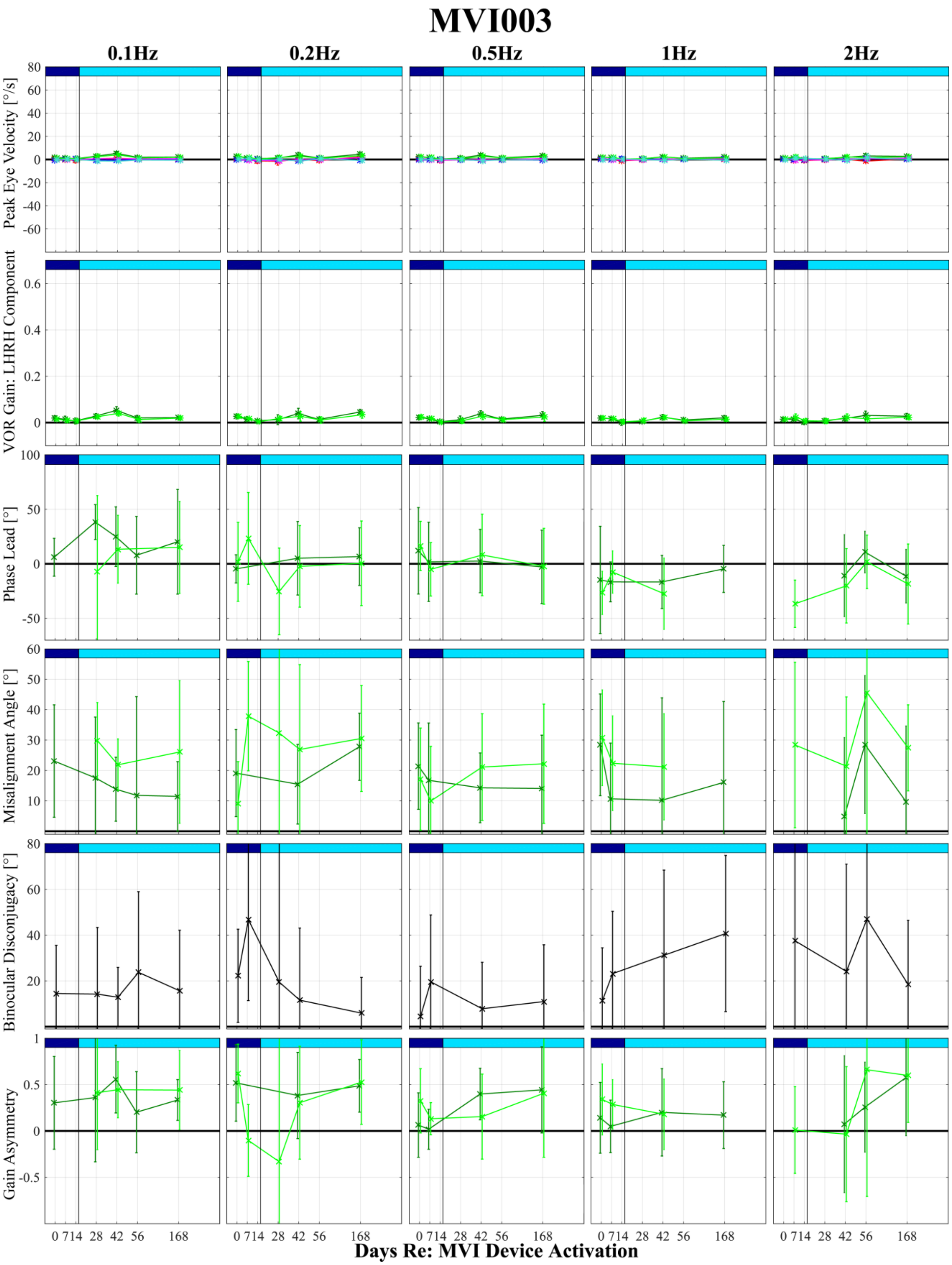

Figure 6.29. MVI003: LAE9: Longitudinal 100°/s virtual frequency sweep.

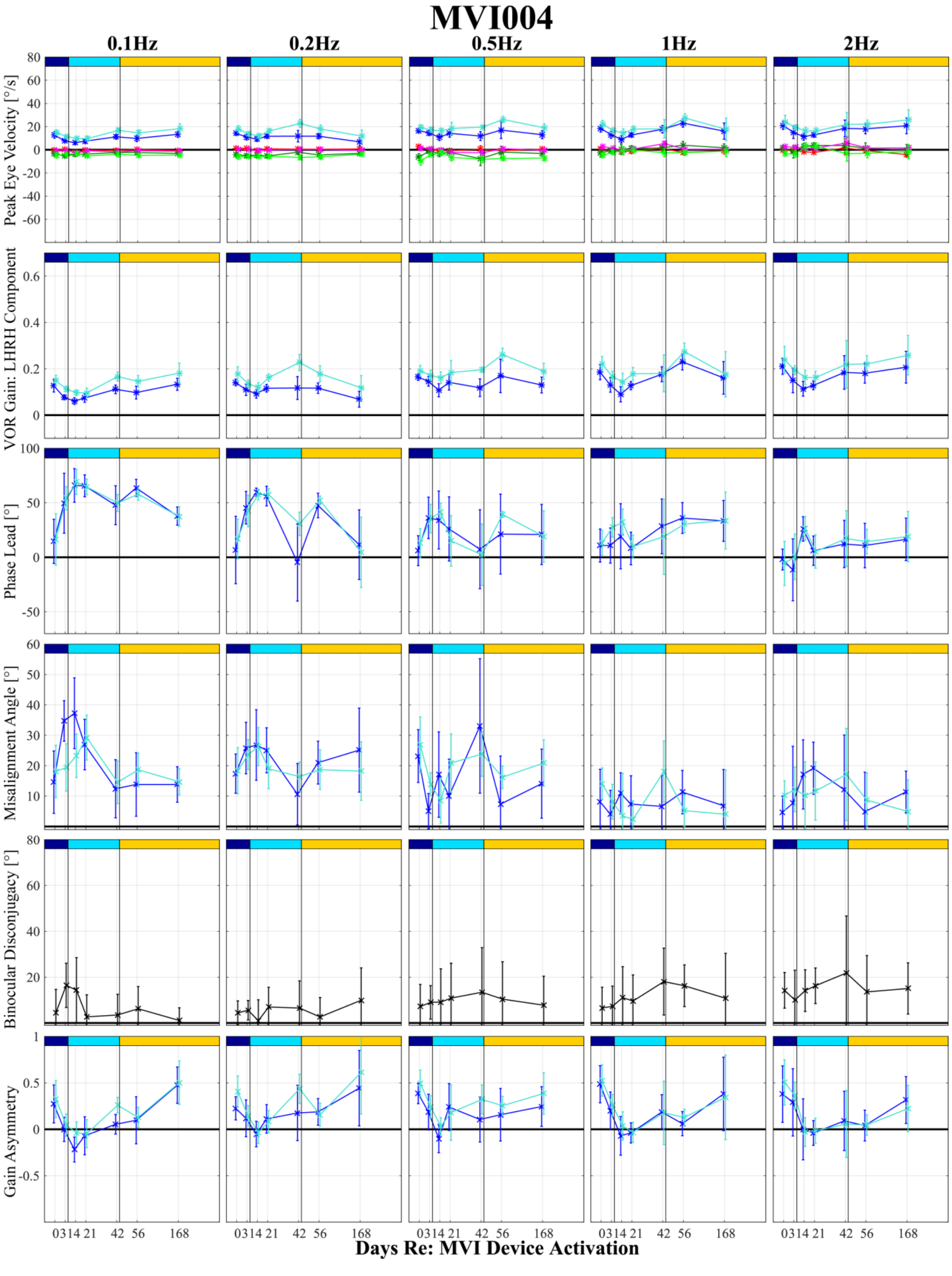

Figure 6.30. MVI004: LPE3: Longitudinal 100°/s virtual frequency sweep.

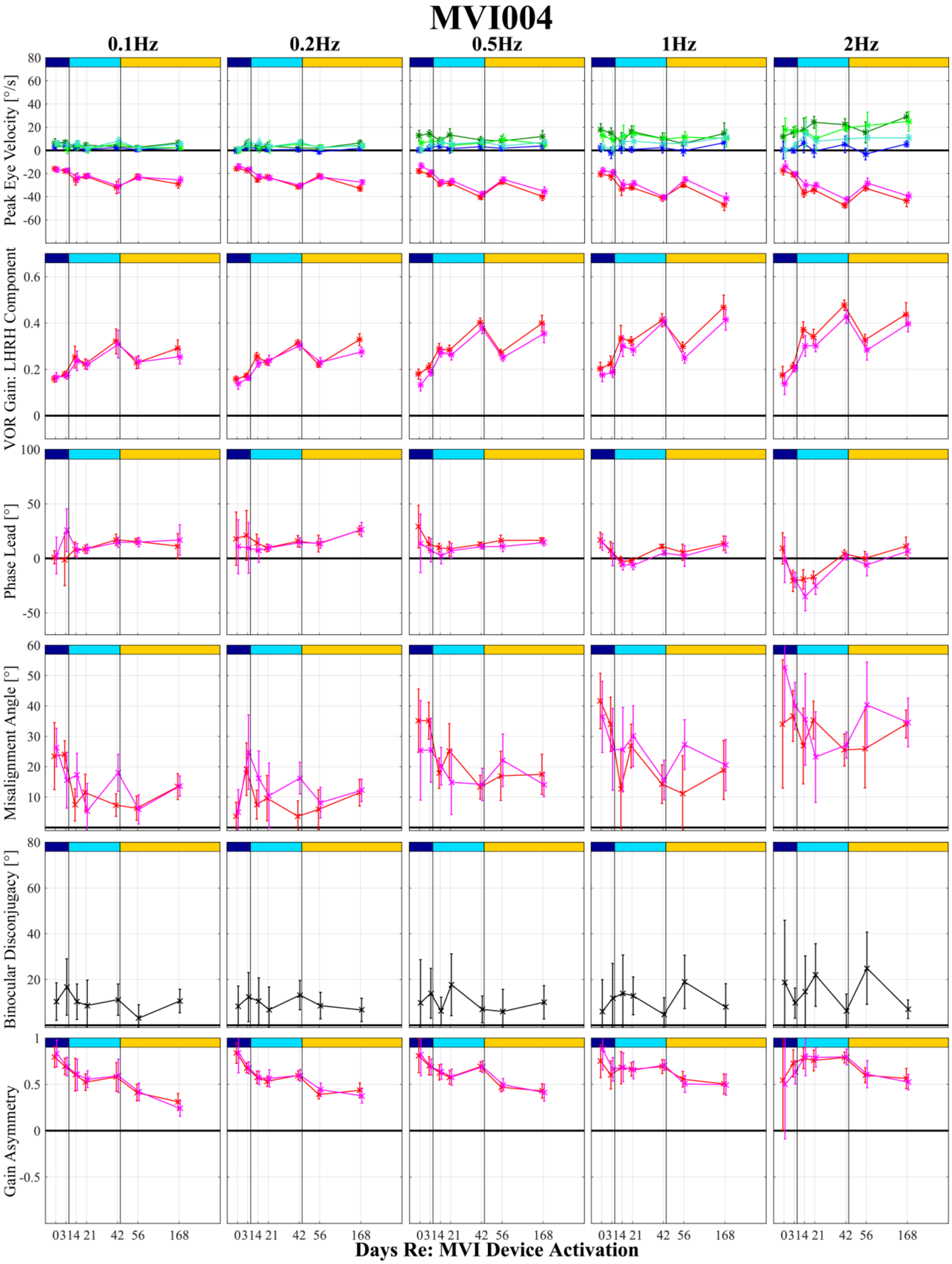

Figure 6.31. MVI004: LHE6: Longitudinal 100°/s virtual frequency sweep.

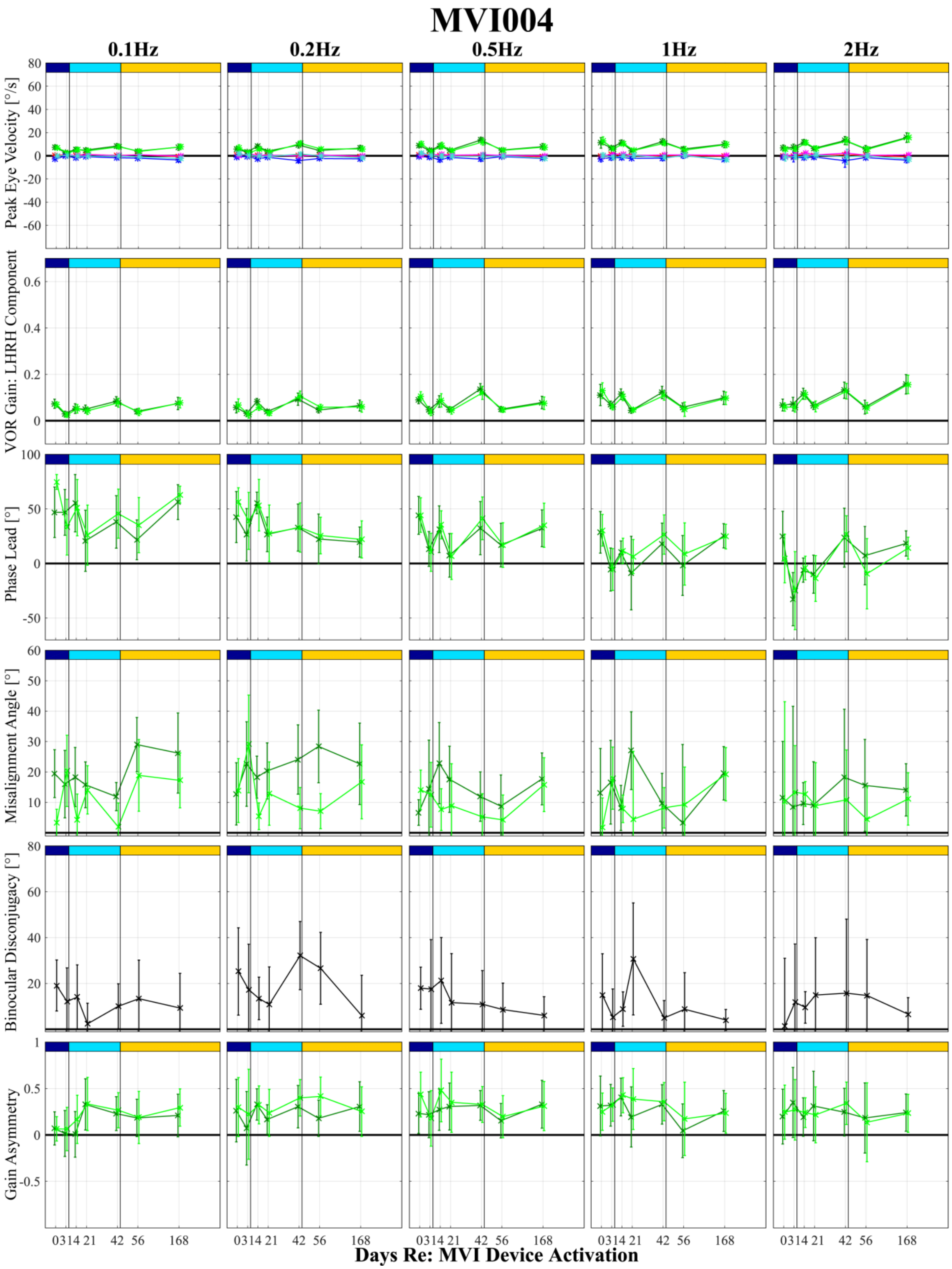

Figure 6.32. MVI004: LAE11: Longitudinal 100°/s virtual frequency sweep.

6.6.3 100°/s Rotary Chair Frequency Sweep

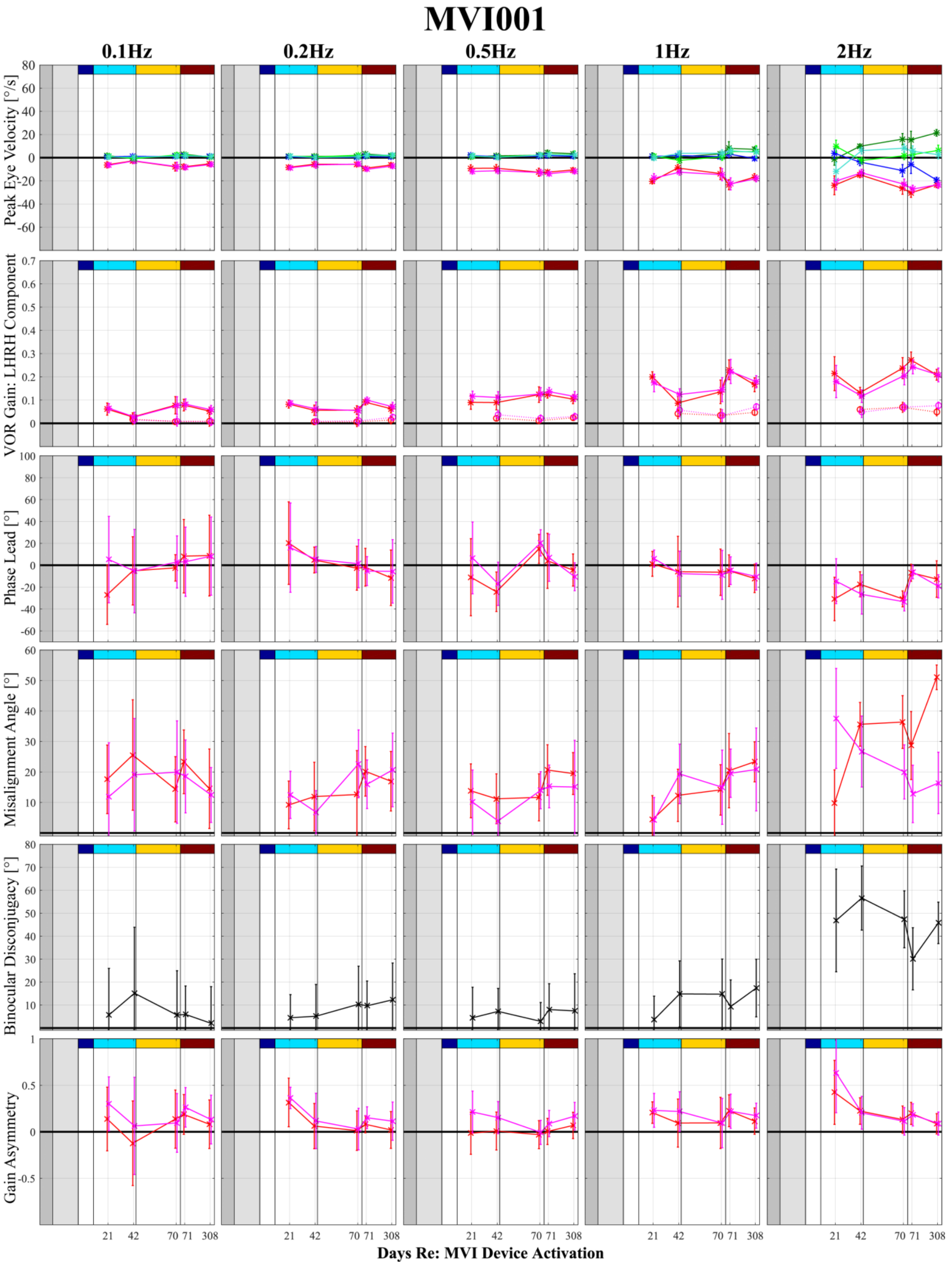

Figure 6.33. MVI001: LHRH: Longitudinal 100°/s rotary chair frequency sweep.

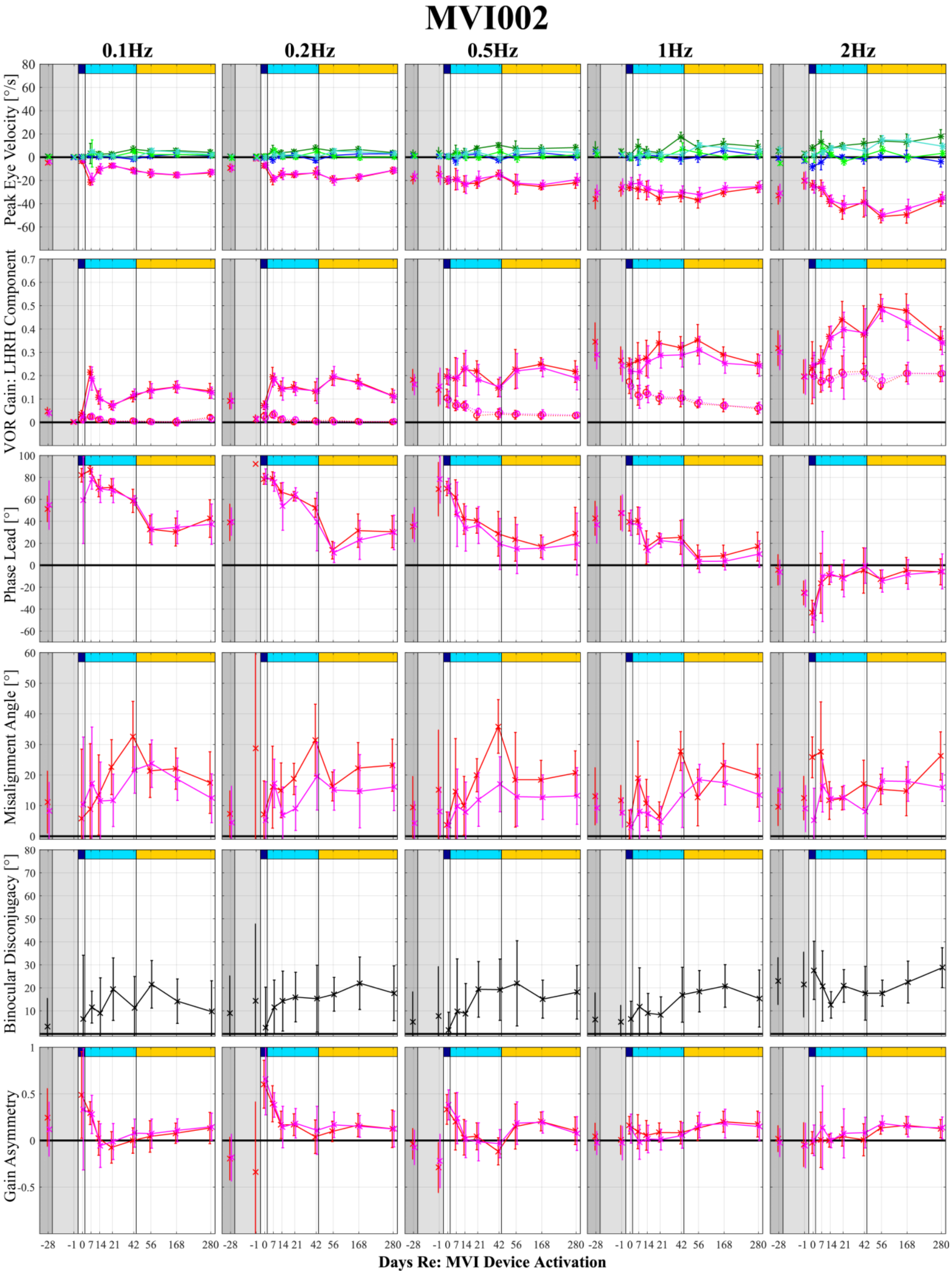

Figure 6.34. MVI002: LHRH: Longitudinal 100°/s rotary chair frequency sweep.

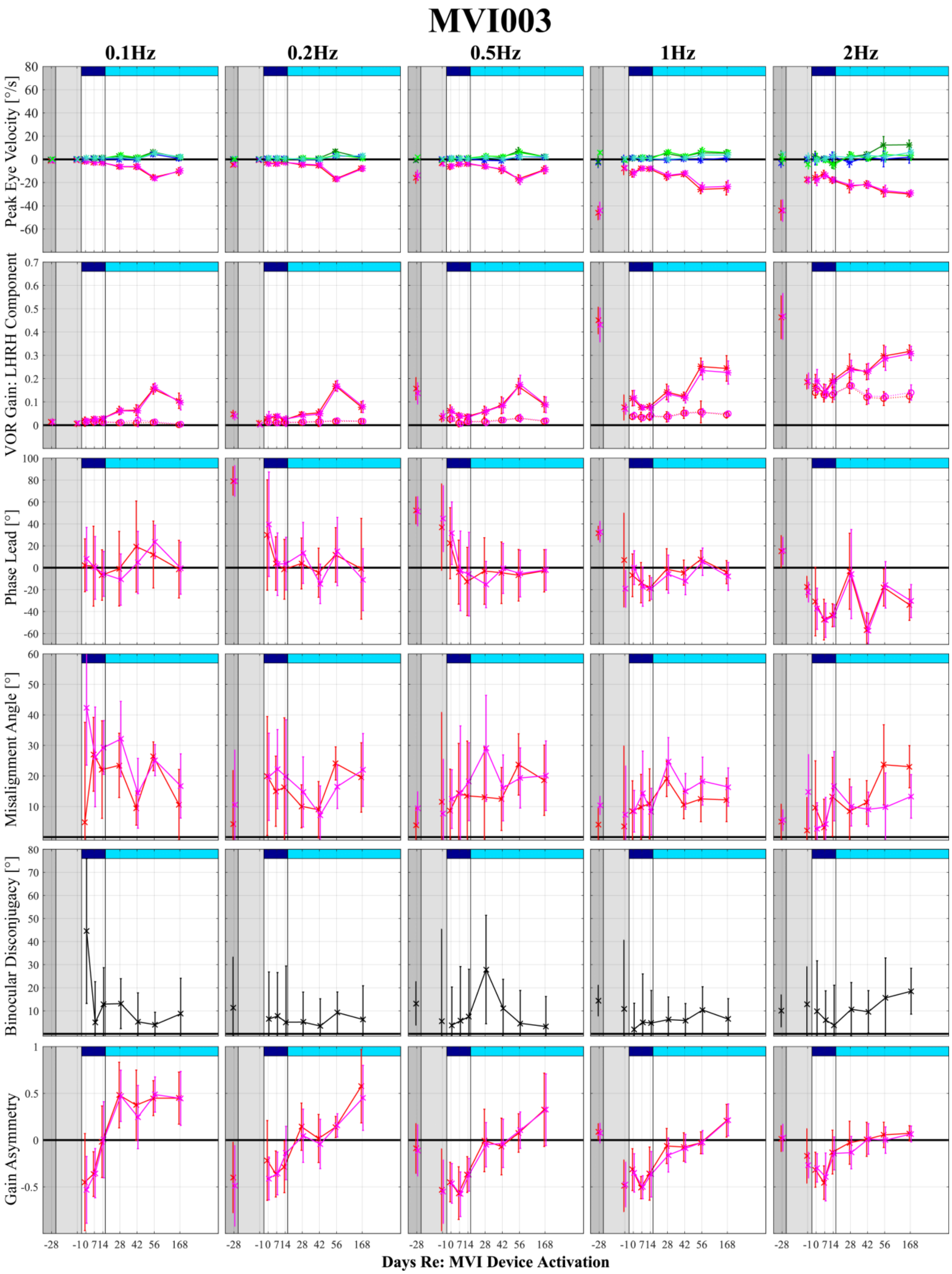

Figure 6.35. MVI003: LHRH: Longitudinal 100°/s rotary chair frequency sweep.

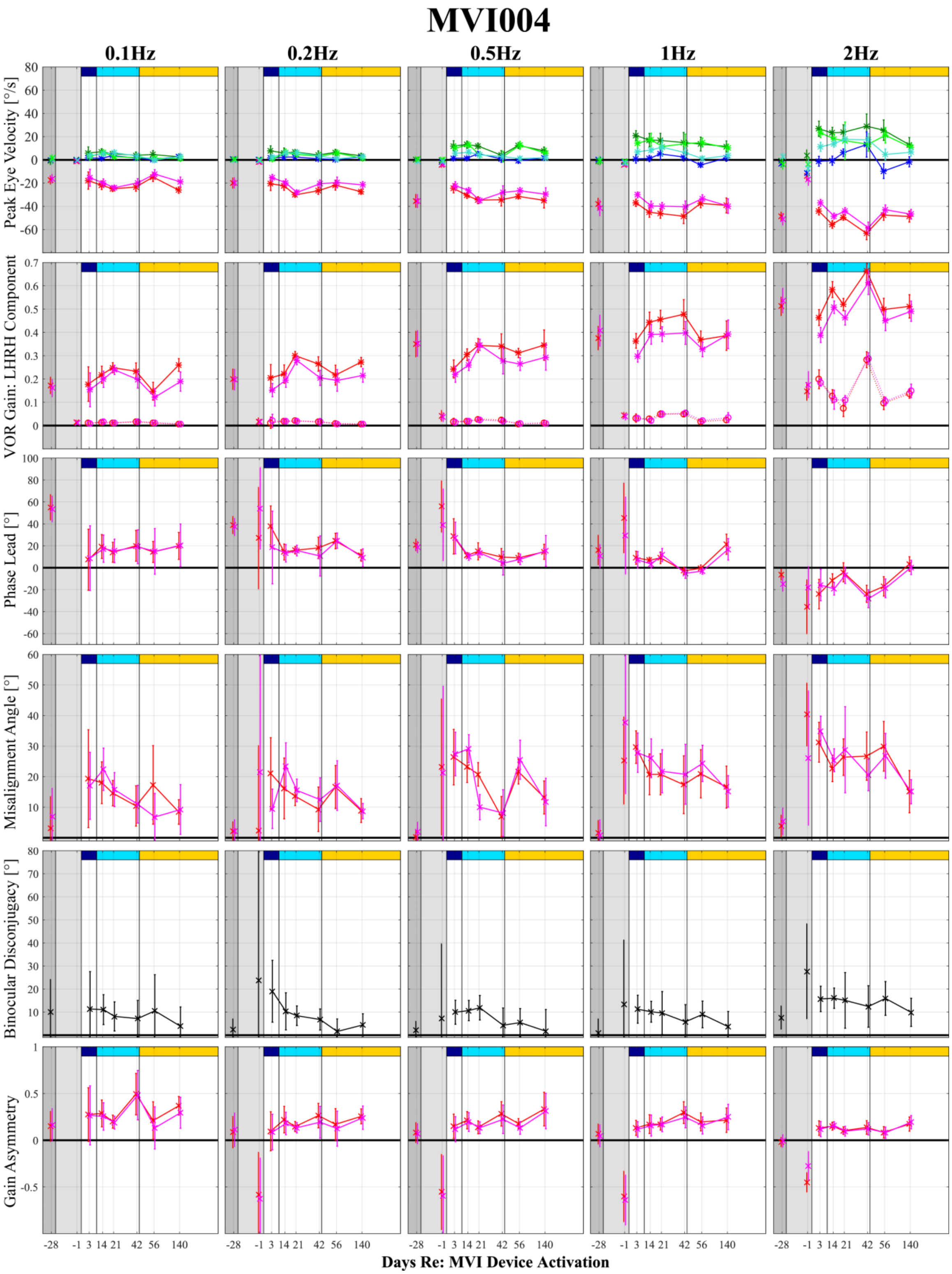

Figure 6.36. MVI004: LHRH: Longitudinal 100°/s rotary chair frequency sweep.

References

[1] Ward, B. K., Agrawal, Y., Hoffman, H. J., Carey, J. P., and Della Santina, C. C., 2013, "Prevalence and Impact of Bilateral Vestibular Hypofunction: Results from the 2008 United States National Health Interview Survey," JAMA Otolaryngol Head Neck Surg., **139**(8), pp. 803–810.

[2] Sun, D. Q., Ward, B. K., Semenov, Y. R., Carey, J. P., and Della Santina, C. C., 2014, "Bilateral Vestibular Deficiency: Quality of Life and Economic Implications.," JAMA Otolaryngol. Head Neck Surg., **140**(6), pp. 527–534.

[3] Carey, J. P., and Della Santina, C. C., 2010, "Principles of Applied Vestibular Physiology," Cummings Otolaryngol. - Head Neck Surg., pp. 2276–2304.

[4] Goldberg, J. M., Victor J. Wilson, Cullen, K. E., Angelaki, D. E., Broussard, D. M., Buttner-Ennever, J., Fukushima, K., and Minor, L. B., 2012, The Vestibular System: A Sixth Sense.

[5] Goldberg, J. M., 1991, "The vestibular end organs: morphological and physiological diversity of afferents," Curr. Opin. Neurobiol., **1**(2), pp. 229–235.

[6] Collewijn, H., and Smeets, J. B., 2000, "Early components of the human vestibulo-ocular response to head rotation: latency and gain.," J. Neurophysiol., **84**(1), pp. 376–389.

[7] Leigh, R. J., and Zee, D. S., 2015, The Neurology of Eye Movements, Oxford University Press.

[8] Della Santina, C. C., Cremer, P. D., Carey, J. P., and Minor, L. B., 2002, "Comparison of head thrust test with head autorotation test reveals that the vestibulo-ocular reflex is enhanced during voluntary head movements.," Arch. Otolaryngol. Head. Neck Surg., **128**(9), pp. 1044–1054.

[9] Carey, J. P., Minor, L. B., Peng, G. C. Y., Della Santina, C. C., Cremer, P. D., and Haslwanter, T., 2002, "Changes in the three-dimensional angular vestibulo-ocular reflex

following intratympanic gentamicin for Ménière's disease," JARO - J. Assoc. Res. Otolaryngol., **3**(4), pp. 430–443.

[10] Sadeghi, S. G., Minor, L. B., and Cullen, K. E., 2010, "Neural Correlates of Motor Learning in the Vestibulo-Ocular Reflex: Dynamic Regulation of Multimodal Integration in the Macaque Vestibular System," J. Neurosci., **30**(30), pp. 10158–10168.

[11] Fetter, M., and Zee, D. S., 1988, "Recovery from unilateral labyrinthectomy in rhesus monkey.," J. Neurophysiol., **59**(2), pp. 370–393.

[12] Whitney, S. L., Alghwiri, A. A., and Alghadir, A., 2016, An overview of vestibular rehabilitation, Elsevier B.V.

[13] Yakushina, S. B., Tarasenkoa, Y., Raphan, T., Suzuki, J.-I., Della Santina, C. C., Minor, L. B., and Cohen, B., 2009, "Modification of the Cervico-ocular Reflex by Canal Plugging," Ann N Y Acad Sci., **1164**, pp. 60–70.

[14] Dozza, M., Chiari, L., and Horak, F. B., 2005, "Audio-biofeedback improves balance in patients with bilateral vestibular loss," Arch. Phys. Med. Rehabil., **86**(7), pp. 1401–1403.

[15] Hegeman, J., Honegger, F., Kupper, M., and Allum, J. H. J., 2005, "The balance control of bilateral peripheral vestibular loss subjects and its improvement with auditory prosthetic feedback," J. Vestib. Res., **15**(2), pp. 109–17.

[16] Kentala, E., Vivas, J., and Wall, C., 2003, "Reduction of Postural Sway By Use of a Vibrotactile," Ann Otol Rhinol Laryngol, pp. 404–409.

[17] Peterka, R. J., Wall, C., and Kentala, E., 2006, "Determining the effectiveness of a vibrotactile balance prosthesis," J. Vestib. Res., **16**(1–2), pp. 45–56.

[18] Tyler, M., Danilov, Y., and Bach-Y-Rita, P., 2003, "Closing an Open-Loop Control System: Vestibular Substitution Through the Tongue," J. Integr. Neurosci., **02**(02), pp. 159–164.

[19] Cohen, B., Suzuki, J. I., and M. B. Bender, 1964, "Eye Movements from Semicircular Canal Nerve Stimulation in the Cat," Ann Otol Rhinol Laryngol, **73**(1), pp. 153–169.

[20] Suzuki, J. I., and Cohen, B., 1964, "Head, Eye, Body and Limb Movements From Semicircular Canal Nerves.," Exp. Neurol., **10**(5), pp. 393–405.

[21] Suzuki, J. I., Goto, K., Tokumasu, K., and Cohen, B., 1969, "Implantation of electrodes near individual vestibular nerve branches in mammals," Ann Otol Rhinol Laryngol, **78**(4), pp. 815–826.

[22] Ezure, K., Cohen, M. S., and Wilson, V. J., 1983, "Response of cat semicircular canal afferents to sinusoidal polarizing currents: implications for input-output properties of second-order neurons.," J. Neurophysiol., **49**(3), pp. 639–648.

[23] Suzuki, J. I., Cohen, B., and Bender, M. B., 1964, "Compensatory eye movements induced by vertical semicircular canal stimulation," Exp. Neurol., **9**(2), pp. 137–160.

[24] Gong, W., and Merfeld, D. M., 2000, "Prototype neural semicircular canal prosthesis

using patterned electrical stimulation.," Ann. Biomed. Eng., **28**, pp. 572–581.

[25] Gong, W., and Merfeld, D. M., 2002, "System design and performance of a unilateral horizontal semicircular canal prosthesis," IEEE Trans. Biomed. Eng., **49**(2), pp. 175–181.

[26] Merfeld, D. M., Gong, W., Morrissey, J., Saginaw, M. A., Haburcakova, C., and Lewis, R. F., 2006, "Acclimation to chronic constant-rate peripheral stimulation provided by a vestibular prosthesis," IEEE Trans. Biomed. Eng., **53**(11), pp. 2362–2372.

[27] Saginaw, M. A., Gong, W., Haburcakova, C., and Merfeld, D. M., 2011, "Attenuation of eye movements evoked by a vestibular implant at the frequency of the baseline pulse rate," IEEE Trans. Biomed. Eng., **58**(10 PART 1), pp. 2732–2739.

[28] Lewis, R. F., Nicoucar, K., Gong, W., Haburcakova, C., and Merfeld, D. M., 2013, "Adaptation of vestibular tone studied with electrical stimulation of semicircular canal afferents.," J. Assoc. Res. Otolaryngol., **14**(3), pp. 331–40.

[29] Gorgiladze, G. I., 2004, "Electrical stimulation of labyrinths and vestibular reactions," Bull. Exp. Biol. Med., **138**(6), pp. 629–631.

[30] Della Santina, C. C., Migliaccio, A. A., and Patel, A. H., 2007, "A multichannel semicircular canal neural prosthesis using electrical stimulation to restore 3-d vestibular sensation.," IEEE Trans. Biomed. Eng., **54**(6 Pt 1), pp. 1016–30.

[31] Fridman, G. Y., Davidovics, N. S., Dai, C., Migliaccio, A. A., and Della Santina, C. C., 2010, "Vestibulo-ocular reflex responses to a multichannel vestibular prosthesis incorporating a 3D coordinate transformation for correction of misalignment.," J. Assoc. Res. Otolaryngol., **11**(3), pp. 367–81.

[32] Davidovics, N. S., Fridman, G. Y., Chiang, B., and Della Santina, C. C., 2011, "Effects of biphasic current pulse frequency, amplitude, duration, and interphase gap on eye movement responses to prosthetic electrical stimulation of the vestibular nerve.," IEEE Trans. Neural Syst. Rehabil. Eng., **19**(1), pp. 84–94.

[33] Dai, C., Fridman, G. Y., Chiang, B., Davidovics, N. S., Melvin, T.-A., Cullen, K. E., and Della Santina, C. C., 2011, "Cross-axis adaptation improves 3D vestibulo-ocular reflex alignment during chronic stimulation via a head-mounted multichannel vestibular prosthesis.," Exp. Brain Res., **210**(3–4), pp. 595–606.

[34] Davidovics, N. S., Fridman, G. Y., and Della Santina, C. C., 2012, "Co-modulation of stimulus rate and current from elevated baselines expands head motion encoding range of the vestibular prosthesis," Exp. Brain Res., **218**(3), pp. 389–400.

[35] Chiang, B., Fridman, G. Y., Dai, C., Rahman, M. A., and Della Santina, C. C., 2011, "Design and performance of a multichannel vestibular prosthesis that restores semicircular canal sensation in rhesus monkey.," IEEE Trans. Neural Syst. Rehabil. Eng., **19**(5), pp. 588–98.

[36] Dai, C., Fridman, G. Y., Davidovics, N. S., Chiang, B., Ahn, J. H., and Della Santina, C. C., 2011, "Restoration of 3D vestibular sensation in rhesus monkeys using a multichannel vestibular prosthesis.," Hear. Res., **281**(1–2), pp. 74–83.

[37] Dai, C., Fridman, G. Y., Chiang, B., Rahman, M. A., Ahn, J. H., Davidovics, N. S., and Della Santina, C. C., 2013, “Directional plasticity rapidly improves 3D vestibulo-ocular reflex alignment in monkeys using a multichannel vestibular prosthesis.,” J. Assoc. Res. Otolaryngol., **14**(6), pp. 863–77.

[38] Davidovics, N. S., Rahman, M. A., Dai, C., Ahn, J., Fridman, G. Y., and Della Santina, C. C., 2013, “Multichannel vestibular prosthesis employing modulation of pulse rate and current with alignment precompensation elicits improved VOR performance in monkeys.,” J. Assoc. Res. Otolaryngol., **14**(2), pp. 233–48.

[39] Nie, K., Ling, L., Bierer, S. M., Kaneko, C. R. S., Fuchs, A. F., Oxford, T., Rubinstein, J. T., and Phillips, J. O., 2013, “An experimental vestibular neural prosthesis: Design and preliminary results with rhesus monkeys stimulated with modulated pulses,” IEEE Trans. Biomed. Eng., **60**(6), pp. 1685–1692.

[40] Phillips, C. M., Ling, L., Oxford, T., Nowack, A., Nie, K., Rubinstein, J. T., and Phillips, J. O., 2014, “Longitudinal performance of an implantable vestibular prosthesis.,” Hear. Res., (September), pp. 1–12.

[41] Wall, C., Kos, M. I., and Guyot, J. P., 2007, “Eye movements in response to electric stimulation of the human posterior ampullary nerve,” Ann. Otol. Rhinol. Laryngol., **116**(5), pp. 369–374.

[42] Guyot, J. P., Sigrist, A., Pelizzone, M., and Kos, M. I., 2011, “Adaptation to steady-state electrical stimulation of the vestibular system in humans,” Ann. Otol. Rhinol. Laryngol., **120**(3), pp. 143–149.

[43] Guyot, J. P., Sigrist, A., Pelizzone, M., Feigl, G. C., and Kos, M. I., 2011, “Eye movements in response to electrical stimulation of the lateral and superior ampullary nerves,” Ann. Otol. Rhinol. Laryngol., **120**(2), pp. 81–87.

[44] Perez Fornos, A., Guinand, N., Van De Berg, R., Stokroos, R. J., Micera, S., Kingma, H., Pelizzone, M., and Guyot, J. P., 2014, “Artificial balance: Restoration of the vestibulo-ocular reflex in humans with a prototype vestibular neuroprosthesis,” Front. Neurol., **5 APR**(April), pp. 1–11.

[45] Guinand, N., Van De Berg, R., Cavuscens, S., Stokroos, R. J., Ranieri, M., Pelizzone, M., Kingma, H., Guyot, J. P., and Perez Fornos, A., 2015, “Vestibular Implants: 8 Years of Experience with Electrical Stimulation of the Vestibular Nerve in 11 Patients with Bilateral Vestibular Loss,” Orl, **77**, pp. 227–240.

[46] van de Berg, R., Guinand, N., Nguyen, T. a. K., Ranieri, M., Cavuscens, S., Guyot, J.-P., Stokroos, R. J., Kingma, H., and Perez Fornos, A., 2015, “The vestibular implant: frequency-dependency of the electrically evoked vestibulo-ocular reflex in humans,” Front. Syst. Neurosci., **8**(January), pp. 1–12.

[47] Nguyen, T. A. K., DiGiovanna, J., Cavuscens, S., Ranieri, M., Guinand, N., van de Berg, R., Carpaneto, J., Kingma, H., Guyot, J.-P., Micera, S., and Fornos, A. P., 2016, “Characterization of pulse amplitude and pulse rate modulation for a human vestibular implant during acute electrical stimulation,” J. Neural Eng., **13**(4), p. 046023.

[48] Perez Fornos, A., Cavuscens, S., Ranieri, M., van de Berg, R., Stokroos, R. J., Kingma, H., Guyot, J.-P., and Guinand, N., 2017, "The vestibular implant: A probe in orbit around the human balance system," J. Vestib. Res., **27**(1), pp. 51–61.

[49] Guinand, N., Van de Berg, R., Cavuscens, S., Ranieri, M., Schneider, E., Lucieer, F., Kingma, H., Guyot, J. P., and Fornos, A. P., 2017, "The video head impulse test to assess the efficacy of vestibular implants in humans," Front. Neurol., **8**(NOV).

[50] van de Berg, R., Guinand, N., Ranieri, M., Cavuscens, S., Khoa Nguyen, T. A., Guyot, J.-P., Lucieer, F., Starkov, D., Kingma, H., van Hoof, M., and Perez-Fornos, A., 2017, "The Vestibular Implant Input Interacts with Residual Natural Function," Front. Neurol., **8**(December).

[51] Golub, J. S., Ling, L., Nie, K., Nowack, A., Shepherd, S. J., Bierer, S. M., Jameyson, E., Kaneko, C. R. S., Phillips, J. O., and Rubinstein, J. T., 2014, "Prosthetic implantation of the human vestibular system.," Otol. Neurotol., **35**(1), pp. 136–47.

[52] Phillips, J. O., Ling, L., Nie, K., Jameyson, E., Phillips, C. M., Nowack, A. L., Golub, J. S., Rubinstein, J. T., J.O., P., L., L., K., N., E., J., C.M., P., A.L., N., J.S., G., and J.T., R., 2015, "Vestibular implantation and longitudinal electrical stimulation of the semicircular canal afferents in human subjects," J. Neurophysiol., **113**(10), pp. 3866–3892.

[53] 2016, "Multichannel Vestibular Implant Early Feasibility Study," ClinicalTrials.gov, p. NCT02725463 [Online]. Available: https://clinicaltrials.gov/ct2/show/NCT02725463?cond=vestibular+implant&rank=1.

[54] Otero-Millan, J., Roberts, D. C., Lasker, A., and Zee, D. S., 2015, "Knowing what the brain is seeing in three dimensions: A novel, noninvasive, sensitive, accurate, and low-noise technique for measuring ocular torsion," J. Vis., **15(14)**(11), pp. 1–15.

[55] Haustein, W., 1989, "Considerations on Listing's Law and the primary position by means of a matrix description of eye position control," Biol. Cybern., **60**(6), pp. 411–420.

[56] Savitzky, A., and Golay, M. J. E., 1964, "Smoothing and Differentiation of Data by Simplified Least Squares Procedures.," Anal. Chem., **36**(8), pp. 1627–1639.

[57] Haslwanter, T., 1995, "Mathematics of three-dimensional eye rotations," Vision Res., **35**(12), pp. 1727–1739.

[58] Migliaccio, A. A., and Todd, M., 1999, "Real-time rotation vectors.," Phys. Eng. Sci. Med., **June; 22**(2), pp. 73–80.

[59] Migliaccio, A. A., 2001, "Listing's Plane and the Human Vestibulo-Ocular Reflex.," University of New South Wales.

[60] Della Santina, C. C., Potyagaylo, V., Migliaccio, A. A., Minor, L. B., and Carey, J. P., 2005, "Orientation of human semicircular canals measured by three-dimensional multiplanar CT reconstruction," JARO - J. Assoc. Res. Otolaryngol., **6**(3), pp. 191–206.

[61] Salter, K. C., and Fawcett, R. F., 1993, "The art test of interaction: a robust and powerful rank test of interaction in factorial models," Commun. Stat. - Simul. Comput., **22**(1), pp.

137–153.

[62] Higgins, J. J., and Tashtough, S., 1994, “An aligned rank transform test for interactione,” Nonlinear World, (2), pp. 201–211.

[63] Wobbrock, J. O., Findlater, L., Gergle, D., and Higgins, J. J., 2011, “The Aligned Rank Transform for Nonparametric Factorial Analyses Using Only ANOVA Procedures,” Proc. SIGCHI Conf. Hum. Factors Comput. Syst., pp. 143–146.

[64] Cullen, K. E., Sadeghi, S. G., Beraneck, M., and Minor, L. B., 2009, “Neural substrates underlying vestibular compensation: Contribution of peripheral versus central processing,” J Vestib Res., **19**, pp. 171–182.

[65] Halmagyi, G. M., Weber, K. P., and Curthoys, I. S., 2010, “Vestibular function after acute vestibular neuritis,” Restor. Neurol. Neurosci., **28**(1), pp. 37–46.

[66] Guyot, J.-P., and Toupet, M., 2007, “Late and sudden recovery of sudden deafness or vestibular neuronitis,” Ann. d’Otolaryngologie Chir. Cervico-faciale, **124**(4), pp. 205–209.

[67] Berthoz, A., Melvill Jones, G., and Bégué, A. E., 1981, “Differential visual adaptation of vertical canal-dependent vestibulo-ocular reflexes,” Exp. Brain Res., **44**(1), pp. 19–26.

[68] Berthoz, A., Jones, G. M., and Begue, A., 1981, “Long-Term Effects of Dove Prism Vision on Torsional VOR and Head-Eye Coordination.”

[69] Solomon, D., Zee, D. S., and Straumann, D., 2003, “Torsional and horizontal vestibular ocular reflex adaptation: Three-dimensional eye movement analysis,” Exp. Brain Res., **152**(2), pp. 150–155.

[70] Trillenberg, P., Shelhamer, M., Roberts, D. C., and Zee, D. S., 2003, “Cross-axis adaptation of torsional components in the yaw-axis vestibulo-ocular reflex,” Exp. Brain Res., **148**(2), pp. 158–165.

[71] M. Furman, J., Koizuka, I., and H. Schor, R., 2000, “Characteristics of secondary phase post-rotatory nystagmus following off-vertical axis rotation in humans,” J. Vestib. Res., **10**, pp. 143–150.

[72] M. Furman, J., Hain, T. C., and Paige, G. D., 1989, “Central Adaptation Models of the Vestibulo-Ocular and Optokinetic Systems,” Biol. Cybern., **61**, pp. 255–264.

[73] Goldberg, J. M., and Fernández, C., 1971, “Physiology of peripheral neurons innervating semicircular canals of the squirrel monkey. I. Resting discharge and response to constant angular accelerations.,” J. Neurophysiol., **34**(4), pp. 635–660.

[74] Leigh, R. J., Robinson, D. A., and Zee, D. S., 1981, “A Hypothetical Explanation for Periodic Alternating Nystagmus: Instability in the Optokinetic-Vestibular System,” Ann. N. Y. Acad. Sci., **374**(1), pp. 619–635.

[75] Malcolm, R., and Jones, G. M., 1970, “A quantitative study of vestibular adaptation in humans,” Acta Otolaryngol., **70**(2), pp. 126–135.

[76] Sadeghi, S. G., Minor, L. B., and Cullen, K. E., 2007, “Response of vestibular-nerve afferents to active and passive rotations under normal conditions and after unilateral labyrinthectomy.,” J. Neurophysiol., **97**(2), pp. 1503–1514.

[77] Bahmer, A., Peter, O., and Baumann, U., 2010, “Recording and analysis of electrically evoked compound action potentials (ECAPs) with MED-EL cochlear implants and different artifact reduction strategies in Matlab.,” J. Neurosci. Methods, **191**(1), pp. 66–74.

[78] Cremer, P. D., Migliaccio, A. A., Pohl, D. V., Curthoys, I. S., Davies, L., Yavor, R. A., and Halmagyi, G. M., 2000, “Posterior semicircular canal nystagmus is conjugate and its axis is parallel to that of the canal,” Neurology, **54**(10), pp. 2016–2020.

[79] Cremer, P. D., Minor, L. B., Carey, J. P., and Della Santina, C. C., 2000, “Eye movements in patients with superior canal dehiscence syndrome align with the abnormal canal,” Neurology, **55**(12), pp. 1833–1841.

[80] Migliaccio, A. A., Della Santina, C. C., Carey, J. P., Minor, L. B., and Zee, D. S., 2006, “The effect of binocular eye position and head rotation plane on the human torsional vestibuloocular reflex,” Vision Res., **46**(16), pp. 2475–2486.

[81] Schultheis, L. W., and Robinson, D. A., 1981, “Directional Plasticity of the Vestibulo-Ocular Reflex in the Cat,” Ann. N. Y. Acad. Sci., **374**(1), pp. 504–512.

[82] Gonshor, A., and Jones, G. M., 1976, “Short-term adaptive changes in the human vestibulo-ocular reflex arc,” J. Physiol., **256**(2), pp. 361–379.

[83] Gonshor, A., and Jones, G. M., 1976, “Extreme vestibulo-ocular adaptation induced by prolonged optical reversal of vision,” J. Physiol., **256**(2), pp. 381–414.

[84] Gonshor, A., and Melvill Jones, G., 1980, “Postural adaptation to prolonged optical reversal of vision in man,” Brain Res., **192**(1), pp. 239–248.

[85] Sun, D. Q., Lehar, M., Dai, C., Swarthout, L., Lauer, A. M., Carey, J. P., Mitchell, D. E., Cullen, K. E., and Santina, C. C. D., 2015, “Histopathologic Changes of the Inner ear in Rhesus Monkeys After Intratympanic Gentamicin Injection and Vestibular Prosthesis Electrode Array Implantation,” JARO - J. Assoc. Res. Otolaryngol., **16**(3), pp. 373–387.

[86] Wilson, B. S., Finley, C. C., Lawson, D. T., Wolford, R. D., and Zerbi, M., 1993, “Design and evaluation of a continuous interleaved sampling (CIS) processing strategy for multichannel cochlear implants.,” J. Rehabil. Res. Dev., **30**(1), pp. 110–6.

[87] Louizou, P. C., 1998, “Mimicking the Human Ear,” IEEE Signal Process. Mag., pp. 101–130.

[88] Wilson, B. S., and Dorman, M. F., 2008, “Cochlear implants: a remarkable past and a brilliant future.,” Hear. Res., **242**(1–2), pp. 3–21.

[89] Merfeld, D. M., Haburcakova, C., Gong, W., and Lewis, R. F., 2007, “Chronic vestibulo-ocular reflexes evoked by a vestibular prosthesis,” IEEE Trans. Biomed. Eng., **54**(6), pp. 1005–1015.

[90] Baird, R. a, Desmadryl, G., Fernández, C., and Goldberg, J. M., 1988, "The vestibular nerve of the chinchilla. II. Relation between afferent response properties and peripheral innervation patterns in the semicircular canals.," J. Neurophysiol., **60**(1), pp. 182–203.

[91] Robinson, D. A., 1963, "A Method of Measuring Eye Movement Using a Scleral Search Coil in a Magnetic Field," IEEE Trans. Bio-Medical Electron., **10**, pp. 137–145.

[92] Minor, L. B., Lasker, D. M., Backous, D. D., and Hullar, T. E., 1999, "Horizontal Vestibuloocular Reflex Evoked by High-Acceleration Rotations in the Squirrel Monkey . I. Normal Responses," J .Neurophysiol., **82**(3), pp. 1254–1270.

[93] Migliaccio, A. A., Schubert, M. C., Jiradejvong, P., Lasker, D. M., Clendaniel, R. a, and Minor, L. B., 2004, "The three-dimensional vestibulo-ocular reflex evoked by high-acceleration rotations in the squirrel monkey.," Exp. Brain Res., **159**(4), pp. 433–46.

[94] Nguyen, K. D., Minor, L. B., Della Santina, C. C., and Carey, J. P., 2009, "Vestibular function and vertigo control after intratympanic gentamicin for Ménière's disease," Audiol. Neurotol., **14**(6), pp. 361–372.

[95] Straumann, D., Zee, D. S., Solomon, D., Lasker, A. G., and Roberts, D. C., 1995, "Transient torsion during and after saccades," Vision Res., **35**(23–24), pp. 3321–3334.

[96] Tweed, D., Cadera, W., and Vilis, T., 1990, "Computing three-dimensional eye position quaternions and eye velocity from search coil signals," Vision Res., **30**(1), pp. 97–110.

[97] Valentin, N., Hageman, K. N., Dai, C., Della Santina, C. C., and Fridman, G. Y., 2013, "Development of a Multichannel Vestibular Prosthesis Prototype by Modification of a Commercially Available Cochlear Implant.," IEEE Trans. Neural Syst. Rehabil. Eng., **2**(MCI).

[98] Hochmair, I., Nopp, P., Jolly, C., Schmidt, M., Schößer, H., Garnham, C., and Anderson, I., 2006, "MED-EL Cochlear Implants: State of the Art and a Glimpse Into the Future," Trends Amplif., **10**(4), pp. 201–219.

[99] Kleine Punte, A., De Bodt, M., and Van De Heyning, P., 2014, "Long-term improvement of speech perception with the fine structure processing coding strategy in cochlear implants," Orl, **76**(1), pp. 36–43.

[100] Roy, A. T., Carver, C., Jiradejvong, P., and Limb, C. J., 2015, "Musical Sound Quality in Cochlear Implant Users: A Comparison in Bass Frequency Perception between Fine Structure Processing and High-Definition Continuous Interleaved Sampling Strategies," Ear Hear., **36**(5), pp. 582–590.

[101] Zirn, S., Arndt, S., Aschendorff, A., Laszig, R., and Wesarg, T., 2016, "Perception of Interaural Phase Differences with Envelope and Fine Structure Coding Strategies in Bilateral Cochlear Implant Users," Trends Hear., **20**, pp. 1–12.

Curriculum Vitae

Peter Joseph Boutros

Born November 2nd, 1989 in Milford, CT

EDUCATION

2012-2018 **The Johns Hopkins School of Medicine**, Baltimore, MD
Ph.D. in Biomedical Engineering
Mentor: Dr. Charles C. Della Santina, Ph.D., M.D.

2008-2012 **The University of Connecticut**, Storrs, CT
Honors Scholar, summa cum laude
Major: BS in Biomedical Engineering
Minors: Electronics & Systems, Mathematics

PROFESSIONAL EXPERIENCE

2012-2018 **Vestibular NeuroEngineering Laboratory,** Johns Hopkins University, Baltimore, MD
Graduate Research Assistant

2017-2018 **Johns Hopkins Institute for Applied Economics, Global Health, and the Study of Business Enterprise**, Baltimore, MD
Equity Research Analyst

2015-2017 **Johns Hopkins Technology Ventures,** Baltimore, MD
Commercialization Academy Intern

2010-2012 **Physiologic Acoustics Laboratory,** University of Connecticut, Storrs, CT
Undergraduate Research Assistant

TEACHING EXPERIENCE

Johns Hopkins University, Department of Biomedical Engineering, Baltimore, MD
2015 *Systems Bioengineering II*
2014 *Principals and Design of Biomedical Instrumentation*

University of Connecticut, Department of Biomedical Engineering, Storrs, CT
2012 *Biomedical Engineering Measurements*

2011	*Biosystem Analysis*
2011	*Introduction to Biomedical Engineering*

LEADERSHIP ACTIVITIES

	BME Extramural Development in Graduate Education Center, Johns Hopkins University, Baltimore, MD
2014-2015	*Center Co-Chair*
2013-2014	*Director of Internships*
	Biomedical Engineering Society, University of Connecticut, Storrs, CT
2011-2012	*Technology Chair*

AWARDS AND HONORS

2016	*UMN Neuromodulation Symposium, 2nd Place Poster Award*
2012	*Honors Scholar*
2012	*Babbidge Scholar*
2008-2012	*Dean's List Award*
2009-2011	*New England Scholar*
2011	*Summer Undergraduate Research Fund (SURF) Award*
2010	*Summer Undergraduate Research Fund (SURF) Award*
2010	*Office of Undergraduate Research (OUR) Grant*

PEER-REVIEWED PUBLICATIONS

1. **Boutros, P. J.**, Valentin, N., Hageman, K. N., Roberts, D., Dai, C., and Della Santina, C. C., 2016, "Temporal Discretization Errors Produce Minimal Effects on Vestibular Prosthesis Performance," J. Med. Device., 10(3), p. 030958.
2. Hageman, K. N., Chow, M. R., **Boutros, P. J.**, Roberts, D., Tooker, A., Lee, K., Felix, S., Pannu, S. S., and Della Santina, C. C., 2016, "Design of a Vestibular Prosthesis for Sensation of Gravitoinertial Acceleration," J. Med. Device., 10(3), p. 030923.
3. Rabbitt, R.D., Brichta, A.M., Tabatabaee, H., **Boutros, P.J.**, Ahn, J.H., Della Santina, C.C., Poppi, L., and Lim, R., 2016, "Heat pulse excitability of vestibular hair cells and afferent neurons," *J. Neurophysiol.*, 2016, p. jn.00110.2016.

PRESENTATIONS

1. **Boutros, P.J.**, Schoo, D., Rahman, M., Valentin, N.S., Chow, M., Gimmon, Y., Bowditch, S., Hofner, A., Morillo, Rascon A., Marx, A., Deas, R., Strasser, S., Fridman, G. Y., Davidovics, N., Roberts, D., Morris, B., Ayiotis, A., Lane, K., Hedjoudje, A., Ward, B., Treviño, C., Schubert, M., Carey, J. P., Jaeger, A., Della Santina, C. C. "First-in-human Safety and Preliminary Efficacy Results for the MVI Multichannel Vestibular Implant" *Bárány Society Meeting 2018*, Uppsala, Sweden, June 2018
2. **Boutros, P.J.** "MVI™ First-in-Human Clinical Trial Update" *iVP Pilot Project Update Meeting*, Innsbruck, Austria, March 2017
3. **Boutros, P.J.**, Rahman, M., Valentin, N.S., Schoo, D., Tan, G., Gimmon, Y., Chow, M., Hofner, A., Morillo Rascon, A., Marx, A., Deas, R., De Marzo, A., Rodriquez, F., Strasser, S., Fridman, G. Y., Dai, C., Ward, B., Schubert, M., Bowditch, S., Jaeger, A., Carey, J. P., Della Santina, C. C.

"Continuous Restoration of the Human Vestibulo-Ocular Reflex via a Multichannel Vestibular Implant" *Neuromodulation Symposium 2017*, Minneapolis, MN, April 2017. MNS2017-240

ABSTRACTS & POSTERS

1. Ren, P., Hedjoudje, A., Wang, G., Ahn, J.H., Rahman, M., **Boutros, P.J.**, Della Santina, C.C., Dai, C., "Intralabyrinthine vs. Distant Reference Electrodes for Multichannel Vestibular Prosthesis in Rhesus Monkeys" *Association for Research in Otolaryngology Mid-Winter Meeting 2019*, Baltimore, MD, February 2019
2. Anson, E., Gimmon, Y., **Boutros, P.J.**, Schubert, M. "Size Matters for Vestibular Perception of Spatial Orientation" *International Conference on Vestibular Rehabilitation*, Chicago, IL, August 2018
3. **Boutros, P.J.**, Rahman, M., Valentin, N.S., Schoo, D., Gimmon, Y., Chow, M., Hofner, A., Morillo Rascon, A., Marx, A., Deas, R., Fridman, G. Y., Davidovics, N. S., Ward, B. K., Treviño, C., Bowditch, S.,Roberts, D.C., Schubert, M., Jaeger, A., Carey, J. P., Della Santina, C. C. "First-in-Human Clinical Trial of the MVI™ Multichannel Vestibular Implant: Continuous Restoration of the Human Vestibulo-Ocular Reflex" *Association for Research in Otolaryngology Mid-Winter Meeting 2018*, San Diego, CA, February 2018.
4. Chow, M., Gimmon, Y., Schoo, D.P., Trevino, C., **Boutros, P.J.**, Rahman, M., Valentin, N., Hofner, A., Morillo Rascon, A., Marx, A., Deas, R., Fridman, G.Y., Jaeger, A., Schubert, M.C., Carey, J., Della Santina, C.C. "First-in-Human Clinical Trial of the MVI™ Multichannel Vestibular Implant in Individuals with Bilateral Sensorineural Vestibular Loss: Effects on Gait and Posture" *Association for Research in Otolaryngology Mid-Winter Meeting 2018*, San Diego, CA, February 2018.
5. Schoo, D.P., Bowditch, S., Marsiglia, D., **Boutros, P.J.**, Chow, M., Gimmon, Y., Rahman, M., Valentin, N., Ward, B. K., Trevino, C., Davidovics, N. S., Hofner, A., Morillo Rascon, A., Marx, A., Deas, R., Fridman, G.Y., Jaeger, A., Carey, J., Della Santina, C.C. "Long-term Audiometric Results from the first 3 subjects of the MVI™ Multichannel Vestibular Implant Early Feasibility Study" *Association for Research in Otolaryngology Mid-Winter Meeting 2018*, San Diego, CA, February 2018.
6. **Boutros, P.J.**, Rahman, M., Valentin, N.S., Schoo, D., Tan, G., Gimmon, Y., Chow, M., Hofner, A., Morillo Rascon, A., Marx, A., Deas, R., De Marzo, A., Rodriquez, F., Strasser, S., Fridman, G. Y., Dai C., Ward, B., Schubert, M., Bowditch, S., Jaeger, A., Carey, J. P., Della Santina, C. C. "Continuous Restoration of the Human Vestibulo-Ocular Reflex via a Multichannel Vestibular Implant" *Neuromodulation Symposium* 2017, Minneapolis, MN, April 2017.
7. Hageman, K.N., Chow, M.R., **Boutros, P.J.**, Roberts, D., Della Santina, C.C. "Electrically-Evoked Eye Movements using a Vestibular Prosthesis Designed to Restore Sensation of Gravitoinertial Acceleration." *Neuromodulation Symposium 2017,* Minneapolis, MN, April 2017.
8. Hageman, K.N., Chow, M.R., **Boutros, P.J.**, Roberts, D., Tooker, A., Lee, K., Felix, S., Pannu, S.S., Della Santina, C.C. "Design of a Vestibular Prosthesis for Sensation of Gravitoinertial Acceleration." *Design of Medical Devices Conference 2016* and *Neuromodulation Symposium 2016*, Minneapolis, MN, April 2016.
9. **Boutros, P.J.**, Valentin, N., Hageman, K.N., Roberts, D., Dai, C., Della Santina, C.C. "Temporal Discretization Errors Produce Minimal Effects on Vestibular Prosthesis Performance." *Design of Medical Devices Conference 2016* and *Neuromodulation Symposium 2016*, Minneapolis, MN, April 2016.
10. Hageman, K.N., Chow, M.R., Roberts, D., Ren, P. **Boutros, P.J.**, Dai, C., Della Santina, C.C. "Characterization of Normal 3D Binocular Chinchilla Otolith-Ocular Reflexes as a Metric to Study

Otolith Stimulation using a Multichannel Vestibular Prosthesis." *Association for Research in Otolaryngology Mid-Winter Meeting 2016*, San Diego, CA, February 2016.

11. **Boutros, P.J.**, Valentin, N., Roberts, D., Hageman, K.N., Dai, C., Della Santina, C.C. "Temporal Discretization Inherent to Continuous Interleaved Sampling Stimulation Causes Negligible Effects on Vestibulo-Ocular Reflex Responses Elicited in Rhesus Monkeys." *Association for Research in Otolaryngology Mid-Winter Meeting 2016*, San Diego, CA, February 2016.
12. Rabbitt, R., Brichta, A., Tabatabaee, T., **Boutros, P.J.**, Ahn, JH., Della Santina, C.C., Poppi, L., Lim, R. "Excitation and Inhibition of Semicircular Canal Type II Hair Cells by Pulsed Infrared Light" *Association for Research in Otolaryngology Mid-Winter Meeting 2016*, San Diego, CA, February 2016.
13. **Boutros, P.J.**, Hageman, K.N., Tooker, A., Lee, K., Felix, S., Dai, C., Pannu, S., Della Santina, C.C. "High Density Micro-machined Polyimide Electrode Arrays for Vestibular Implants." *Association for Research in Otolaryngology Mid-Winter Meeting 2015*, Baltimore, MD, February 2015.
14. **Boutros P.J.**, Ahn J.H., Fridman G.Y., Dai C., Lasker D., Della Santina C.C. "Vestibular Primary Afferent and Vestibulo-Ocular Reflex Eye Movement Responses to Infrared Laser Stimulation of the Mammalian Labyrinth" *Association for Research in Otolaryngology Mid-Winter Meeting 2013*, Baltimore, MD. February 2013.
15. **Boutros, P.J.**, Kim, D., Kuwada, S., Escabi, M. "Temporal Nonlinearities for Amplitude Modulation Coding in the Unanesthesized Rabbit Inferior Colliculus" *Society for Neuroscience 2012*, New Orleans, LA. November 2012
16. **Boutros, P.J.**, Lee, C., Mathews, S., Wilkens, P., Peterson, D., McIsaac, J. "Novel 3-D Brachial Plexus Reconstruction from 2-D Ultrasound Using XBOX Kinect Tracking" *2012 Biomedical Engineering Society Annual Meeting*, Atlanta, GA. October 2012
17. **Boutros P.J.**, Kim D., Kuwada S., Escabi M. "Temporal Nonlinearities for Amplitude Modulation Coding in the Unanesthesized Rabbit Inferior Colliculus" *Association for Research in Otolaryngology Mid-Winter Meeting 2012*, San Diego, CA, February 2012